Transmisión de señales neuronales con UWB y medidas de canal en entorno corporal

Autor: Paula Martí Rocafull

Director1: Cristina Tarín Sauer

Director2: Narcís Cardona Marcet

Resumen — La captación, comprensión e interpretación de las señales neuronales, son las claves para el estudio del funcionamiento del cerebro humano. Los dispositivos de captación y transmisión de señales tienden actualmente hacia la transmisión inalámbrica, especialmente debido a la movilidad que esta ofrece. En el siguiente trabajo se estudiará la transmisión de señales neuronales utilizando la tecnología inalámbrica Ultra Wideband, cuya elección se justifica teniendo en cuenta los requerimientos de ancho de banda de la aplicación. Por un lado, se realizarán transmisiones de archivos que contienen señales neuronales reales para distintas velocidades de envío y se analizarán los datos recibidos. Por otro, se hará un estudio del canal Ultra Wideband en entorno corporal para dos casos distintos: un enlace implante cerebral a dispositivo móvil y un enlace implante cerebral a implante corporal. Se realizará una campaña de medidas del canal para diferentes posiciones de antena transmisora y receptora, según los casos contemplados. De estas medidas se extraerá información relativa al canal, tal como path loss, power delay profile, delay spread, etc.
Finalmente, se utilizará la información obtenida para sacar conclusiones acerca de viabilidad de la transmisión y velocidades posibles de transmisión.

Abstract — Recording, comprehension and interpretation of the neural signals are the keys for the study of the human's brain function. The recording and transmission devices of signals tend nowadays towards the wireless transmission, especially due to the mobility that offers. In this work, neural signal transmission has been performed using Ultra Wideband wireless technology because of the bandwidth requirements of the application. On the one hand, several file transmissions containing real neural signals have been transmitted at different data rates and the received data have been analyzed. On the other hand, the Ultra Wideband channel in corporal environment has been studied for two different cases: a link between an implant located in the head and a handheld device and a link between a head implant and a body implant. A measurement campaign has been held with different transmitter and receiver antenna locations for both cases. With these

Autor: Paula Martí Rocafull, email: paumarro@iteam.upv.es
Director 1: Cristina Tarín Sauer, email: critasa@iteam.upv.es
Director 2: Narcís Cardona Marcet, email: ncardona@dcom.upv.es
Fecha de entrega: 30-02-07

measurements, channel information such as path loss, power delay profile, delay spread, etc. has been assessed.

Finally, according to the obtained results, possible transmission data rates and conclusions about the feasibility of the transmission have been set.

ÍNDICE

I. MOTIVACIÓN

Conforme la medicina y la tecnología evolucionan, el conocimiento sobre el funcionamiento del cuerpo es cada vez mayor y más preciso. Sin embargo, la parte fundamental del hombre, el cerebro, sigue siendo un gran misterio. El estudio del funcionamiento del cerebro humano, está resultando complejo y lento debido a la dificultad de obtener, comprender e interpretar las señales neuronales.

En este campo de investigación existen ciertas técnicas para captar las señales neuronales, algunas no invasivas, como los electroencefalogramas [4] o los magnetoencefalogramas [5] (que registran la actividad eléctrica o magnética del cerebro, respectivamente) y otras invasivas, utilizando sensores que son insertados en la zona del cerebro que se pretende estudiar [6]. Las técnicas más sofisticadas registran la información proveniente de una neurona o un pequeño grupo de ellas, por lo que registrar toda la información de una determinada zona del cerebro requiere un elevado número de microelectrodos. Por ejemplo, para una zona de 20 μm x 20 μm, podríamos tener 64 microelectrodos (en un array de 8x8). Generalmente las neuronas son cultivadas *in-vitro* directamente sobre estos microelectrodos [7]. Los datos captados de las neuronas son básicamente trenes de impulsos en los que está codificada la información que se pretende interpretar por lo que los sensores deben capturarlos y enviarlos con la mayor fiabilidad posible.

Todas las técnicas mencionadas anteriormente requieren de un cableado entre el sensor y la máquina a la que se conectan y en la que se reciben los datos. Por ello, la medicina muestra un creciente interés por el uso de las tecnologías inalámbricas aplicadas tanto a equipamiento médico como a dispositivos portables por el paciente. Este interés viene respaldado por las ventajas que ofrece la conexión sin cables: es más limpio, ahorra espacio y sobre todo ofrece movilidad al paciente.

Otra de las ventajas que ofrece la comunicación inalámbrica es la posibilidad de obtener la información de forma remota. Esto es muy útil en aplicaciones de telemedicina ([8],[9]), donde el médico es capaz de saber lo que le ocurre al paciente y diagnosticarle sin estar presente, y también para la obtención de información durante actividades de la vida cotidiana o durante largos periodos de tiempo en el que el paciente es monitorizado pero tiene libertad de movimientos.

En esta situación se enmarca el proyecto Sinaptic, con el que el grupo de comunicaciones móviles del Instituto de Telecomunicaciones y Aplicaciones Multimedia (iTEAM) ha comenzado sus estudios en esta área. Más concretamente, en la transmisión inalámbrica de señales neuronales desde un implante cerebral a un servidor, un ordenador o dispositivo remoto que sea capaz de almacenarlas, procesarlas o simplemente mostrarlas en tiempo real.

Esta transmisión plantea básicamente dos problemas a resolver. El primero es que el implante, en caso de aplicación *in vivo,* va a ser introducido en el cerebro, con lo cual debe ser lo más

pequeño y simple posible. Esto requiere que no haya almacenamiento, sino transmisión en tiempo real y que su potencia de transmisión sea muy limitada. Por esta última premisa podemos suponer que su rango de alcance no será muy alto y que no podrá comunicarse directamente con un receptor que se encuentre lejos (otra habitación, otro país, etc.). El segundo problema es la cantidad de información a transmitir. Dado que se van a necesitar muchos electrodos, que además queremos capturar la información de forma continua y que esta información debe ser transmitida en tiempo real, la tasa de transmisión o *throughput* necesaria para enviar esa información va a ser muy elevada.

De forma general, se plantea el esquema mostrado en la Fig. 1. El objetivo es enviar las señales neuronales del implante situado en el cerebro a un servidor. Para conseguir movilidad para el paciente, y dado que el servidor puede estar muy alejado del implante, se propone la utilización de otras tecnologías que hagan de "puente" entre ambos.

Como puente se ha elegido un móvil, una PDA o un dispositivo comercial similar, usuales en nuestra vida cotidiana y que el paciente pueda llevar consigo sin mayor molestia. Las señales provenientes del implante serán enviadas al dispositivo móvil utilizando una tecnología inalámbrica de corto alcance y que cumpla los requisitos de *throughput* y potencia comentados anteriormente. El dispositivo móvil reenviará las señales hacia el servidor a través de Internet (utilizando una tecnología de mayor alcance, como por ejemplo UMTS) de modo que el servidor, también conectado, pueda recibirlas.

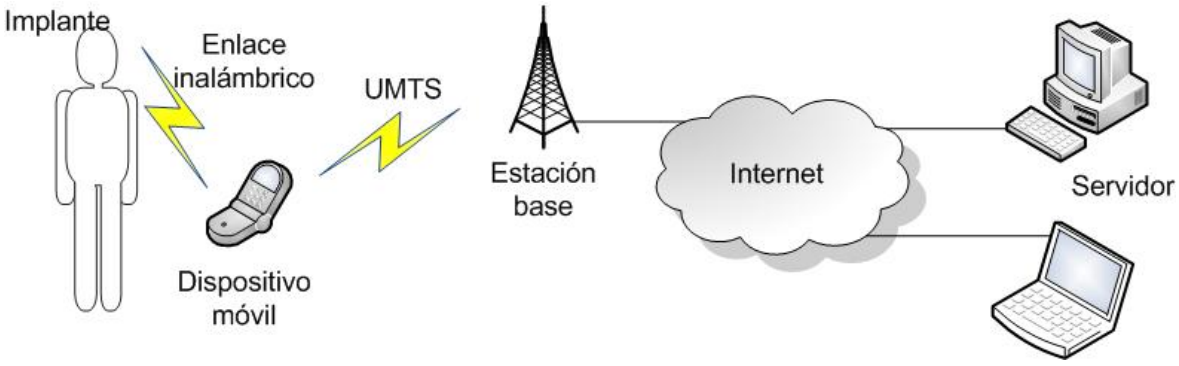

Fig. 1 Sistema de comunicaciones propuesto entre un dispositivo implantable y un servidor remoto

La elección de la tecnología inalámbrica a utilizar entre el implante y el dispositivo móvil para el correcto envío de las señales neuronales se describirá más adelante, en los puntos III y IV. Tras el estudio de las tecnologías existentes, se deduce que UWB es la más adecuada para la aplicación.

La transmisión de señales neuronales requiere de una fiabilidad en la conexión con el fin de no perder información. El efecto de las pérdidas de paquetes en el enlace UWB se estudia en el punto V, donde se han realizado experimentos a distintas distancias y velocidades de transmisión UWB para hallar la mejor configuración para el envío de las señales neuronales.

En el punto VI, se muestran los resultados obtenidos al realizar diversas medidas de canal UWB en un entorno típico de oficina. Se ha aprovechado el montaje para estudiar, no sólo el canal correspondiente al enlace implante cerebral a dispositivo móvil, sino también posibles canales entre implantes corporales, pensando en futuras aplicaciones en las que el implante cerebral deba comunicarse con otros implantes situados en el propio cuerpo, como por ejemplo en neuroprótesis para pacientes con parálisis con las que el cerebro pueda hacer llegar las órdenes a otras partes del cuerpo de forma inalámbrica.

Para finalizar, en el punto VII se presentan la discusión de los resultados obtenidos y las conclusiones.

II. OBJETIVO

Este trabajo se centra en la primera parte del esquema presentado anteriormente (Fig. 1), la comunicación entre el implante y el dispositivo móvil. Para ello, los objetivos que se deberán perseguir son:

- Definición de los requisitos para la transmisión de señales neuronales de modo inalámbrico: necesidades de capacidad, potencia y calidad del sistema (punto .
- Estudio las tecnologías inalámbricas de corto alcance existentes y selección de la tecnología inalámbrica adecuada.
- Estudio en profundidad del estándar UWB e identificación de sus puntos fuertes y débiles.
- Transmisión de señales neuronales con tecnología UWB y estudio de parámetros de calidad de la transmisión, así como de la recuperación de las señales en recepción.
- Realización de medidas en oficina para modelar el efecto del entorno y del cuerpo en el canal UWB. Viabilidad de la transmisión.
- Elección de parámetros adecuados de transmisión para un correcto envío y recepción de las señales neuronales.

III. ESTADO DEL ARTE

III.1. CAPTACIÓN DE SEÑALES NEURONALES

III.1.1. Señales neuronales

Dado que la aplicación que se pretende desarrollar es la captación y transmisión inalámbrica de señales neuronales, se hará una breve descripción de las características de dichas señales.

Las neuronas emiten impulsos o *spikes*, formando trenes de impulsos. Los patrones de disparo formados en estos trenes de impulsos son los que contienen la información neuronal, codificada en la frecuencia de disparo, amplitud del pulso, etc. Cada uno de estos pulsos tiene una duración de 1

a 3 ms y un voltaje del orden microvoltios [4] [11]. La banda de frecuencias ocupada por cada *spike* es de 100 a 10.000 Hz. En la Fig. 2 puede verse un tren de impulsos captado de un cultivo neuronal por un electrodo, en el que se mezclan señales de varias neuronas cercanas al sensor y ruido.

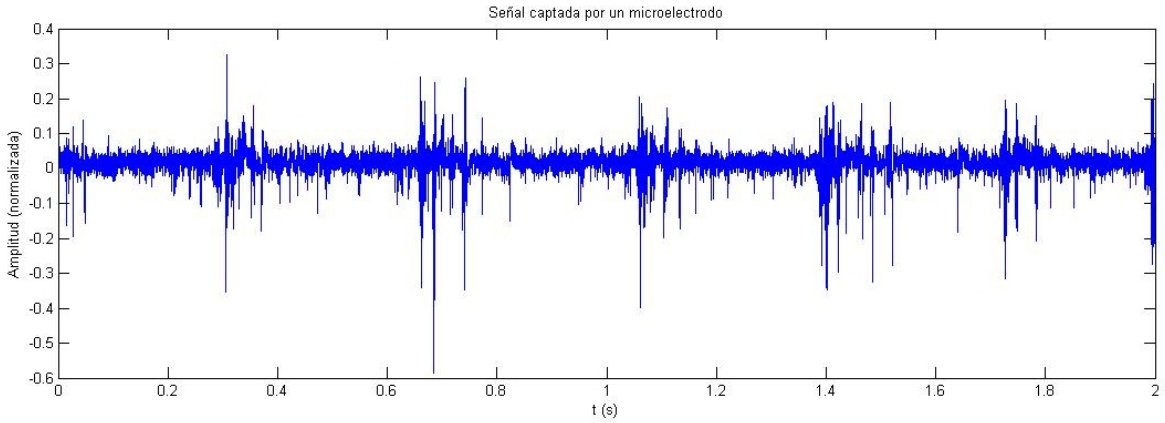

Fig. 2 Señal captada de neuronas cultivadas in-vitro por un microelectrodo

De acuerdo con el contenido frecuencial de estas señales, las frecuencias de muestreo utilizadas varían entre los 15 y los 50kHz. En general a mayor frecuencia de muestreo, se obtiene mayor fidelidad en las señales pero a su vez se genera mayor cantidad de datos a ser procesados o transmitidos por unidad de tiempo, lo cual es problemático en cuanto a capacidad de procesado, de transmisión, consumo, etc. La resolución que se suele utilizar para las muestras de señal es de 10 a 12 bits que proporciona rangos dinámicos de 60-72dB.

III.1.2. Sistemas de captación de señales neuronales y tasa de transmisión

Actualmente existen en el mercado diversos sistemas de captación y adquisición de señales neuronales, tanto para experimentos *in-vivo*, es decir, con electrodos implantables [12], como para experimentos *in-vitro* con cultivos de neuronas [13].

Como ejemplo se mencionarán los sistemas de captación de Multichannel Systems [13]. Esta empresa provee arrays de microelectrodos planares de 64 o incluso de hasta 128 electrodos para captación y adquisición en tiempo real de señales neuronales cultivadas *in-vitro*. El sistema permite captar señales, amplificarlas y adquirirlas en un ordenador y permite la representación gráfica y el análisis de los datos adquiridos. En la Fig. 3 se muestra la representación de las señales adquiridas utilizando el software de Multichannel Systems para un array de 64 electrodos, de los cuales 60 se utilizan para adquisición y 4 para estimulación del cultivo.

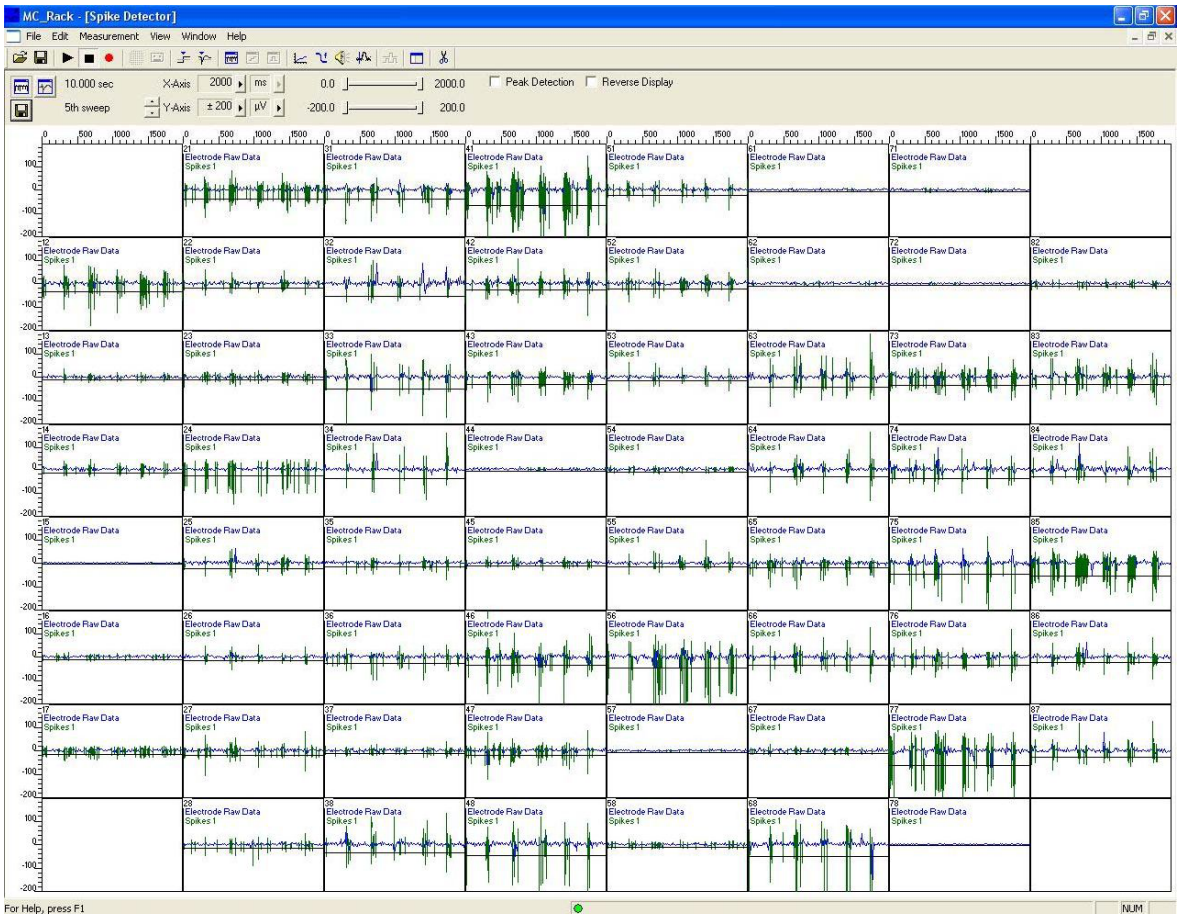

Fig. 3 Software de Multichannel Systems que muestra las señales de 64 canales, correspondientes a un array de 64 microelectrodos

Para un sistema de captación de 60 canales, con las señales muestreadas a 15 kHz y 12 bits por muestra, se estaría generando una tasa de 60*15000*12= 11 Mbps. Si el sistema fuera de 120 canales y se muestreara a 25 kHz, aumentaría a 36 Mbps.

Se supondrá por lo tanto, que la tasa de transmisión debe ser mayor que 10 Mbps y podría llegar a los 40 Mbps.

III.2. TECNOLOGÍAS INALÁMBRICAS DE CORTO ALCANCE

Como se ha comentado anteriormente, la eliminación de cables en dispositivos para pacientes favorece su implantación y aumenta el número de aplicaciones posibles. Ahora bien, habrá que tener en cuenta los requisitos específicos de cada aplicación para poder seleccionar la tecnología inalámbrica adecuada en cada caso. A continuación se realiza un estudio de las principales tecnologías inalámbricas utilizadas en corto alcance y que están siendo consideradas en aplicaciones médicas actualmente, ZigBee [20], Bluetooth [21] y Ultra Wideband [24], y se analizarán sus pros y sus contras para la aplicación actual.

III.2.1. Bluetooth

Bluetooth es la norma que define un estándar global de comunicación inalámbrica que posibilita la transmisión de voz y datos entre diferentes equipos mediante un enlace por radiofrecuencia. Además ofrece la posibilidad de crear pequeñas redes inalámbricas (piconets) de hasta 8 dispositivos y facilitar la sincronización de datos entre los equipos personales.

El SIG (*Special Interest Group*) de Bluetooth [24] es un grupo de compañías que trabajan juntas para desarrollar, promover, definir y publicar las especificaciones de esta tecnología, así como gestionar los programas de calidad.

Las especificaciones de Bluetooth ponen a disposición de los desarrolladores de productos tanto especificaciones para el nivel de enlace como para el de aplicación. La especificación de Bluetooth define un canal de comunicación de máximo 720 kbps con rango óptimo de 10 metros (opcionalmente 100 m). La frecuencia de radio con la que trabaja está en la banda de 2.4 a 2.48 GHz (ISM, no licenciado). Se basa en saltos de frecuencia adaptativos (AFH) evitando así interferencias con otros dispositivos en la misma banda. La potencia de salida para transmitir a una distancia máxima de 10 metros es de 0dBm, mientras que la versión de largo alcance transmite entre 20 y 30 dBm y puede llegar a los 100 metros de alcance.

Buscando ampliar la compatibilidad de los dispositivos Bluetooth, estos utilizan como interfaz entre el dispositivo anfitrión (PC, teléfono celular, etc.) y el dispositivo Bluetooth como tal (chip Bluetooth) una interfaz denominada HCI (*Host Controller Interface*). La versión 2.0, creada para ser una especificación separada, principalmente incorpora la técnica *Enhanced Data Rate* (EDR) que le permite mejorar las velocidades de transmisión en hasta 3 Mbps.

El ahorro de energía es una de las claves de Bluetooth. En la norma se especifica el "*down power*", esto es, una disminución de potencia y consumo durante periodos de inactividad.

Se han investigado numerosas aplicaciones de Bluetooth en el ámbito médico y hospitalario relacionadas con la telemedicina: En [21] y en [22], un dispositivo llevado por el paciente registra los datos (ECG) y los envía por bluetooth a un monitor local o servidor, que está conectado a Internet. En [23] se propone un sistema similar, sólo que los sensores se comunican individualmente con una PDA por bluetooth. Todos ellos tienen en común que utilizan muy pocos sensores, y que por lo tanto, la tasa de transmisión no es muy alta.

III.2.2. ZigBee

Se trata de una especificación de protocolos de comunicaciones diseñados para redes de área personal (*Wireless Personal Area Network*, WPAN), basados en el estándar IEEE 802.15.4 [25]. La *ZigBee Alliance* pone a disposición del público general las especificaciones de esta tecnología que, para uso no comercial, están abiertas a todo el público.

La tecnología está diseñada para ser más económica y simple que otras WPANs, como por ejemplo Bluetooth. El nodo más complejo dentro de una arquitectura ZigBee requiere solamente el

10% del software de uno comparable de Bluetooth. El coste es muy reducido aunque en general hay que añadir el coste de un microcontrolador, que entonces lo hace parecido a un chip de Bluetooth.

Los protocolos definidos por ZigBee son ideales para aplicaciones que requieren velocidades de transmisión bajas y bajo consumo energético. Entre otros, los campos de aplicación son domótica, control industrial, redes de sensores, dispositivos médicos, alarmas o automatización de edificios. El diseño se basa sobre todo en reducir al máximo la potencia y este bajo consumo es el que hace que la tecnología ZigBee tenga un largo periodo de vida sin tener que recargar las baterías.

En general, los protocolos ZigBee minimizan el tiempo durante el cual la transmisión por radio está activa para reducir el consumo. Los nodos solamente se activan para transmitir y recibir cuando hay datos disponibles, aunque en algunas redes algunos dispositivos están constantemente activos mientras otros están dormidos casi todo el tiempo.

Los dispositivos ZigBee deben seguir la norma IEEE 802.15.4-2003 para redes de área personal (*Wireless Personal Area Network* WPAN) de baja velocidad, donde se especifica la capa física, la capa de acceso al medio y el nivel de enlace de datos. Se especifica la operación de dispositivos en las bandas no licenciadas de 2.4 GHz, 915 MHz y 868 MHz (bandas ISM). La velocidad de transmisión de datos es de 250 kbps por canal en la banda de 2.4 GHz, 40 kbps por canal en la banda 915 MHz y 20 kbps en la banda 868 MHz. El alcance de la transmisión está entre 10 y 75 m.

El software de los dispositivos ZigBee está diseñado para poder utilizar microprocesadores de bajo consumo y bajo coste. Así también el diseño RF ha sido optimizado para bajo consumo y bajo coste.

Existen numerosos esfuerzos por desarrollar aplicaciones en el ámbito médico para monitorización de pacientes y generación de alarmas. En [26] se diseña un transceptor ZigBee para sensores y en [27] se propone un sistema de monitorización remota basado en una red de sensores ZigBee alrededor del cuerpo, enviando datos a una PDA. La PDA enviaría los datos al servidor mediante mensajes o GSM, ya que de nuevo, el volumen de datos a transmitir es muy bajo.

III.2.3. UWB

UWB es una tecnología que consiste en la utilización de un gran ancho de banda con una potencia muy baja. Este hecho implica que la banda de frecuencias utilizada en el espectro, solapa con otras bandas ya en uso, pero no interfiere porque la potencia está incluso por debajo del nivel de ruido. Formalmente, se denomina *Ultra Wideband* a toda banda cuyo ancho de banda sea mayor que 500 MHz o cuyo ancho de banda fraccional sea mayor que 20%, definiendo ancho de banda fraccional como:

$$B_f = \frac{2(f_h - f_l)}{f_h + f_l} \times 100\,\% \tag{1}$$

donde f_h es la frecuencia de corte superior y f_l la inferior.

Aunque UWB aparece hoy en día como una tecnología moderna, hay que destacar que la idea original nació hace más de un siglo, en la primera transmisión inalámbrica diseñada por Marconi y Hertz hacia el 1890. Debido a las limitaciones técnicas de la época, la banda estrecha se ha impuesto ante UWB, hasta nuestros días, donde vuelve a cobrar importancia.

En febrero de 2002 se aprobaron las emisiones por el FCC (*Federal Communications Comission,* [28]) de tal forma que el espectro se encuentra entre 3.1 y 10.6 GHz con una potencia isotrópica efectiva radiada de -41.3 dBm/MHz (75nW/MHz). En la Fig. 4 puede verse la máscara espectral asignada a UWB por la FCC. Actualmente existen sistemas basados en la transmisión de impulsos de muy corta duración, y por lo tanto muy extendidos en el espectro, llamados *Impulse Radio UWB* (IR-UWB), así como sistemas de modulación por división de frecuencias ortogonales OFDM (OFDM-UWB). Se han desarrollado dos estándares en competencia: OFDM-UWB e IR-UWB, que se discutirán con más detalle en el punto IV.

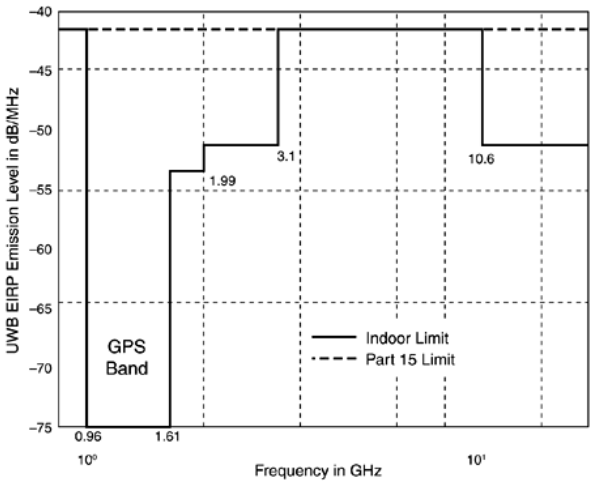

Fig. 4 Máscara espectral para transmisión en interiores (*indoor*) asignada a UWB por la FCC

III.2.4. Comparación

A continuación se muestra una tabla que resume las cualidades de las tecnologías inalámbricas elegidas.

	Tasa de tx	**Alcance**	**Banda frec.**	**Potencia tx**	**Implantable**
ZigBee	250 kbps	100 m	2.4 GHz	Muy baja	No
Bluetooth	720 kbps	100 m	2.4 GHz	Baja	Sí
UWB	>100 Mbps	10 m	3.1- 10.6 GHz	Muy baja	Sí

Tabla 1: Comparación entre distintas tecnologías inalámbricas para BAN

Podemos observar cómo ZigBee sacrifica velocidad de transmisión a cambio de una potencia muy baja y, por lo tanto, muy bajo consumo. Bluetooth, en cambio, posee una velocidad de transmisión mayor, aunque no es comparable con las velocidades alcanzadas por UWB.

Para nuestro objetivo concreto, tal y como se mostró en el punto III.1.2, el volumen de datos a transmitir es muy alto, con lo que ZigBee no cumple los requisitos de ancho de banda. La potencia de transmisión para un dispositivo implantable deberá ser lo menor posible, por lo que se ha elegido UWB ante Bluetooth. Además, la banda de frecuencias de Bluetooth es una banda sin licencia, bastante saturada, mientras que la de UWB pertenece a la banda ISM (*Industrial, Scientific and Medical*), específica para aplicaciones médicas.

Por lo tanto, UWB consigue los dos objetivos fundamentales que son alta velocidad y baja potencia, aunque hemos de tener en cuenta que su estandarización aún no está cerrada y que actualmente no existen dispositivos comerciales que implementen esta tecnología.

IV. LA TECNOLOGÍA UWB

IV.1. OFDM-UWB VS IR-UWB

Como se ha comentado anteriormente, dos tecnologías UWB compiten por el estándar 802.15.3a. Ambas se basan en conseguir ocupar una banda ancha del espectro con muy baja potencia, pero cada una de ellas lo hace de un modo muy diferente.

OFDM-UWB utiliza modulación multibanda OFDM (*Orthogonal Frequency-Division Multiplexing*) que consigue un gran ancho de banda como unión de muchas subbandas más estrechas y con muy poca interferencia entre símbolos, debido a que las subbandas de frecuencias son ortogonales entre sí. Una de las ventajas que ofrece la modulación multibanda es la posibilidad de no transmitir en ciertas subbandas para prevenir o evitar interferencias, lo que hace a OFDM-UWB flexible y escalable.

Otra de las ventajas de esta modulación es su posible implementación mediante la FFT (*Fast Fourier Transform*), lo que es rápido y sencillo, aunque por otro lado la FFT requiere procesado y por lo tanto potencia.

En IR-UWB la señal consiste en series de pulsos con un ciclo de trabajo muy bajo, menos de un 0.5%. El ancho del pulso en el tiempo es muy estrecho, típicamente nanosegundos, lo que resulta en el espectro un ancho de banda muy grande y una mejor resolución para multicamino en los canales UWB. Esta implementación no usa portadora, por lo que la circuitería RF es más sencilla. Por otro lado, el manejo de pulsos de tan corta duración obliga a trabajar a frecuencias de procesado muy altas. Además se requiere una extremada precisión en la sincronización y también una alta velocidad de conmutación entre envío y recepción en los transceptores.

Con IR-UWB podemos conseguir que no haya interferencia entre pulsos si hacemos que el intervalo de repetición de pulsos sea mayor que el *delay spread* del canal, mientras que en OFDM-UWB, si las subbandas son lo suficientemente estrechas (menores que el ancho de banda de coherencia del canal), podemos suponer canales planos sin selectividad en frecuencia.

Actualmente, algunas marcas comerciales han comenzado a lanzar sus productos y la mayoría de ellos se han decantado por OFDM-UWB. OFDM-UWB parece ser la tecnología dominante en comunicaciones, mientras que IR-UWB es muy interesante para aplicaciones tipo radar, ya que gracias a sus pulsos ultra-cortos consigue una resolución temporal muy fina y por lo tanto, una precisión de localización muy alta.

La bibliografía sobre UWB no es muy extensa, aunque ya existen algunos libros específicos donde puede encontrarse información, como por ejemplo [1], [2], [3].

IV.2. EL ESTÁNDAR DE WIMEDIA

Para una futura implementación de la aplicación se pretende elegir una tecnología que tenga un estándar definido y esté implementada en productos comerciales, de modo que no se necesite diseñar un hardware específico. El estándar de WiMedia, respaldado por la WiMedia Alliance [29], utiliza OFDM-UWB y es el más extendido en estos momentos. Es de esperar que en algunos años venga integrado en los dispositivos móviles tal y como ahora está el Bluetooth. Se detallarán a continuación algunas de sus especificaciones en cuanto a velocidades de transmisión, bandas de frecuencias y acceso al medio.

Para el rango de frecuencias que van desde los 3.1 a los 10.6 GHz, el espectro se divide en 14 bandas, cada una con un ancho de banda de 528 MHz. Estas bandas se agrupan en 5 grupos, de 3 bandas cada una excepto la 5ª, que tiene 2. En la Fig. 5 puede verse la distribución de las bandas y sus frecuencias centrales. Cada banda usa OFDM con un total de 110 subportadoras (100 de datos y 10 de guarda). Además posee 12 subportadoras para detección coherente. Cada una de estas portadoras se modula a su vez en QPSK (*Quadrature Phase Shift Keying*) o en DCM (*Dual Carrier Modulation*).

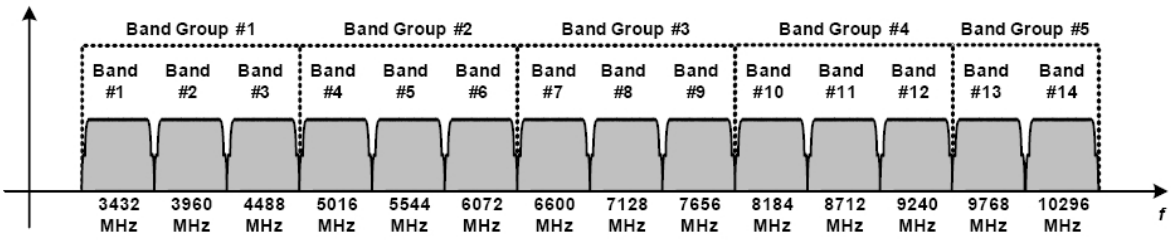

Fig. 5 Localización de las bandas de frecuencias asignadas a UWB

La tasa de transmisión para los datos es seleccionable entre un conjunto dado: 53.3, 80, 106.7, 160, 200, 320, 400 y 480 Mbps. Estas tasas se consiguen variando la modulación y con el uso de ensanchamiento frecuencial (*frecuency-domain spreading*, FDS), ensanchamiento temporal (*time-domain spreading*, TDS) y codificación con corrección de errores (*Forward Error Correction*, FEC). Los códigos usados son códigos convolucionales con tasas 1/2, 1/3, 5/8 y 3/4.

Tasa transmisión (Mbps)	**Modulación**	**Tasa de codificación (R)**	**FDS**	**TDS**
53.3	QPSK	1/3	Sí	Sí
80	QPSK	1/2	Sí	Sí
106.7	QPSK	1/3	No	Sí
160	QPSK	1/2	No	Sí
200	QPSK	5/8	No	Sí
320	DCM	1/2	No	No
400	DCM	5/8	No	No
480	DCM	3/4	No	No

Tabla 2 Parámetros de los que depende la tasa de transmisión

En la Tabla 2 se muestran las configuraciones para cada una de las velocidades de transmisión.

La capa de acceso al medio (MAC, *Media Access Control*) asegura un comparto equitativo del ancho de banda de la red. La MAC provee esquemas de priorización para tráfico síncrono y asíncrono. Para hacer esto se usa una combinación de CSMA (*Carrier Sense Multiple Access*) y TDMA (*Time Division Multiple Access*), es decir, escuchar el medio para saber si existe presencia de portadora en los momentos en los que se ocupa el canal con el fin de evitar colisiones y además tener periodos temporales asignados para la transmisión. Para la escalabilidad de la red, ofrece PCA (*Priorized Contention Access*) usando un esquema CSMA, donde el tráfico prioritario escucha durante un periodo menor de tiempo antes de transmitir.

V. TRANSMISIÓN DE SEÑALES NEURONALES CON UWB

Las señales neuronales transmitidas en tiempo real generan una tasa de transmisión (calculada en el punto III.1.2) demasiado elevada para la mayoría de sistemas de transmisión inalámbrica actuales. UWB nos proporciona velocidades teóricas muy altas que en la práctica no se alcanzan puesto que existen elementos que afectan al sistema como el ruido, el multicamino, la dispersión, la interferencia de otros dispositivos, etc. Las velocidades alcanzadas con UWB son de todos modos muy superiores a las de otras tecnologías.

A continuación se explicará el montaje y desarrollo de un experimento que pretende medir las pérdidas (*Bit Error Rate*, BER) sufridas por una señal neuronal en un enlace UWB y la implicación

que estas pérdidas tienen en la detección de los *spikes* neuronales, así como decidir la tasa óptima de transmisión.

Las señales neuronales, como se dijo en el punto III.1.1, son básicamente trenes de impulsos mezclados con ruido. Separar estos impulsos del ruido requiere de un detector capaz de detectar estos impulsos, por ejemplo, utilizando un umbral fijo o adaptativo. Para medir la calidad de un detector se utilizan las curvas ROC (*Receiver Operating Characteristic*), que nos dan la probabilidad de detección (pd) con respecto a la probabilidad de falsa alarma (pfa). La curva ROC ideal es la función escalón, donde para cualquier probabilidad de detección, la pfa es siempre cero. El parámetro que se utilizará para comparar curvas ROC será el área bajo la curva (*Area Under the Curve*, AUC), que para la ROC ideal es 1.

V.1. DESCRIPCIÓN DEL MONTAJE

Para la realización de las medidas se ha utilizado un kit de desarrollo para la transmisión UWB, concretamente el DVK DV9110M de la empresa Wisair y que implementa el estándar WiMedia. La banda de frecuencias que utiliza es la definida como Grupo de Bandas 1, que son 3 bandas situadas desde 3.168 a 4.752 GHz. La potencia de salida son 80μW/MHz (-42 dBm/MHz como máximo). El kit de desarrollo consta de dos equipos capaces de enviar y transmitir, provistos con antenas UWB omnidireccionales.

Estos equipos se han colocado sobre mesas de oficina a 1, 2 y 3 metros de distancia sucesivamente y para cada una de estas distancias, se han elegido las configuraciones de 53.3, 80 y 106.7 Mbps, lo que llamaremos “velocidad del kit” o “velocidad máxima teórica”. Las medidas han consistido en enviar un archivo que contiene una señal neuronal en binario, programando distintas velocidades de envío, siempre por debajo de la teórica.

Para cada una de las velocidades del kit y velocidades de envío, se ha enviado la señal 100 veces para obtener 100 archivos recibidos y poder sacar resultados en media.

La transmisión se realiza mediante un programa escrito en *c*, que trocea el archivo en paquetes y envía un determinado número de paquetes por segundo. La velocidad de transmisión puede ajustarse así modificando el tamaño del paquete. El protocolo utilizado es UDP, que no garantiza la recepción de todos los paquetes ni el orden correcto, pero que es rápido y eficaz para transmisión en tiempo real.

V.2. RESULTADOS

V.2.1. BER

En la Fig. 6 se muestra representada la señal original (izquierda) y un ejemplo de señal recibida (derecha). La señal recibida presenta espacios en blanco que son los paquetes que no se han recibido correctamente. Se comprueba que cuando hay pérdidas, siempre se pierden segmentos de

la señal, pero nunca hay bits recibidos erróneos. Esto es debido a que estamos utilizando un equipo de UWB con el estándar WiMedia, donde las capas física y de enlace implementan detección de errores y directamente van a descartar los paquetes erróneos enteros.

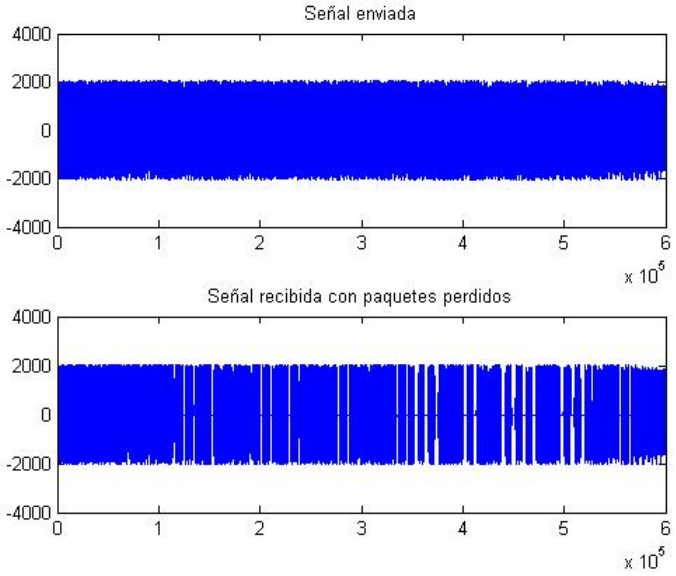

Fig. 6 Señal original y señal recibida con paquetes perdidos

La *Bit Error Rate* (BER) o tasa de error de bit se calcula dividiendo el número de bits recibidos entre el número total de bits enviados.

$$BER = \frac{bits\ \ recibidos}{bits\ \ enviados} \tag{2}$$

Aunque en este caso podríamos haber utilizado la tasa de error de paquete (PER), hay que destacar que las BER obtenidas coinciden prácticamente con las PER ya que si se recibe un paquete, se habrán recibido los *n* bits correctos y por lo tanto la relación bits recibidos a bits enviados es la misma que paquetes recibidos a paquetes enviados.

$$BER = \frac{bits\ \ recibidos}{bits\ \ enviados} = \frac{n * paquetes\ \ \ recibidos}{n * paquetes\ \ \ enviados} = \frac{paquetes\ \ \ recibidos}{paquetes\ \ \ enviados} = PER \tag{3}$$

La única diferencia sería en el último paquete enviado, que puede ser de tamaño menor al resto y que variaría ligeramente el resultado. Se ha preferido utilizar la BER por ser un parámetro más común en la caracterización de canales de comunicación.

La BER mostrada en las figuras Fig. 7 a Fig. 9 es la media de las 100 BERs calculadas (ya que se realizan 100 envíos de la señal) para cada velocidad de transmisión. Se ha configurado el kit para una velocidad de 53.3 Mbps (Fig. 7), 80 Mbps (Fig. 8) y 106.7 Mbps (Fig. 9). Cuando la velocidad de envío es baja con respecto a la máxima, la BER es muy baja, mientras que si nos acercamos a la máxima velocidad teórica, la BER aumenta. Además vemos que de 1 a 2 metros, el aumento de la BER no es muy significativo y con 3 metros ya se observa una diferencia, ya que la BER pasa de estar entorno a 0.01 a llegar hasta 0.06.

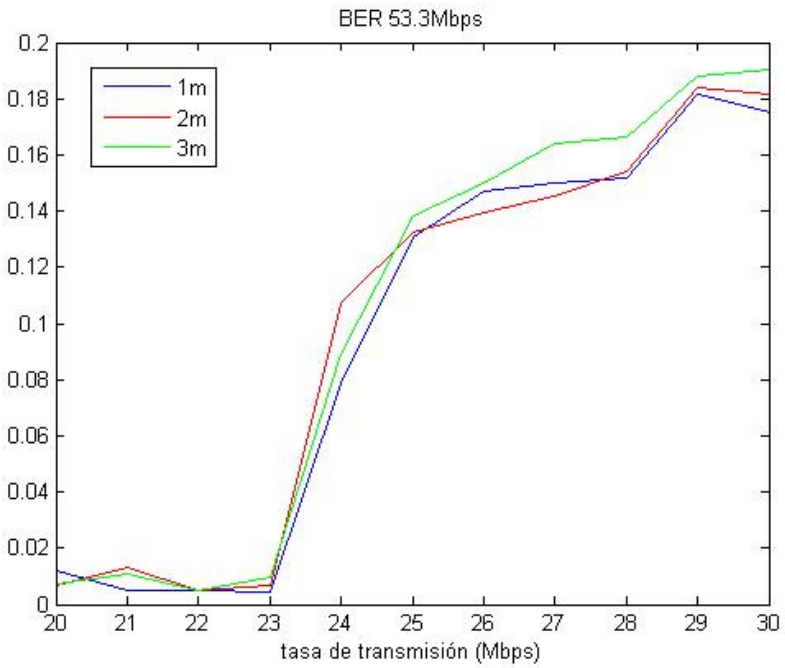

Fig. 7 BER calculada para una velocidad máxima de 53.3 Mbps para 1, 2 y 3 metros de separación

En las tres figuras se observa un punto en el que la BER comienza a incrementarse muy rápidamente. Las pérdidas de paquetes a partir de ese punto son causadas por limitaciones del hardware. Si nos fijamos en una cierta distancia, a 1 metro se observa que para 53.3 Mbps las pérdidas de paquetes comienzan cuando transmitimos a una velocidad mayor de 23 Mbps. Si se aumenta la velocidad máxima teórica a 80 Mbps, las velocidades de transmisión pueden ser mayores y las pérdidas de paquetes comienzan a ser significativas a partir de los 31 Mbps. Nuevamente se observa que podemos desplazar el punto hasta los 40 Mbps aumentando la velocidad del kit a 106.7 Mbps.

Para 2 y 3 metros se reduce un poco la velocidad a la que aumenta la BER pero tampoco es muy significativo ya que, como se dijo anteriormente, la mayor pérdida de paquetes se debe a que al pasar una cierta velocidad de transmisión, nos vemos limitados por hardware, con lo que es lógico que la distancia influya poco en este punto.

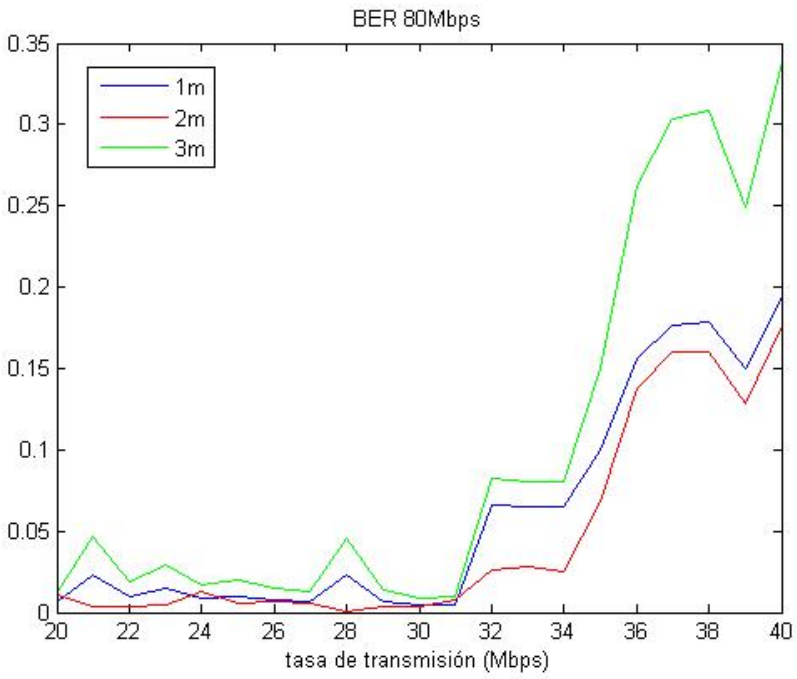

Fig. 8 BER calculada para una velocidad máxima de 80 Mbps para 1, 2 y 3 metros de separación

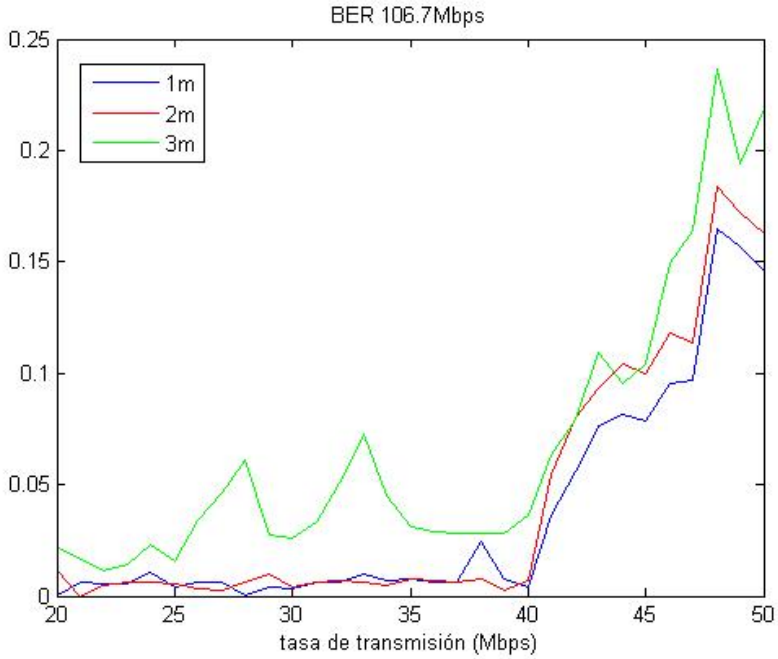

Fig. 9 BER calculada para una velocidad máxima de 106.7 Mbps para 1, 2 y 3 metros de separación

V.2.2. ROC y área bajo la curva

Las curvas ROC nos sirven para medir la calidad de la detección de un determinado detector, o para comparar la calidad de diferentes detectores frente a una señal. En nuestro caso, estudiaremos el efecto de la transmisión en la detección de *spikes*, con lo que nos interesará comparar las curvas

ROC antes y después de la transmisión. La comparación se hará mediante el área bajo la curva, que nos servirá para caracterizar la degradación de la calidad de la detección.

En la Fig. 10 (a) puede verse como ejemplo, la curva ROC de la señal original transmitida, con un área bajo la curva de 0.9795. Las siguientes curvas muestran la ROC media (calculada como el promedio de las 100 curvas ROC calculadas para las 100 recepciones de cada configuración) de una señal transmitida a 20Mbps (b) y de otra transmitida a 30 Mbps (c) para una velocidad de transmisión del kit de 53.5Mbps. El efecto de la transmisión y la pérdida de paquetes se reflejan en las curvas ROC como una saturación, ya que se han perdido *spikes* que no podremos detectar. Se observa cómo a 20 Mbps el área es prácticamente la misma, 0.95, pero para la de 30 Mbps empeora bastante la deteción y por lo tanto disminuye hasta 0.7097.

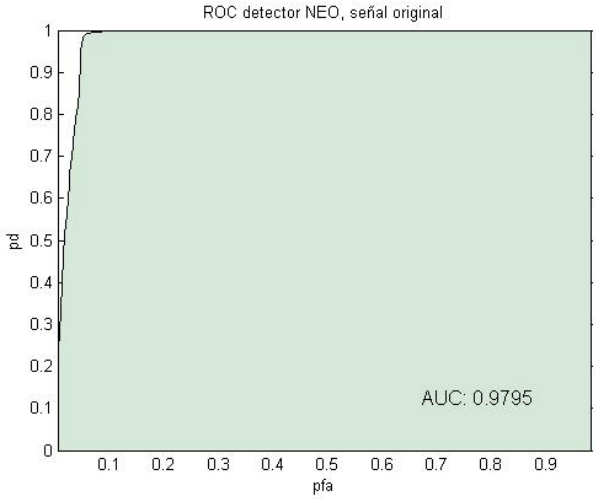

(a)

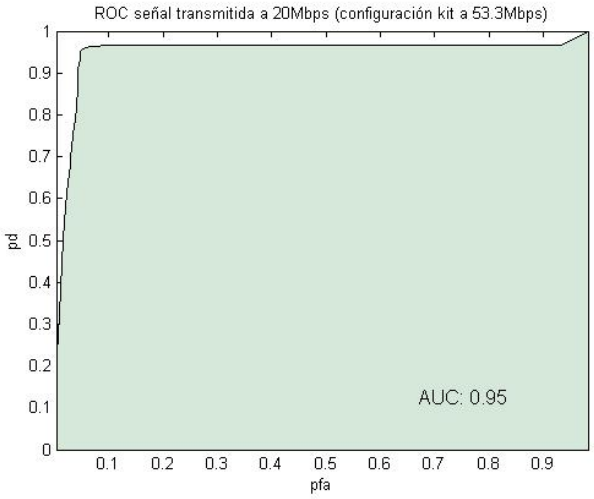

(b)

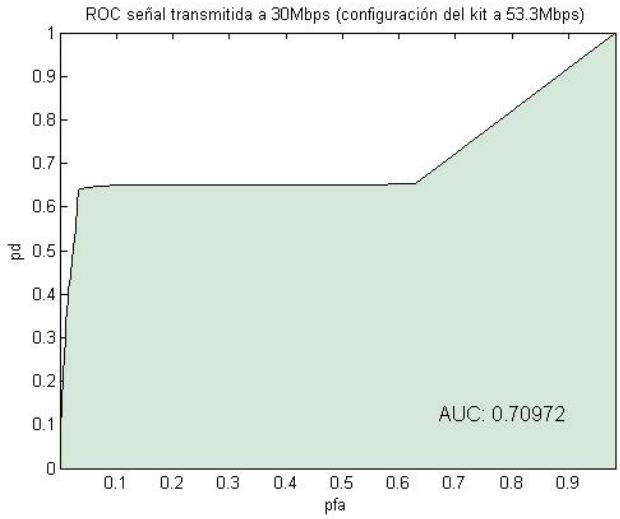

(c)

Fig. 10 Curvas ROC utilizando la señal original antes de ser transmitida (a) y tras enviarla a 20 (b) y 30 Mbps (c) con el kit de UWB configurado a 53.3 Mbps.

La Fig. 11 muestra las áreas bajo la curva para todas las medidas realizadas. Puede verse que es coherente que al acercarnos a la velocidad máxima teórica, empeore la detección.

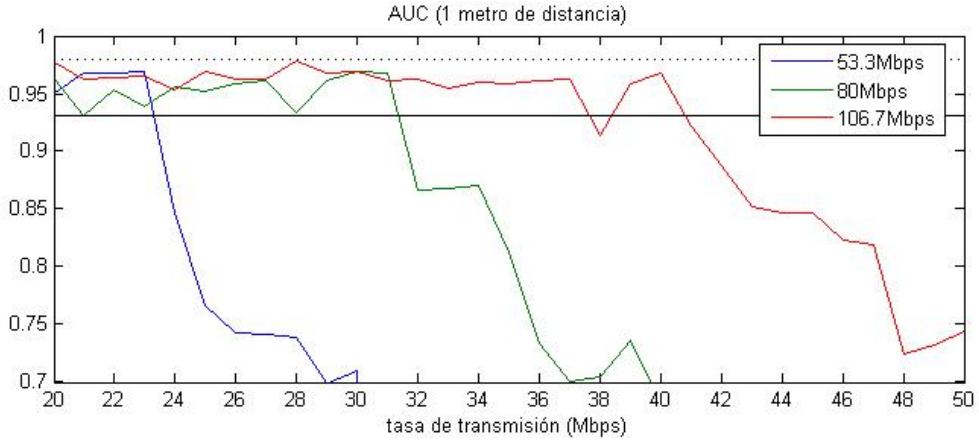

Fig. 11 Área bajo la curva para las tres configuraciones y a una distancia de 1 metro.

En línea discontinua se marca AUC = 0.9795, la máxima AUC posible obtenida de la señal completa antes de ser enviada. Para una calidad aceptable, se ha limitado el AUC a un 5% menor del área máxima, lo que da un AUC límite de 0.9305. En la Fig. 11 se muestra dicho límite con una línea negra y todas las velocidades que nos den una AUC por debajo de esta línea no cumplirían los requisitos de calidad y no serían aptas para la transmisión. Del mismo modo, las medidas para 2 y 3 metros de distancia se observan en la Fig. 12 y la Fig. 13, respectivamente.

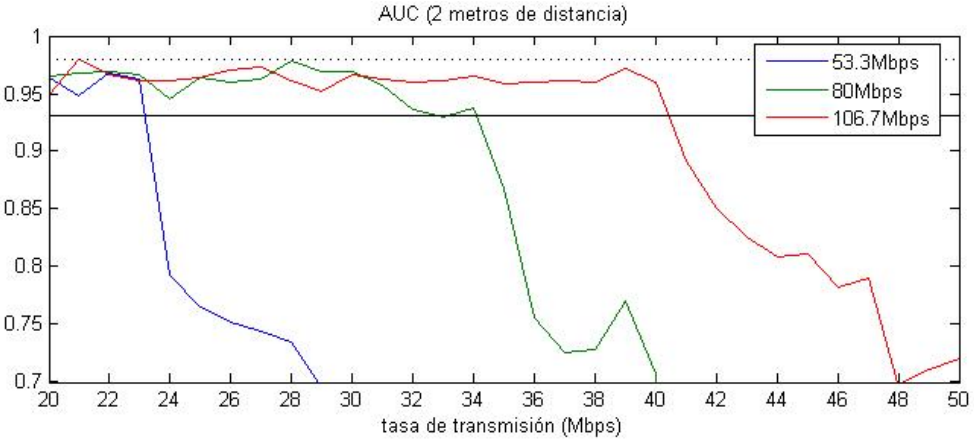

Fig. 12 Área bajo la curva para las tres configuraciones y a una distancia de 2 metros

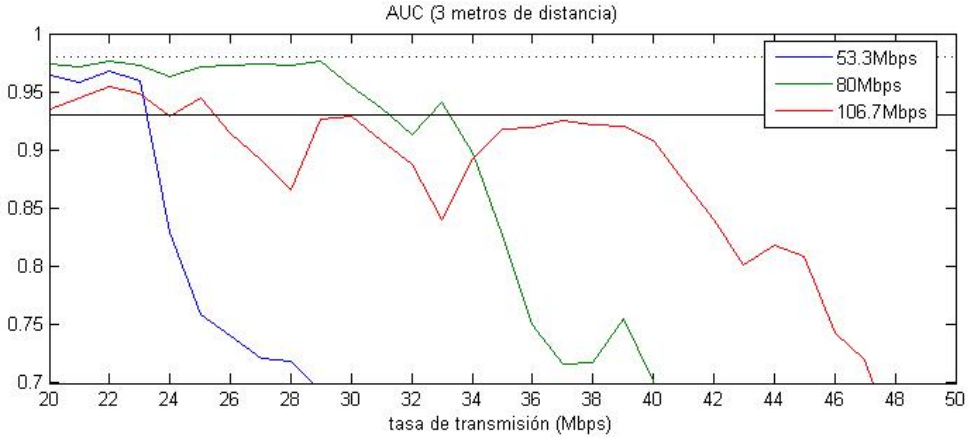

Fig. 13 Área bajo la curva para las tres configuraciones y a una distancia de 3 metros

En la Tabla 3 se muestran la tasa máxima (en Mbps) a la que se podría transmitir para cada configuración y distancia.

	53.3 Mbps	**80 Mbps**	**106.7 Mbps**
1 metro	23	31	37
2 metros	23	32	40
3 metros	23	31	24

Tabla 3 Tasas máximas de transmisión (en Mbps) para una AUC límite 5% menor que el AUC máximo

Vemos que para 53.3 Mbps, la tasa de transmisión es de 23 Mbps y para 80 es de 31 Mbps, bastante constantes en ambos casos. La configuración de 106.7 Mbps es la más irregular, ya que tiene velocidades con picos de caída de AUC. Para 3 metros de distancia a esta velocidad, la caída del área bajo la curva es muy rápida, lo que nos da una tasa de transmisión de tan solo 24 Mbps. Esto es debido a que cuando aumentamos la velocidad teórica del kit, estamos cambiando parámetros como la tasa de codificación o el uso de ensanchamiento frecuencial para conseguir una

velocidad mayor a costa de menor redundancia. Por ello, estos cambios afectan negativamente cuando aumentamos la distancia del enlace, donde hay más errores y menos protección ante ellos.

Dada la frecuencia de disparo de los *spikes* utilizados (50 Hz), en todos los paquetes enviados se encuentran impulsos neuronales, con lo que pérdidas de paquetes se traducen directamente en una degradación de la curva ROC. Sin embargo, si disminuyéramos la frecuencia de disparo (o el tamaño del paquete), podría darse el caso de que en algunos paquetes no hubiera *spikes*, lo que significaría que la BER y la AUC no se degradarían del mismo modo. Como ejemplo, se ha realizado una transmisión UWB a 2 metros de una señal escalón. Una vez recibida, esta señal nos va a dar una "máscara", como se observa en la Fig. 14, de los paquetes perdidos. Multiplicando esta máscara por una señal artificial con neuronas disparando a 50 Hz y por otra señal a 3 Hz, se obtienen dos señales con una misma BER, que, sin embargo, según se muestra en la Fig. 15, no tienen la misma AUC.

Fig. 14 Ejemplo de máscara

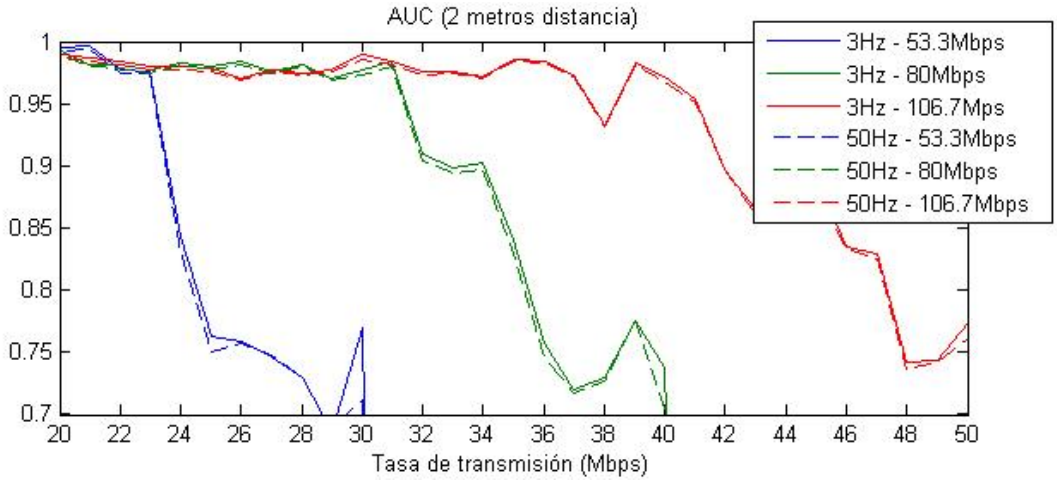

Fig. 15 Área bajo la curva para una señal con *spikes* a 3Hz y otra a 50Hz y misma BER

Como era de esperar, la señal con menor tasa de *spikes* tiene una AUC mayor, ya que aunque ambas hayan perdido el mismo número de paquetes, la de 50 Hz pierde más información por paquete. Cabe destacar, que una frecuencia de disparo de 3 Hz es bastante baja para la actividad neuronal normal.

Sobre la variabilidad de los resultados podemos decir que la campaña de medidas fue realizada en dos días distintos y que el segundo día dio resultados ligeramente peores en general. Aún

cuando las antenas se están apuntando directamente, los cambios en el entorno afectan a las medidas.

En general y teniendo en cuenta que sólo se han utilizado las 3 velocidades más bajas de UWB, podemos decir que puede encontrarse una configuración adecuada que permita la transmisión de datos a la tasa que requieren nuestras señales neuronales.

VI. CANAL UWB EN ENTORNO CORPORAL

Tras el estudio de las velocidades de transmisión adecuadas y el efecto de la pérdida de paquetes en la transmisión UWB, se necesita conocer cómo es el canal en el que se va a realizar dicha transmisión. Para ello, se han realizado diferentes medidas para caracterizar los parámetros más importantes de un canal de comunicaciones.

Diversos estudios sobre canal UWB han sido llevados a cabo, como por ejemplo en [14] o [15]. Más concretamente en el tema del entorno corporal, pueden encontrarse investigaciones sobre la influencia del tipo de antena a utilizar ([16], [17]), así como sobre redes de sensores colocados sobre el cuerpo [18], [19].

En nuestro caso, el interés de estas medidas se centra en conocer el efecto del cuerpo y del entorno, ya que se pretende estudiar una situación real a las frecuencias de UWB.

En el punto VI.1.1 se describe el montaje realizado para las medidas, así como los dos casos tenidos en cuenta: enlace dispositivo implantable a móvil y enlace dispositivo implantable a implantable. Los resultados obtenidos para cada caso, se describen en los puntos VI.1.2 y VI.1.3.

VI.1. MEDIDAS EN OFICINA

VI.1.1. Descripción del montaje

Montaje y medidas se han realizado en una oficina de tamaño grande (8 m x 17 m) con mobiliario típico de oficina: escritorios, ordenadores, armarios metálicos, etc.

El equipo utilizado ha sido un analizador vectorial de redes (VNA), en concreto el modelo ZVA24 de Rhode & Schwarz. Este analizador permite medir magnitud y fase de una señal desde 10 MHz hasta 24 GHz con un rango dinámico de hasta 135 dB. Dos antenas se han conectado al VNA mediante cables RG-223 de 5 metros. Estos cables son apropiados para trabajar a frecuencias de hasta 12.4 GHz y su atenuación no afecta a la medida, puesto que previamente se realiza un calibrado.

El montaje se ha usado para medir la función de transferencia de frecuencia compleja del canal, (parámetro S_{21}) para un rango de frecuencias que van desde los 3 a los 6 GHz.

Para cada canal se han tomado 200 medidas de 2001 puntos discretos de frecuencia en el rango de 3 a 6 GHz. Para asegurar suficiente rango dinámico, se ha transmitido con una frecuencia de 0 dBm y para recoger incluso las reflexiones más lejanas, se han registrado 600 ns de señal.

Finalmente, se ha tomado la media de las 200 medidas para reducir el error debido a la variabilidad del canal.

Las medidas se han realizado sobre un sujeto sobre el cual se iban situando las antenas en las distintas posiciones. Se han definido diferentes canales o caminos entre un transmisor y un receptor, según donde se coloquen. La antena transmisora se ha situado en cuatro posiciones distintas: encima de la cabeza, en el lado izquierdo, en la parte trasera y en el lado derecho. Con respecto a la antena receptora, se han estudiado dos casos según si el receptor se suponía un móvil o un implante en el cuerpo:

Caso 1: Receptor dispositivo móvil

Se han realizado medidas para 6 posiciones: en la mano con el brazo extendido, semiextendido, doblado, hablando por teléfono, en el bolsillo delantero y en el trasero. Estas localizaciones para las antenas transmisora y receptora pueden verse en la Fig. 15. Las combinaciones de las distintas posiciones dan un total de 24 canales de propagación medidos.

En la Tabla 4 pueden verse las combinaciones de transmisor y receptor para obtener los 24 canales, con la numeración que se le ha dado a cada canal y la distancia del canal.

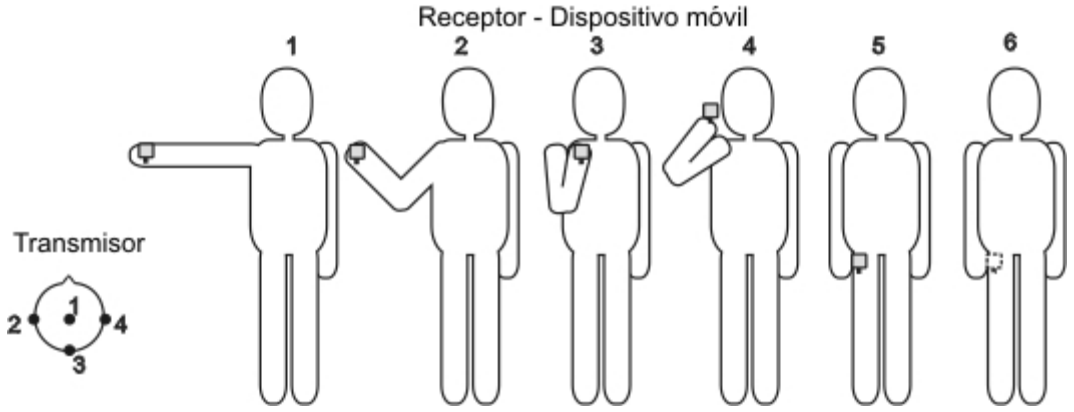

Fig. 16 Posiciones del transmisor y del receptor para la configuración de dispositivo móvil

		rx1 (extendido)	**rx2** (semi-extendido)	**rx3** (doblado)	**rx4** (hablando)	**rx5** (bolsillo delantero)	**rx6** (bolsillo trasero)
tx1 (arriba)	Canal	1	2	3	4	5	6
	d [m]	0,84	0,50	0,37	0,20	0,85	0,92
tx2 (izquierda)	Canal	7	8	9	10	11	12
	d [m]	0,86	0,50	0,30	0,22	0,80	0,85
tx3 (atrás)	Canal	13	14	15	16	17	18
	d [m]	0,80	0,46	0,33	0,16	0,80	0,80
tx4 (derecha)	Canal	19	20	21	22	23	24
	d [m]	0,70	0,38	0,26	0,60	0,70	0,78

Tabla 4 Relación de canales con la numeración asignada y la distancia entre transmisor y dispositivo móvil

Para esta configuración se han realizado dos tandas de medidas con dos tipos de antenas UWB omnidireccionales para poder comparar medidas y ver si son coherentes. Las antenas utilizadas han sido un par de antenas proporcionadas por la empresa Wisair y un par de antenas diseñadas y manufacturadas en el iTEAM.

Caso 2: Receptor - Dispositivo implantable

Se han realizado medidas para 12 posiciones (8 delanteras y 4 traseras) que se muestran en la Fig. 16. Las combinaciones de las distintas posiciones de transmisor y receptor dan un total de 48 canales de propagación. Las distancias de los enlaces se muestran en la Tabla 5. Estas medidas han sido realizadas con las antenas manufacturadas por el iTEAM, que pueden considerarse antenas omnidireccionales en el rango de frecuencias de UWB que se va a medir.

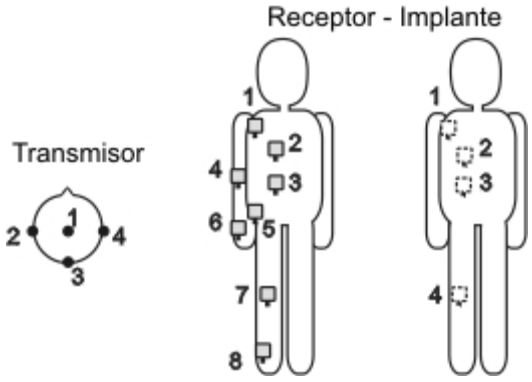

Fig. 17 Posiciones del transmisor y del receptor para la configuración de dispositivo implantable

Posición receptor	Número de canal	Distancia del enlace [m]			
		Tx1	Tx2	Tx3	Tx4
Delante	1	0.35	0.33	0.3	0.2
	2	0.4	0.36	0.35	0.3
	3	0.6	0.5	0.5	0.5
	4	0.7	0.65	0.55	0.57
	5	0.8	0.7	0.7	0.6
	6	0.9	0.85	0.8	0.77
	7	1.25	1.05	1.1	1.1
	8	1.6	1.5	1.4	1.4
Detrás	1	0.42	0.35	0.27	0.3
	2	0.5	0.4	0.32	0.4
	3	0.7	0.55	0.5	0.54
	4	1.25	1.1	1	1.1

Tabla 5 Relación de canales con la numeración asignada y la distancia entre transmisor e implante receptor

VI.1.2. Caso 1: Dispositivo móvil

Path loss

El *path loss* o atenuación con la distancia se define como:

$$L = 10n\log_{10}(d) \tag{4}$$

donde *n* es el exponente de atenuación y *d* es la distancia del enlace.

En la Fig. 18 se muestra el *path loss* de los 24 canales ordenados según distancia, en escala logarítmica y normalizada a la mínima distancia (20 cm) para cada una de las parejas de antenas. En color rojo aparecen las antenas fabricadas en el iTEAM y en azul las de Wisair. También se muestra el modelo lineal que mejor ajusta los puntos y se puede observar que es coherente para ambas antenas.

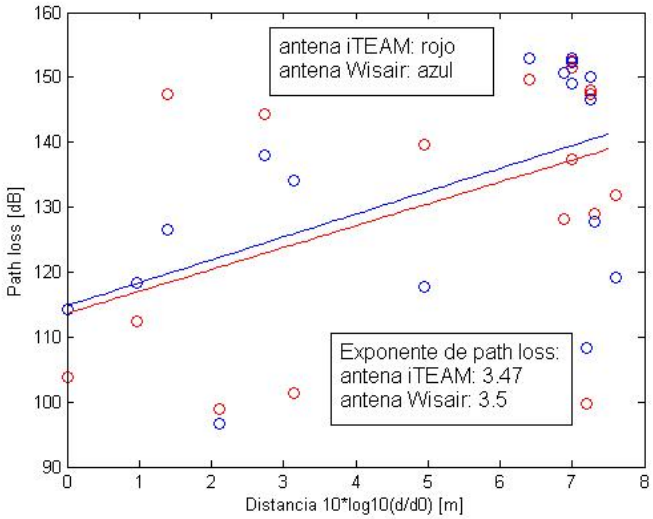

Fig. 18 Path loss para los dos tipos de antena, con la aproximación lineal que mejor ajusta

Los exponentes de atenuación obtenidos son de 3.47 para la antena del iTEAM y 3.5 para la de Wisair y la variabilidad de las medidas es de 55 dB. La diferencia existente entre los exponentes de atenuación es debida a pequeños cambios en el entorno a la hora de realizar las medidas con cada una de las antenas.

Averaged Power Delay Profile (APDP)

Se define como

$$P(\tau) = E[|s(\tau)|^2] \tag{5}$$

siendo τ la variable retardo y *s(t)* la señal recibida.

En la Fig. 18, se muestran para las 4 posiciones del transmisor, el APDP para cada uno de los canales correspondientes a las 6 posiciones del receptor. Los APDPs correspondientes a cada par de antenas están agrupados juntos.

Los canales están ordenados de menor a mayor distancia del enlace y etiquetados con su correspondiente número de canal (ver Tabla 5) y tipo de antena en el eje *y*.

Se puede observar una primera concentración de señal de 1 a 6 ns, correspondiente a las contribuciones directas o muy cercanas al cuerpo, mientras que los picos a partir de 8 ns son debidos a reflexiones en el entorno. También vemos que la posición del primer pico recibido se desplaza gradualmente de 1 a 4 ns cuando la distancia del enlace aumenta.

Las primeras contribuciones recibidas a los 8 ns son debidas a las reflexiones en suelo y techo. Con respecto a la comparación entre antenas, se puede observar que aunque en general los resultados son muy similares para ambas antenas, la antena de Wisair muestra una mayor ganancia para algunas de las posiciones (por ejemplo, transmisor 2) que la genérica del iTEAM. Esto puede ser debido a diferencias en el diagrama de radiación, que no es completamente omnidireccional en todas las direcciones.

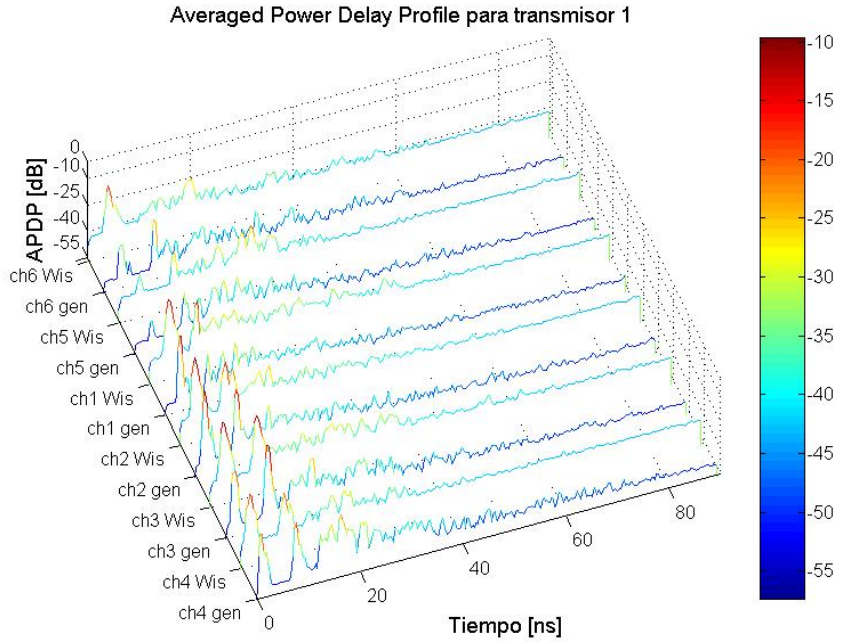

(a)

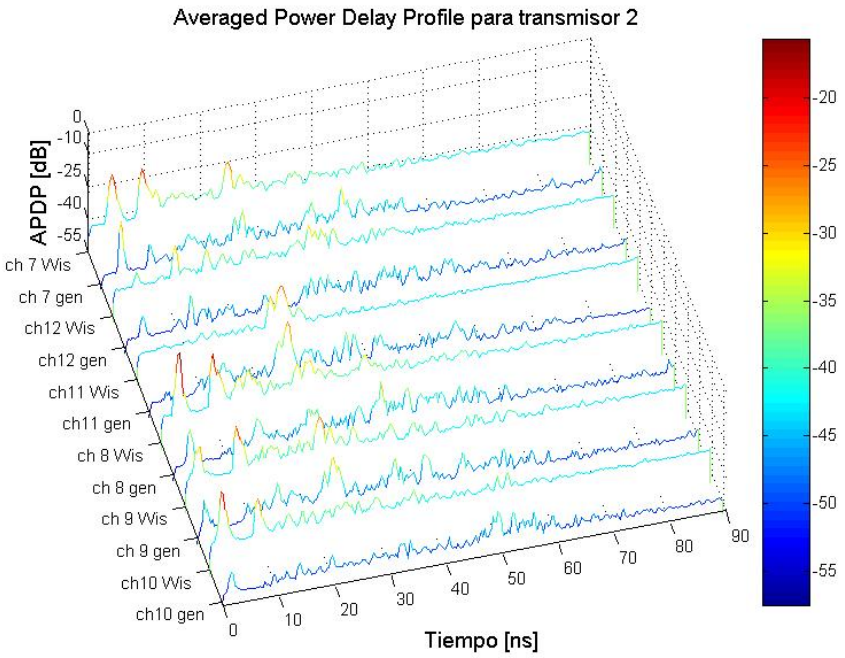
Averaged Power Delay Profile para transmisor 2
APDP [dB]
0
-10
-25
-40
-55
ch 7 Wis
ch 7 gen
ch12 Wis
ch12 gen
ch11 Wis
ch11 gen
ch 8 Wis
ch 8 gen
ch 9 Wis
ch 9 gen
ch10 Wis
ch10 gen
0
10
20
30
40
50
60
70
80
90
Tiempo [ns]
-20
-25
-30
-35
-40
-45
-50
-55

(b)

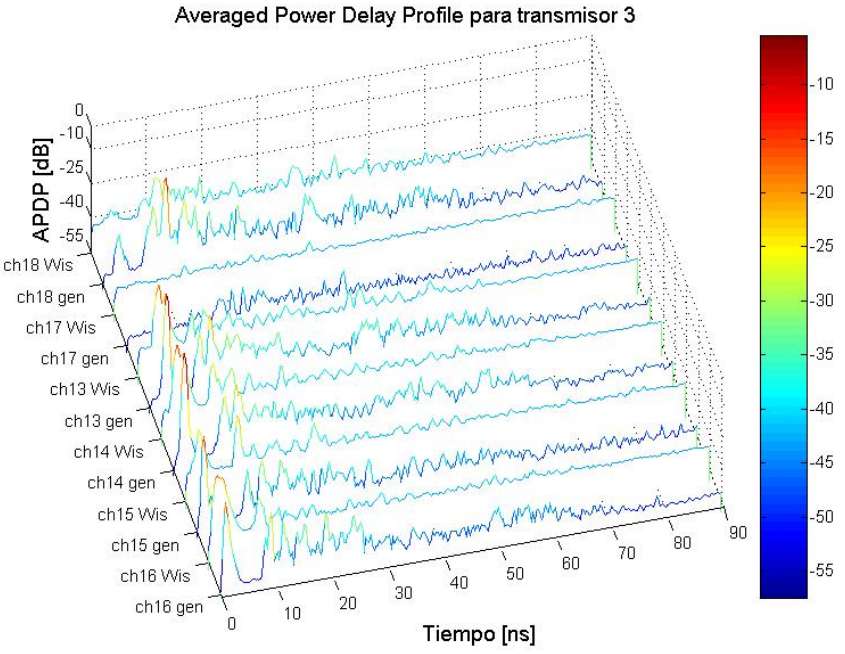
Averaged Power Delay Profile para transmisor 3
APDP [dB]
0
-10
-25
-40
-55
ch18 Wis
ch18 gen
ch17 Wis
ch17 gen
ch13 Wis
ch13 gen
ch14 Wis
ch14 gen
ch15 Wis
ch15 gen
ch16 Wis
ch16 gen
0
10
20
30
40
50
60
70
80
90
Tiempo [ns]
-10
-15
-20
-25
-30
-35
-40
-45
-50
-55

(c)

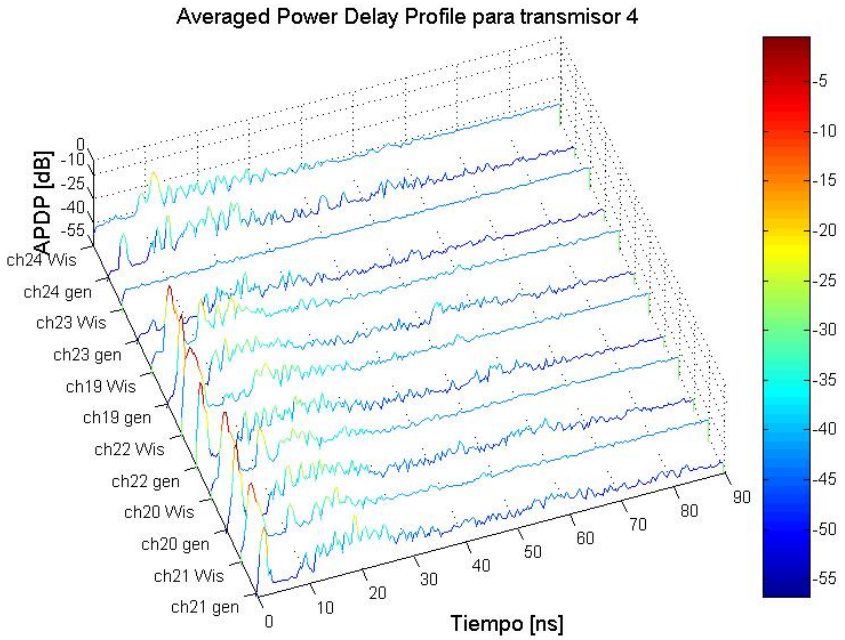

(d)

Fig. 19 APDPs correspondientes a las 4 posiciones del transmisor: arriba de la cabeza (a), lado izquierdo (b), parte trasera (c) y lado derecho (d) para un dispositivo móvil

Mean delay of strongest echo, mean delay of first echo, mean excess delay y delay spread

La Fig. 19 muestra el *Mean Delay of Strongest Echo* (MDSE) o retardo medio de la contribución más fuerte, para ambas antenas y distancias del enlace. Los enlaces están separados según si existe visión directa (LOS) o no (NLOS). Lógicamente, el MDSE es menor para canales LOS y menos variante con la distancia que para los NLOS. Como puede observarse, el incremento lineal para LOS y NLOS es similar para los dos tipos de antenas.

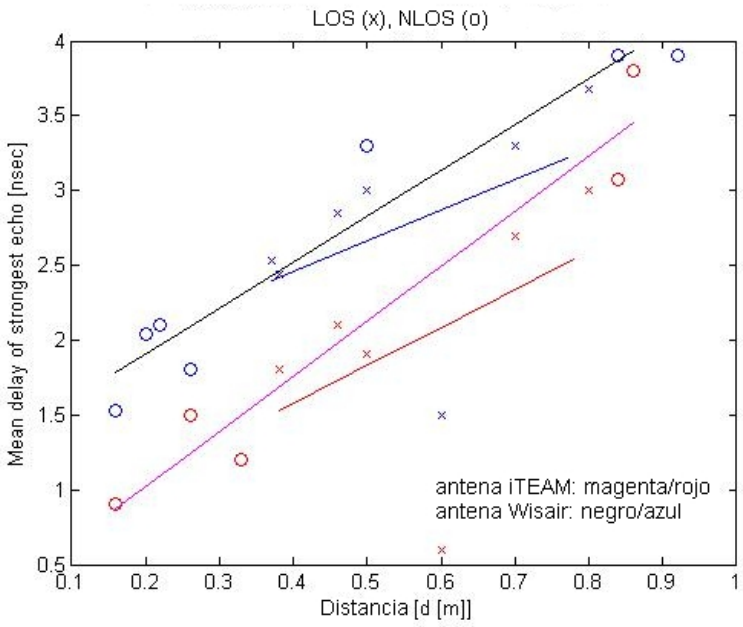

Fig. 20 Mean Delay of Strongest Echo para ambos tipos de antenas, para canales con y sin visión directa

Para caracterizar el APDP, se calcula el *delay spread*, que es la duración de la dispersión:

$$\tau_{rms} = \sqrt{\frac{\sum_{i=1}^{N} (\tau_i - \tau_A)^2 P(\tau_i)}{\sum_{i=1}^{N} P(\tau_i)}} \tag{6}$$

Con τ_i, tiempo de llegada de una contribución, $P(\tau_i)$, potencia asociada a esa contribución y τ_A, mean delay:

$$\tau_A = \frac{\sum_{i=1}^{N} \tau_i P(\tau_i)}{\sum_{i=1}^{N} P(\tau_i)} \tag{7}$$

El valor medio de τ_{rms} clasificados según LOS o NLOS se muestra en la Tabla 6. Como se esperaba, el *delay spread* en los casos NLOS es mayor que para LOS.

		Delay spread
iTEAM	LOS	0.2484
	NLOS	1.0198
Wisair	LOS	0.4932
	NLOS	1.1096

Tabla 6 Delay spread para los canales LOS y NLOS para las antenas del iTEAM y Wisair

La Fig. 20 (arriba) muestra en rojo el MDSE y en magenta el MDFE (*Mean Delay of First Echo*) o retardo medio de la primera contribución, para todos los canales de la antena del iTEAM. Para los canales en los que coinciden MDSE con MDFE sólo el este último es representado. La línea negra representa la llegada de la primera contribución no directa (proveniente de la reflexión en el suelo o techo). Puede observarse que para todos los canales LOS, las contribuciones principales llegan antes que las no directas, ya que el MDSE es menor del retardo del camino no directo.

En Fig. 20 (abajo) se representa el porcentaje de potencia recibida. La línea negra marca el 10% de la potencia recibida y los canales que recolectan menos de esta potencia están representados en rojo. Estos canales coinciden con aquellos en los la contribución directa llega después de las reflexiones, por lo puede verse (Fig. 20 (arriba)) que el MDSE es mayor que el retardo de la contribución no directa. Para el resto de canales, un receptor que recoge señal hasta la primera contribución no directa, asegura un porcentaje de potencia útil de más del 20%. Los canales LOS presentan mejor relación de potencia media, 42%, que los NLOS con 10.5%.

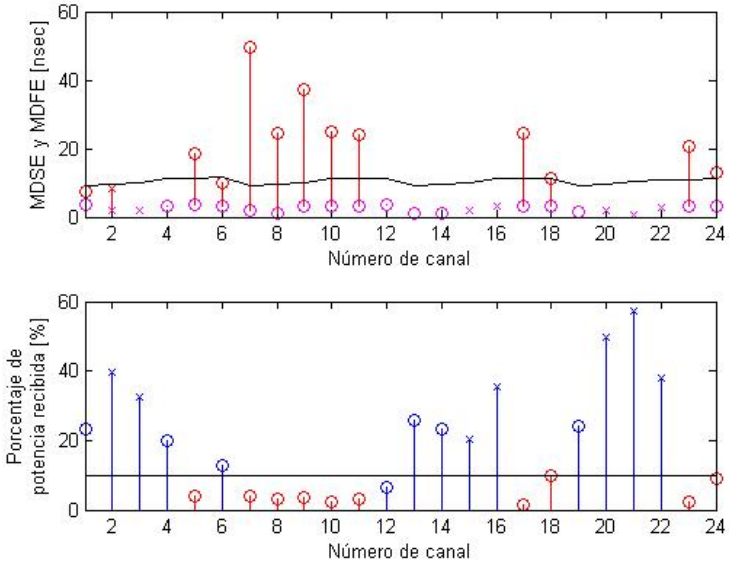

Fig. 21 MDSE y MDFE obtenidos en la antenna del iTEAM para LOS y NLOS canales (arriba) y porcentaje de potencia recibida

VI.1.3. Caso 2: Dispositivo implantable

Path loss

En la Fig. 21 se muestra el *path loss* calculado para los 48 canales del dispositivo implantable (en azul) y, de modo comparativo, los resultados obtenidos para el dispositivo móvil (en rojo) frente a la distancia del enlace en unidades logarítmicas y normalizada a la mínima distancia. Puede observarse que para el implantable, el *path loss* es mayor, aunque la variabilidad del canal es de sólo 10 dB frente a los 25 dB del dispositivo móvil. El exponente de *path loss* es de 0.566 para el implantable.

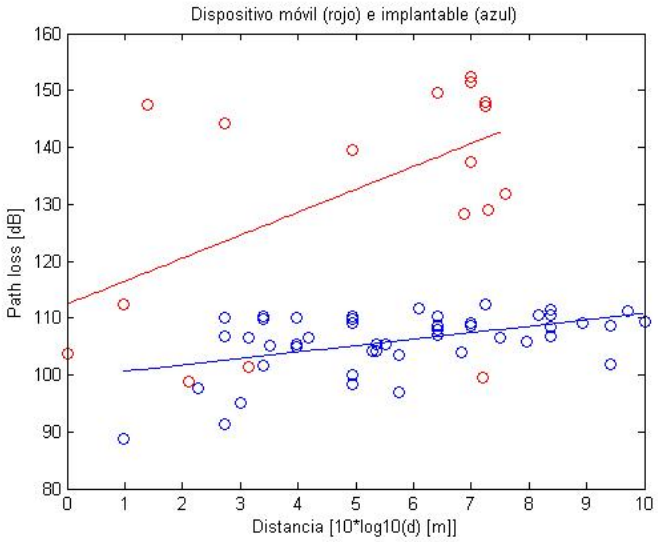

Fig. 22 Path loss para un dispositivo móvil (rojo) y uno implantable (azul) para diversos canales y sus respectivas aproximaciones lineales

Averaged Power Delay Profile (APDP)

En la Fig. 1 pueden observarse los APDP para las diferentes posiciones del implante. En el eje *y* se observan las posiciones agrupadas en dos grupos: las 8 posiciones delanteras del implante y las 4 traseras. Dentro de cada grupo, los canales están ordenados de menor a mayor distancia entre el transmisor y el receptor.

En general, puede observarse una primera contribución que llega antes de los 6 ns y un silencio hasta los 8 ns aproximadamente, que es cuando llega la segunda contribución correspondiente a las reflexiones en el entorno, principalmente suelo y techo.

Para el transmisor 1, puede observarse (Fig. 22 (a)) que la segunda contribución es algo mayor que la primera. Esto es lógico ya que este transmisor está colocado en la parte superior de la cabeza y la reflexión en el techo es bastante importante mientras que el cuerpo obstaculiza y atenúa la señal directa. De hecho, puede observarse que en las posiciones delanteras 7 y 8 ambas contribuciones son muy débiles, ya que tanto la señal directa como la reflexión del techo llegan muy atenuadas a las posiciones de la rodilla y el tobillo.

En la Fig. 22 (b), está representado el APDP para el transmisor 2, situado en la parte izquierda de la cabeza, justo la parte contraria a la posición de los receptores, que se sitúan a lo largo de la parte derecha del cuerpo. Por ello puede observarse que, especialmente a partir de la posición delantera 3, las contribuciones llegan muy debilitadas, ya que prácticamente todos los caminos son sin visión directa y además se ven atenuados por el cuerpo.

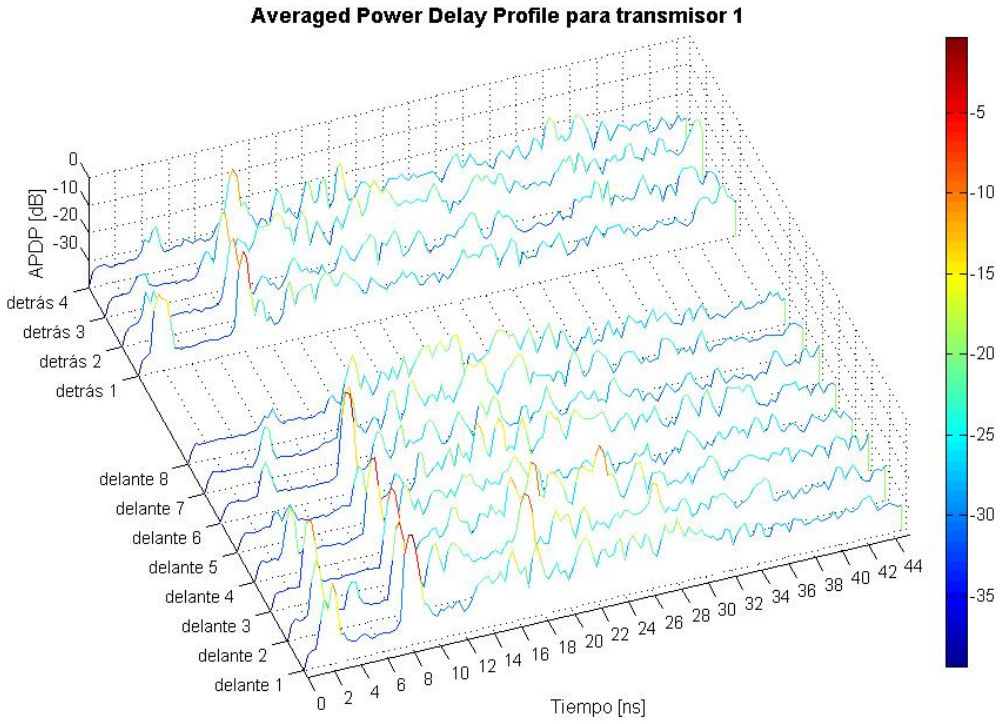

(a)

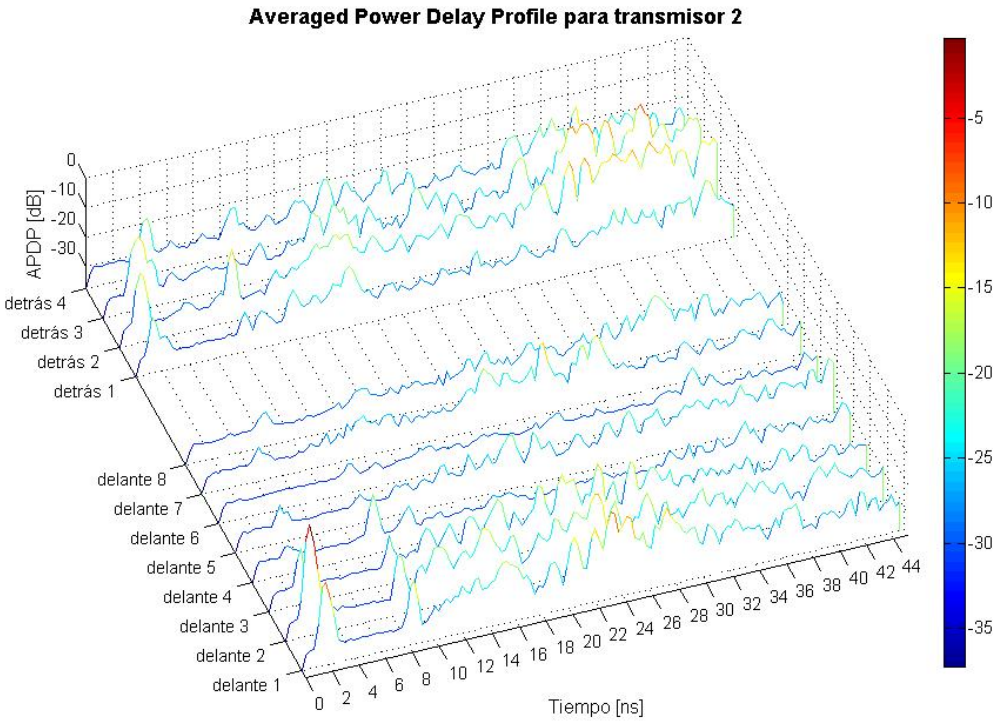
Averaged Power Delay Profile para transmisor 2
APDP [dB]
0
-10
-20
-30
detrás 4
detrás 3
detrás 2
detrás 1
delante 8
delante 7
delante 6
delante 5
delante 4
delante 3
delante 2
delante 1
0 2 4 6 8 10 12 14 16 18 20 22 24 26 28 30 32 34 36 38 40 42 44
Tiempo [ns]
-5
-10
-15
-20
-25
-30
-35

(b)

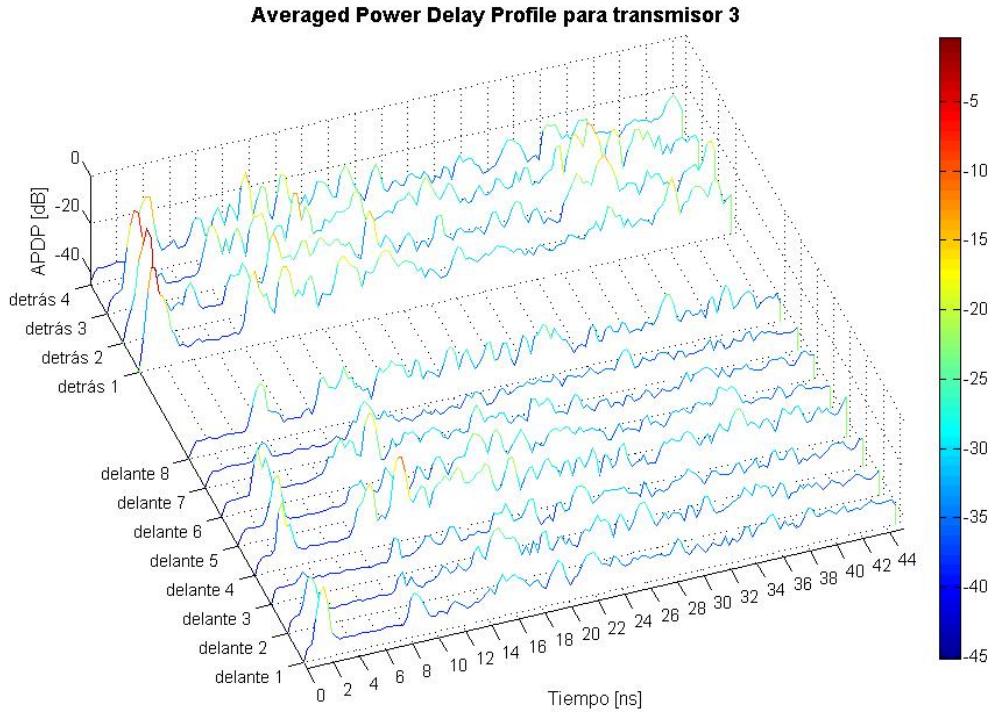
Averaged Power Delay Profile para transmisor 3
APDP [dB]
0
-20
-40
detrás 4
detrás 3
detrás 2
detrás 1
delante 8
delante 7
delante 6
delante 5
delante 4
delante 3
delante 2
delante 1
0 2 4 6 8 10 12 14 16 18 20 22 24 26 28 30 32 34 36 38 40 42 44
Tiempo [ns]
-5
-10
-15
-20
-25
-30
-35
-40
-45

(c)

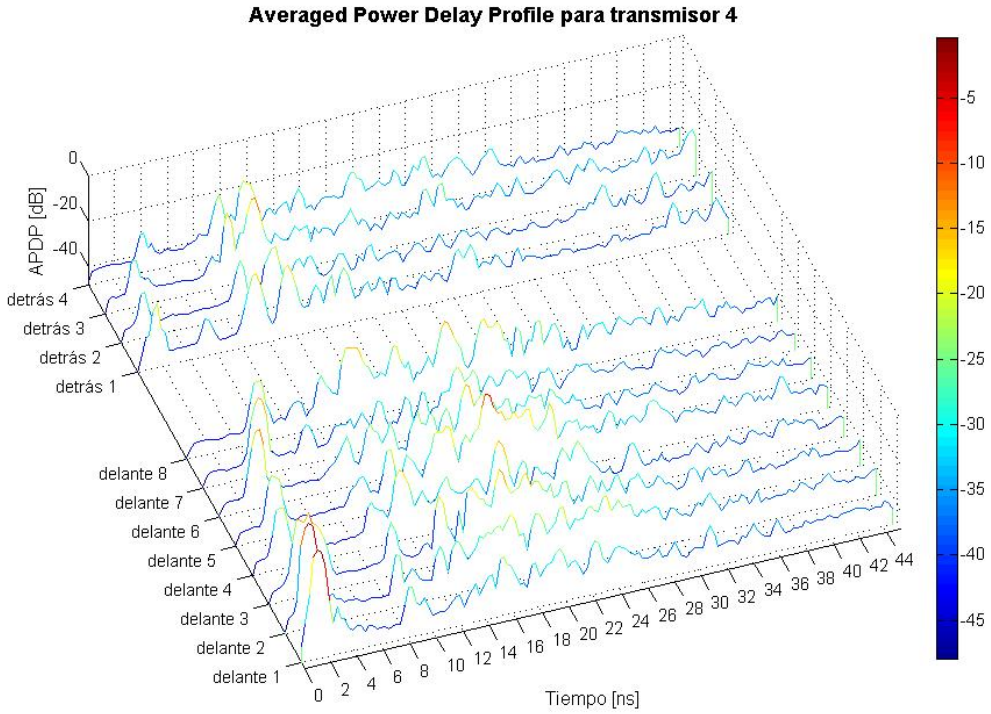

(d)

Fig. 23 APDPs correspondientes a las 4 posiciones del transmisor: arriba de la cabeza (a), lado izquierdo (b), parte trasera (c) y lado derecho (d) para un dispositivo implantable

Con el transmisor situado en la parte trasera de la cabeza, Fig. 22 (c), como era de esperar, los receptores situados en la espalda son los que mejor señal reciben.

Y finalmente para la posición 4 (Fig. 22 (d)), podemos comprobar que, dado que transmisor y receptor están situados en el mismo lado del cuerpo, se sufre menor atenuación y se obtiene una clara primera contribución, aunque los implantes de la parte trasera reciben una señal más débil.

Mean delay of strongest echo, mean delay of first echo, mean excess delay y delay spread

Se muestra en la Fig. 23 el MDSE (rojo) y el MDFE (magenta) para las cuatro posiciones del transmisor. La línea negra representa la llegada de la primera contribución no directa (proveniente generalmente del suelo o el techo). Si comparamos nuevamente estos resultados con los de la Fig. 24, donde puede verse el porcentaje de potencia recibida, se observa que los canales cuyo MDSE es mayor que el tiempo de llegada de la primera contribución no directa (que pueden verse por encima de la línea negra en la Fig. 23 y están representados en rojo en la Fig. 24), suelen recolectar menos del 10% de la potencia enviada. Por ejemplo, en los canales 5 al 8 del transmisor 2 se tiene una contribución principal que llega 30-40 ns después que la primera no directa, y se observa una APDP muy plana.

Los transmisores 1, 3 y 4 muestran un menor número de canales con esta característica, por lo que se puede decir que estos canales sufren una menor dispersión de la señal.

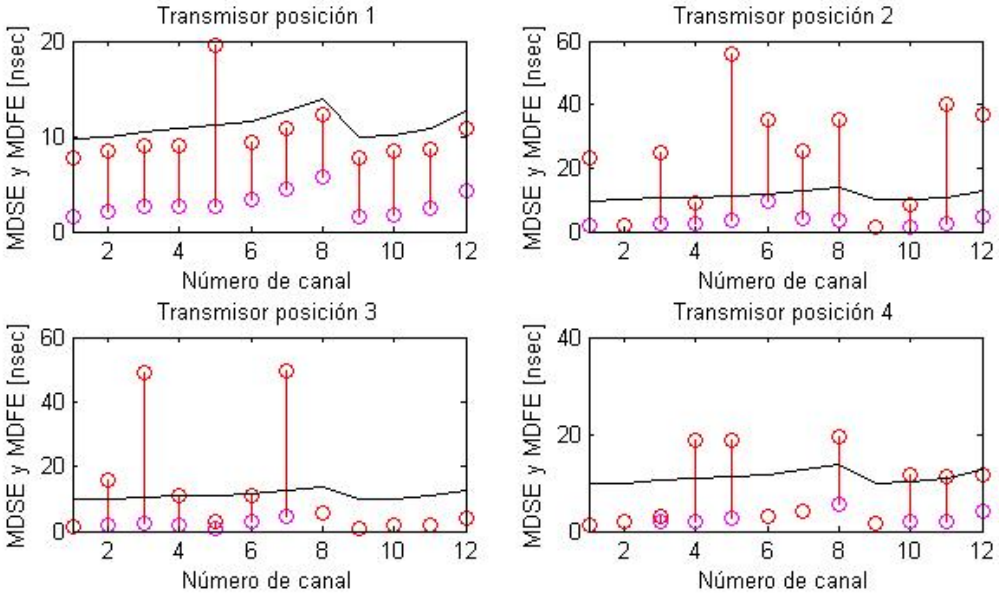

Fig. 24 MDSE (círculo rojo) y MDFE (círculo magenta) para las 4 posiciones del transmisor

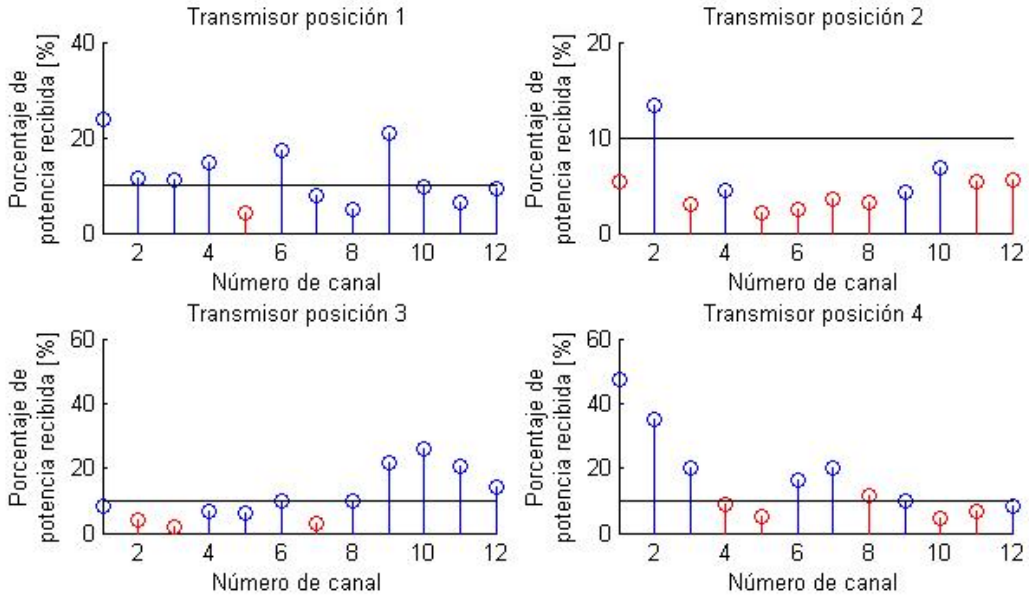

Fig. 25 Porcentaje de energía recibida para las 4 posiciones del transmisor. Rojo indica que en ese canal, el eco más fuerte llega después que la primera contribución no directa.

En cuanto al *delay spread* (τ_{rms}) y al *mean excess delay* (τ_m), se representan comparativamente en la Fig. 25. La línea negra discontinua se corresponde con la recta $\tau_m = \tau_{rms}$. La recta que mejor ajusta los resultados se representa en azul y es:

$$\tau_m = 0.85\ \tau_{rms} + 2.0372 \tag{8}$$

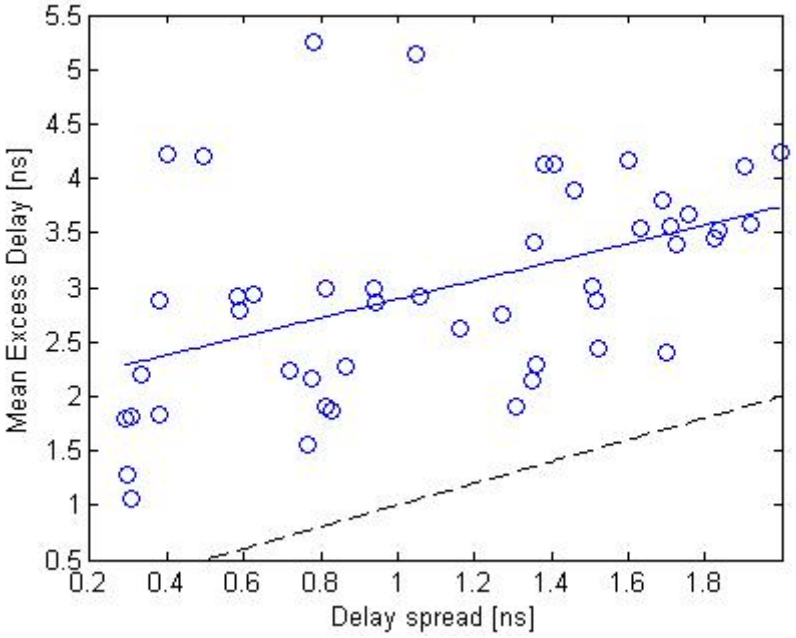

Fig. 26 Mean excess delay vs. delay spread

Como puede observarse, para todos los canales medidos se tiene que $\frac{\tau_m}{\tau_{rms}} > 1$. Esto significa que en general la potencia no está muy concentrada y que la energía llega distribuida en el tiempo.

VII. DISCUSIÓN Y CONCLUSIONES

En este trabajo se ha hecho un estudio exhaustivo de las diferentes técnicas de transmisión inalámbrica para corto alcance y se ha concluido que UWB es la única cumple las necesidades de baja potencia y alta capacidad de transmisión, que eran requisito para el sistema que se planteaba.

Por otro lado, se ha hecho un estudio del mercado en cuanto a dispositivos con tecnología UWB y se ha adquirido un kit de evaluación con el que poder probar y testear su funcionamiento.

Según las medidas realizadas utilizando el kit comercial adquirido, la transmisión con la tecnología UWB no alcanza las máximas velocidades especificadas, pero alcanza unas tasas de transmisión mucho mayores que el resto de tecnologías estudiadas. Estas tasas son suficientes para cumplir los requisitos de *throughput* (10-40 Mbps) del sistema que se pretende diseñar.

Se ha evaluado la calidad de la detección de *spikes* en señales neuronales, midiendo la BER y la AUC de la señal transmitida a través de un enlace UWB. En este caso la información que de verdad interesa conocer es cuántos de los *spikes* que transportaba la señal se han perdido en la transmisión. Por ello, el cálculo del área bajo la curva de las curvas ROC para detectores de *spikes* es una aproximación más real a la degradación de la señal por la transmisión, ya que depende de la actividad del canal transmitido, mientras que la BER caracteriza el sistema de transmisión.

Sin embargo, ya que BER y AUC nos dan una idea muy similar de cómo ha afectado la transmisión a la señal, podríamos usar la BER como aproximación, ya que el cálculo de la BER es mucho más rápido que el de la AUC.

Según los resultados y teniendo en cuenta las necesidades del sistema, para una tasa de transmisión de 11 Mbps nos bastaría con utilizar una configuración para 53.3 Mbps (la mínima en el estándar WiMedia), para obtener una recepción óptima. Si la tasa fuera de 36 Mbps, podríamos utilizar la configuración de 106.7 Mbps para transmitir con baja BER. Aunque si el sistema lo permite, y pensando en escenarios más adversos, sería mejor elegir una velocidad mayor, por ejemplo, la siguiente a 160 Mbps y así aseguraríamos una buena recepción.

Con el fin de modelar el canal UWB en el entorno corporal, se han realizado medidas de canal para el rango de frecuencias de UWB, tanto para el caso en que tenemos un enlace implante cerebral a implante corporal, como para el caso implante cerebral a dispositivo móvil. Las medidas de canal muestran que el cuerpo ofrece una gran influencia, así como el entorno.

Para el caso del dispositivo móvil, ambas antenas, tanto las antenas manufacturadas por el iTEAM como las antenas comerciales de Wisair, han dado un resultado similar, siendo coherente en todo momento. Las diferencias observadas (por ejemplo, la diferencia constante en el *path loss* o en el MDSE) son debidas a una diferente adaptación de las dos antenas, lo que lleva a la antena de Wisair a tener más pérdidas que la del iTEAM.

El *path loss* medio y su variabilidad son mayores para los canales con receptor dispositivo móvil que para el caso del dispositivo implantado, lo cual quiere decir que la atenuación de la cabeza es más significativa para el dispositivo móvil.

En general podemos decir, tal como se aprecia en los APDPs calculados, que la energía no está muy concentrada, sino que más bien llega muy distribuida en el tiempo. Con respecto al transmisor, cuando está situado a la parte derecha de la cabeza, en el mismo lado en el que se sitúan los receptores, se obtienen los mejores resultados. Si los implantes se encuentran en la espalda, el transmisor debería situarse en la parte trasera de la cabeza. También se ha comprobado que cuando el transmisor está situado en la parte alta de la cabeza, la reflexión del techo cobra mucha importancia, con lo que sería útil un receptor capaz de utilizar la potencia proveniente de dicha reflexión. También se concluye de los resultados que la elección de la antena y la adaptación de la misma son muy importantes, ya que la antena del iTEAM recibía una mayor potencia.

El estudio de MDSE, MDFE muestra que la primera contribución no es siempre la más importante y, por lo tanto, la recolección de energía debería hacerse al menos hasta la llegada del segundo eco.

Tras las medidas realizadas se deduce que la transmisión a las velocidades demandadas sería viable. La caracterización del canal nos da una idea de la transmisión de las señales sobre un paciente con el dispositivo receptor moviéndose a lo largo de distintas posiciones. En este caso, el

entorno corporal es un canal muy variable donde la posición del transmisor con respecto al receptor y la capacidad de este de recolectar la señal transmitida son decisivas.

AGRADECIMIENTOS

Quiero agradecer al proyecto Sinaptic, financiado por Telefónica de España, que se llevó a cabo durante el pasado año 2006 y que ha dado lugar a este trabajo.

Del mismo modo, quiero agradecer a Cristina y Narcís el haberme dirigido en la realización de esta tesina. Gracias también a Lara por su colaboración y a todos ellos por todo lo que he aprendido en este tiempo.

BIBLIOGRAFÍA

[1] C.R. Anderson et al., *An Introducction to Ultra Wideband Communication Systems*. Prentice Hall PTR, ISBN 0131481037

[2] F. Nekoogar, *Ultra-WideBand Communications. Fundamentals and applications.* Prentice Hall PTR, ISBN 0131463268

[3] X. Shen, M. Guizani, R.C. Qiu and T. Le-Ngoc, *Ultra-Wideband Wireless Communications and Networks.* John Wiley & Sons, ISBN 9780470011447

REFERENCIAS

[4] S.H. Choi and M. Lee, *Brain Computer Interface using EEG Sensors Based on an fMRI Experiment*. International Joint Conference on Neural Networks, IJCNN '06, 16-21 July 2006, pp 4656 – 4663

[5] C.D. Tesche, *Detecting activity from deep brain areas with magnetoencephalographic arrays*. Proceedings of the 20th Annual International Conference of the IEEE Engineering in Medicine and Biology Society, 29 Oct.-1 Nov. 1998, vol. 4, pp 2201 - 2204

[6] K.C. Cheung, K. Djupsund, Y. Dan and L.P. Lee, *Implantable Multichannel Electrode Array Based on SOI Technology*. Journal of Microelectromechanical Systems, Apr. 2003, vol. 12, number 2

[7] J.B. Christen and A.G. Loeb, *Design, Fabrication and Testing of a Hybrid CMOS/PDMS Microsystem for Cell Culture and Incubation*, IEEE Transactions on Biomedical Circuits and Systems, March 2007, vol. 1, number 1

[8] E. Kyriacou, S. Pavlopoulos, D. Koutsouris, A.S. Andreou, C. Pattichis and C. Schizas, *Multipurpose health care telemedicine system*, Proceedings of the 23rd Annual International Conference of the IEEE Engineering in Medicine and Biology Society, Oct. 2001, vol. 4, pp. 3544 – 3547

[9] C. Kugean, S.M. Krishnan, O. Chutatape, S. Swaminathan, N. Srinivasan and P. Wang, *Design of a mobile telemedicine system with wireless LAN*. Asia-Pacific Conference on Circuits and Systems, APCCAS '02, Oct. 2002, vol. 1, pp 313 - 316

[10] I. Obeid, *A wireless multichannel neural recording platform for real-time brain machine interfaces*. Ph.D. dissertation, Department of Biomedical Engineering Duke University, 2004

[11] G.R. Perelman Y, *Analog frontend for multichannel neuronal recording system with spike and LFP separation*. J. Neurosci. Methods., 2006

[12] NeuroNexus Technologies, http://neuronexustech.com (accesible a 10/08/07)

[13] Multi Channel Systems, http://www.multichannelsystems.com (accesible a 10/08/07)

[14] A.F. Molisch, *Ultrawideband Propagation Channels-Theory, Measurement and Modeling*. IEEE Transactions on Vehicular Technology, vol. 54, no. 5, Sept. 2005

[15] A. Muqaibel, A. Safaai-Jazi, A. Attiya, B. Woerner and S. Riad, *Path-loss and Time Dispersion Parameters for Indoor UWB Propagation*. IEEE Transactions on Wireless Communications, vol. 5, no. 3, March 2006

[16] A. Alomainy and H.Hao, *Radio Channel Models for UWB Body-Centric Networks with compact planar antenna*. IEEE Antennas and Propagation Society International Symposium, July 2006, pp 2173-2176

[17] A. Alomainy, Y. Hao, C. Parini and P. Hall, *Comparison between two different antennas for UWB on-body propagation measurements.* Antennas and Wireless Propagation Letters, 2005

[18] T.B. Welch, R.L. Musselman, B.A. Emessiene, P.D. Gift, D.K. Choudhury, D.N. Cassadine and S.M. Yano, *The effects of the human body on UWB signal propagation in an indoor environment.* IEEE Journal on Selected Areas in Communications, vol. 20, no. 9, Dec. 2002

[19] T. Zasowski, F. Althaus, M. Stäger, A. Wittneben and G. Tröster, *UWB for noninvasive wireless body area networks: Channel measurements and results*. IEEE Conference on Ultra Wideband Systems and Technologies, UWBST 2003, Nov 2003

[20] S.Warren, J. Lebak, J. Yao, J. Creekmore, and A. M. E. Jovanov, *Interoperability and security in wireless body area network infrastructures*. 27th Annual International Conference of the Engineering in Medicine and Biology Society, Sept 2005

[21] S.N. Yu and J.C. Cheng, *A wireless physiological signal monitoring system with integrated bluetooth and wifi technologies*. 27th Annual International Conference of the Engineering in Medicine and Biology Society, Sept. 2005

[22] C. Lopez-Casado, J. Tejero-Calado, A. Bernal-Martin, M. Lopez-Gomez, M. Romero-Romero, G. Quesada, J. Lorca, and E. Garcia, *Network architecture for global biomedical monitoring service*. 27th Annual International Conference of the Engineering in Medicine and Biology Society, Sept. 2005.

[23] D. Salamon, M. Grigioni, M. Gianni, M. Liberti, S. De luca, A. Bei and G. D'Inzeo, *Indoor Telemedicina in Hospital: a PDA-based Flexible Solution for Wireless Monitoring nad Database Integration*. Proceedings of the IEEE Engineering in Medicine and Biology 27th Annual Conference, Sept. 2005, pp 386 - 389

[24] J. Ryckaert, C. Desset, A. Fort, M. Badaroglu, V. De Heyn, P. Wambacq, G. Van der Plas, S. Donnay, B. Van Poucke and B. Gyselinckx, *Ultra-wide-band transmitter for low-power wireless body area networks: design and evaluation.* IEEE Transactions on Circuits and Systems I: Regular Papers, Vol 52, Issue 12, Dec 2005, pp 2515 – 2525

[25] Bluetooth SIG, *Bluetooth specifications*, www.bluetooth.org (accesible a 10/08/07)

[26] ZigBee Alliance, *ZigBee Specifications*, www.zigbee.org (accesible a 10/08/07)

[27] C.C. Wang, J.M. Huang, L.H. Lee, S.H. Wang and C.P. Li, *A Low-Power 2.45 GHz ZigBee Transceiver for Wearable Personal Medical Devices in WPAN.* International Conference on Consumer Electronics, 2007. ICCE 2007. Digest of Technical Papers, 10-14 Jan 2007, pp 1-2

[28] Z. Zhao and L. Cui, *Easimed: A remote health care solution*. 27th Annual International Conference of the Engineering in Medicine and Biology Society, Sept. 2005

[29] FCC, www.fcc.gov (accesible a 10/08/07)

[30] WiMedia Alliance, www.wimedia.org (accessible a 10/08/07)

ANEXOS

A continuación se encuentran anexas la lista de publicaciones a las que ha dado lugar la investigación de la tesina, así cómo las pruebas de asistencia o aceptación a los congresos. Se adjuntan también los artículos completos, tal y como aparecieron (o como aparecerán) en el congreso.

Publicaciones y congresos

C. Tarín, L. Traver, J.F. Santamaria, P. Martí and N. Cardona, *Bluetooth-3G wireless transmission system for neural signal telemetry*. Proceedings of the Wireless Telecommunications Symposium, WTS 2007 (1-4244-0697-8/07/.00), California, 2007.

C. Tarín , P. Martí ,L. Traver, N. Cardona, J.A. Díaz and E. Antonino, *UWB Channel Measurements for hand-portable devices: a comparative study*. Proceedings of the IEEE International Symposium on Personal, Indoor and Mobile Radio Communications (1-4244-1144-0/07/$25.00), Athens, Sept 2007

C. Tarín, L. Traver, P. Martí, N. Cardona, J.A. Díaz and M. Cabedo, *UWB Channel measurements for measures for hand-portable and wearable devices*. Proceedings of the IEEE International Conference on Wireless and Mobile Computing, Networking and Communications (0-7695-2889-9/07 $25.00), New York, Oct 2007

Aceptados pendientes de publicación:

Capítulos en libros

C. Tarín, L. Traver, P. Martí and N. Cardona. Chapter: *Wireless communication systems from the perspective of implantable sensor networks for neural signal monitoring*. Book: Wireless Technology: Applications, Management and Security based on the top research presented at WTS 2007.

Artículos en revistas

L. Tracver, C. Tarín, P. Martí and N. Cardona, *Adaptive-threshold neural spike detection by noise-envelope tracking (ELL-2007-1631)* Electronic Letters, 2007.

Mail de aceptación del capítulo del libro "Wireless Technology: Applications, Management and Security based on the top research presented at WTS 2007"

----- Mensaje reenviado de Aaron French <amf165@msstate.edu> -----
Fecha: Sat, 30 Jun 2007 19:10:27 -0500
De: Aaron French <amf165@msstate.edu>
Responder-A: Aaron French <amf165@msstate.edu>
Asunto: WTS Program Committee
Para: critasa@iteam.upv.es

I am contacting you on the behalf of:
Dr. Steve Powell, WTS General Chair [srpowell@csupomona.edu]
Dr. J.P. Shim, WTS Program Chair [JShim@cobilan.msstate.edu]

June 30, 2007

Dear Cristina TarÃn,

Congratulations! The WTS Program Committee has selected your paper presented at WTS 2007 for inclusion in a forthcoming book entitled Wireless
Technology: Applications, Management, and Security to be published by Springer. Copyright restrictions on papers published in the book require that they be expanded/revised so that they differ substantially from the papers published in the 2007 WTS Proceedings.

Please let us know by July 7 if you would like your paper published in this
book representing the best papers presented at WTS 2007. If you would like
your paper published in the book, it is necessary that you send me an expanded/revised version of the paper by August 1 so that we can meet Springer's deadline for the manuscript (Instructions for Authors will be announced shortly).

Thank you for participating in WTS 2007. Your WTS 2007 paper will contribute a great deal to our book.

We look forward to hearing from you.

Sincerely,

Dr. Steve Powell Dr. J.
P. Shim
WTS General Chair WTS Program
Chair

----- Fin del mensaje reenviado -----

Mail de aceptación del artículo para Electronic Letters

-----Mensaje original-----
De: eletters@theiet.org [mailto:eletters@theiet.org]
Enviado el: viernes, 02 de noviembre de 2007 10:45
Para: latrase@iteam.upv.es
Asunto: Message from Electronics Letters

Dear Ms. Traver

I am pleased to inform you that your paper ELL-2007-1631 'Adaptive-threshold neural spike detection by noise-envelope tracking' has been accepted for publication in Electronics Letters and will appear in a forthcoming issue, a complimentary copy of which will be sent to you. Reprints of a Letter can also be supplied; a reprint request form and details of reprint charges will be sent to you shortly before publication.

Also, we cannot publish your paper without a signed copyright form which has been included as an attachment and is also available at http://www.iee.org/Publish/Support/Auth/Authel.cfm#copyright

Please send a copy back to the editorial office, preferably by fax at +44 (0)1438 767317.

Yours sincerely,

Dr Helen Dyball

Electronics Letters

Bluetooth-3G wireless transmission system for neural signals telemetry

Cristina Tarín Sauer, Lara Traver Sebastià, Juan Felipe Santamaría Gómez, Paula Martí Rocafull and Narcís Cardona Marcet
ITEAM
Tech. University of Valencia
E-46022 Valencia, Spain

Abstract

In this contribution a wireless transmission system for neural signals is developed. This system includes data compression algorithms at the information source, namely neural signals recorded by micro-electrode arrays. The signals are transmitted over Bluetooth to a mobile device that, without any processing or storing, retransmits it over 3G to a remote server where signal post-processing and analysis is performed. The overall transmission rate of the system is limited by the Bluetooth link between the information source and the mobile phone. Data compression allows the transmission of up to 3 neural signals in real-time, while the limiting data rate is smaller than that required for the real-time transmission of one single signal.

1. Introduction

In recent years, a number of promising clinical prototypes of implantable and wearable monitoring devices have started to emerge [1]. Although a number of problems as long-term stability and biocompatibility remain, the potential medical value is enormous. Many applications exist in the field of bio-telemetry: blood glucose level monitorization, identification in cardiological life threatening episodes, etc. Our interest focusses in neurological monitoring [2]. Telemetry systems for neuronal signals are nowadays under investigation and we are particularly interested in Bluetooth and 3G as a possible wireless transmission method for such systems.

The design of a telemetry application includes the specification of the communication system parameters such as data transmission capacity, synchrony, delay, etc. In other words, the application defines the set of requirements to be met by the communication system. Meeting the required specifications is eventually accomplished by correct definition of the communication protocol layers which use a physical channel to implement the data communication.

We have developed a wireless transmission system for neural signals over Bluetooth and 3G. The neural signals are recorded my micro-electrode arrays and then, in real-time transmitted over a Bluetooth link to a mobile phone. This mobile device immediately, without intermediate storage, re-transmits the signals over 3G to a remote server where data processing and analysis is performed.

First, in section 2, there is a description of the characteristics of the signals captured by the neuronal multi-electrode sensors and the bandwidth requirements imposed by them including also a compression algorithm. Section 3 describes and analyzes the developed wireless transmission system over Bluetooth and 3G. Measurement results and complete discussion are provided in section 4. Finally, in section 5 the conclusions drawn from the developed work are shown.

2. Neural signal processing

2.1. Neural signals

Signals from extracellular cortical electrodes contain action potential waveforms with amplitudes ranging from tens to hundreds of microvolts peak to peak; pulse widths are typically 1 - 1.5 ms. The noise floor, which includes biological noise from far field neurons and electrical noise from the amplifier circuit, is around 20 μVrms; signal to noise ratios therefore range from 0 to 12 dB, although ratios as high as 20 dB are occasionally encountered [3]. Published figures for the signal frequency content vary, ranging from 100 to 400Hz for the low end range to 3k to 10 kHz for the high end range. Published sampling rates also vary, ranging from 15 kHz up to 50 kHz. In general, higher sampling rates produce higher fidelity signals but also produce more data, requiring faster and higher power systems to process them. Furthermore, in a wireless system with limited bandwidth, increasing the sampling rate will increase the data rate. Analog to digital converter (ADC) resolution should be

10 - 12 bits to provide 60 - 72 dB of dynamic range. Figure 1 displays the data rate required for the transmission of a neural signal as a function of the sampling frequency and the selected number of quantization bits per sample.

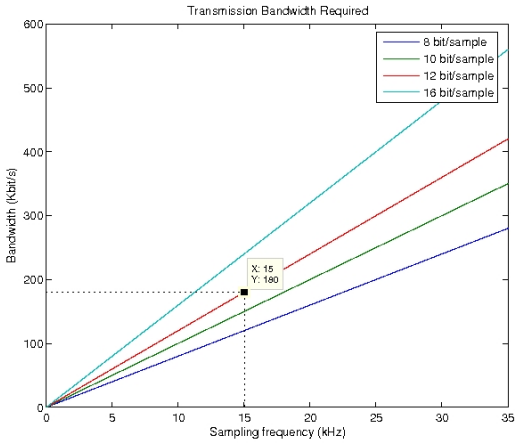

Figure 1: Transmission bandwidth required depending on the sampling frequency and precision.

For the experiments presented in this paper we use recordings of in-vitro neural activity kindly provided by Multichannel Systems. A 64-electrode array was used and signals where sampled at 15 Khz. Figure 2 shows the Multi Channel Systems Multi-Electrode Array.

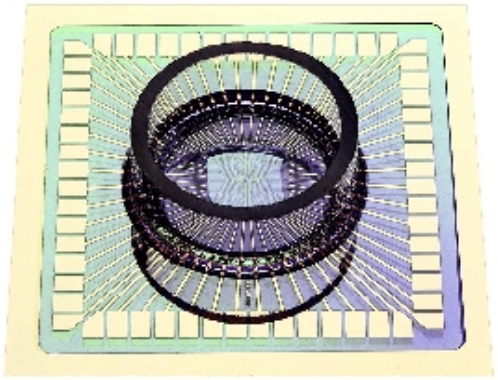

Figure 2: 64 channels Multi-Electrode Array (MEA) from Multi Channel Systems (*www.multichannelsystems.com*) widely used in neuronal signal recordings.

2.2. Neural signal compression

As described above, neural signals contain trains of action potentials or spikes that form particular spiking patterns. During the intervals of the signal without spikes, the content of the signal is exclusively noise. It is, therefore, possible to compress neural signals by coding the impulse trains leaving the noise-only parts away. For doing this, it is necessary to: first detect the occurrence of the spikes, and then code the time, the channel (in the case of a multichannel recording system) and the spike waveform. In this way, it is feasible to compress and multiplex an arbitrary number of channels into one single stream of data.

For this work, we have considered the case where the recording system has a number N of recording electrodes. The sampling frequency is 15 Khz and the sampling precision is 12 bits. The system is then producing a $12 \times 15 \times N = 180 \times N$ kbps data stream.

We have implemented a compression algorithm that works in a frame-based manner. Each processing frame lasts 50 ms, i.e., 750 samples. In each frame-based step the algorithm performs a spike detection for each of the channels and, when a spike is detected, the time and channel of the spike are coded at the output. Figure 3 shows the coding structure.

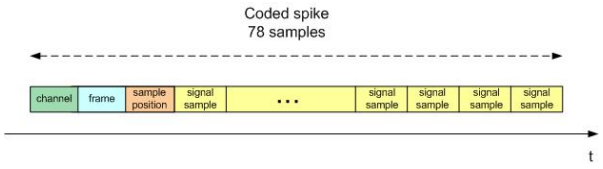

Figure 3: Coded spike.

Neural signals coded in this way can be later decoded and spike trains can be reconstructed by placing each spike waveform in the corresponding channel and time.

Detection is done by a Nonlinear-Energy-Operator-based detector, which preprocesses input signal $x[n]$ by applying the energy operator

$$\Psi(x[n]) = x^2[n] - x[n-1] \cdot x[n+1]$$

.

Such preprocessing eases the detection process because it amplifies the signal energy concentrations.

After preprocessing, spikes are detected by comparing the signal amplitude with an adaptive threshold. Adaptation is done by performing automatic noise-level tracking and setting the threshold to certain level which is relative to the estimated noise level.

The process for noise-level estimation is as follows. For each processing frame:

- Maximum absolute value of the signal amplitude is calculated ($|s_{max}[n]|$)
- The maximum is compared with the noise-level estimation in the previous frame ($|n[n-1]|$)
- If the maximum is bigger than 5 times the noise level of the previous frame,

$$|s_{max}[n]| > 5 \cdot |n[n-1]|$$

it is assumed that there is a spike present in the frame and, therefore, the noise level estimate is not updated.

- Otherwise,
  - if the maximum is bigger than the noise level estimate

$$|s_{max}[n]| > |n[n-1]|$$

noise level estimate is updated as follows:

$$|n[n]| = \alpha_{up} \cdot |s_{max}[n]| + (1-\alpha_{up}) \cdot |n[n-1]|$$

  - if the maximum is smaller than the noise level estimate,

$$|s_{max}[n]| < |n[n-1]|$$

noise-level estimate is updated as:

$$|n[n]| = \alpha_{dw} \cdot |s_{max}[n]| + (1-\alpha_{dw}) \cdot |n[n-1]|$$

Time constant values: α_{up} and α_{dw} have been adjusted experimentally to $\alpha_{up} = 0.02$ and $\alpha_{dw} = 0.05$. These values yield adequate noise-level tracking. An example of automatic noise-level tracking is shown in figure 4.

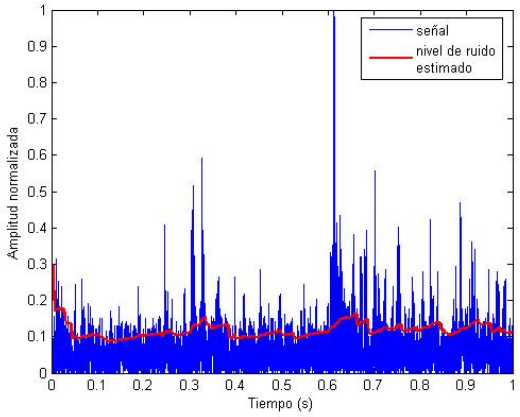

Figure 4: Automatic neural-signal-noise-level tracking example.

3. Wireless transmission

Figure 5 represents the overall transmission scheme. The information source is a PC where neural data recorded by a MEA system are stored. This PC establishes via a Bluetooth-Dongle a wireless communication link with a mobile terminal. The stored data are transmitted over the Bluetooth link from the information source to the mobile device that receives them and, without intermediate storing, re-transmits them via a 3G link to a remote server PC, where the data are definitely stored and processed.

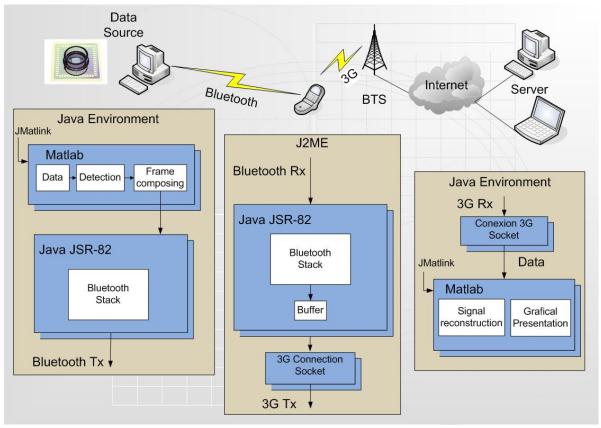

Figure 5: Wireless Bluetooth-3G transmission.

3.1. Bluetooth wireless transmission

Bluetooth is a flexible and capable technology for providing short-range radio communications between devices in an ad-hoc manner using the 2.4 GHz band. It is well suited as a low power radio transceiver (transmitter and receiver) operating at up to 1 Mbps. Two types of channels are used in Bluetooth systems: SCO and ACL. SCO are synchronous connection oriented links with fixed 64 kbps data rate used exclusively for voice traffic; while ACL are Asynchronous Connection-Less links. As shown above in Section 2., streaming of multichannel or even single channel neural signals demands such a bandwidth which can not be offered by SCO links. The Bluetooth connection type capable of flexible and higher bandwidths is the Asynchronous Connection-Less (ACL) link.

Figure 6 shows the core Bluetooth protocol layers. The baseband layer enables the physical RF link between Bluetooth units making a connection. Link Manager Protocol (LAMP) is responsible for link set-up between Bluetooth devices and managing security aspects such as authentication and encryption. L2CAP adapts upper-layer protocols to the baseband. It multiplexes between the various logical connections made by the upper layers. Audio data typically is routed directly to and from the baseband and does not go through L2CAP. SD is used to query device information, services and characteristics of services.

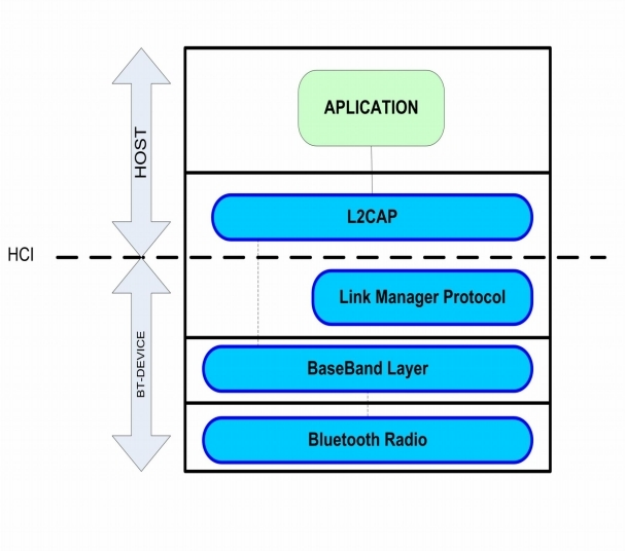

Figure 6: Core Bluetooth Architecture.

Java standard API for Bluetooth: JSR-82

Given that our communication scheme includes a client application implemented on the information source and the server application running on a mobile phone, it is reasonable to choose a Bluetooth programming technology that is provided in nowadays mobile devices. That is why we have decided to use the standard Bluetooth Java programming API "JSR-82" currently supported in a wide range of mobile devices from different manufacturers. JSR-82 API allows us to establish an L2CAP point-to-point connection between client and server devices through which the neural signals are transmitted. JSR-82 supports Bluetooth standard v1.1. which is therefore the version used in our experiments.

Methods

In order to have control over the Bluetooth transmission we have programmed the client and server applications implementing the communication. In our implementation, first, an L2CAP connection is established between the master and the slave. Once communication is established, the client application running on the slave starts sending data over the connection to the masters's server application. The data packet size used in the connection can be selected at compilation time and a 2 Mbyte neuronal signal of the type described in section 2 is used as data source. The transmitter monitors the channel quality by inspecting throughput.

3.2. Transmission over 3G

The third generation transmission standard for mobile communication enhances GPRS in a variety of performance characteristics:

- High transmission rates up to 2 Mbps.
- High security and confidentiality.
- Efficient multiple access.
- High resistance to interferences.
- Global roaming .
- Always on, QoS (Quality of Service).
- Low cost.

In this contribution we have used the 3G technology to transmit the neural data from a mobile terminal to a remote server over public cellular networks. This remote server is either an ordinary PC, a laptop or even a remote MEA connected to a neural culture.

As the mobile device receives the neural data from the information source, these are re-transmitted immediately to the remote server. Once the mobile phone is registered in the network, a profile containing all necessary parameters for the 3G transmission, such as access point etc., is established. The TCP Transmission Control Protocol is used for the data transmission. It offers a point-to-point connection-oriented reliable link recovering a huge variety of errors dynamically and adaptively. In order to use the TCP, the transmitter (in this particular case the mobile phone) and the receiver (equivalent to the remote server in our application) shall create the terminal points of the connection, called sockets. A socket is defined by a transmission protocol (TCP is this case), an IP address and a port number. In out experiments the mobile phone is programmed to be the client. The mobile phone requests the opening of a TCP-socket to the server that is waiting for inquiries.

As already mentioned, the application running on the mobile phone implementing the Bluetooth transmission is programmed in J2ME^{TM} (due to the limited device resources). Contained in this application also the 3G transmission is managed. Also, the server application is programmed using Java.

In Fig. 5 it can be observed that both the application running on the information source PC and the remote server application incorporate the JMATLink software package. This packages allows the integration of MATLAB^{TM} applications with Java applications. Especially for data pre- and postprocessing as well as for real-time data representation this package offers huge advantages. The data compression algorithms described in Section 2.2. are implemented in MATLAB^{TM} and launched by JMATLink. For the evaluation of the transmission, real-time graphical data representation is required on the server, also implemented in MATLAB^{TM} and launched by JMATLink.

4. Results and discussion

Due to the fact that the Bluetooth L2CAP connection is a secure channel, retransmissions assure the correct arrival of each single packet and until the acknowledgment of the former packet does not confirm its correct reception a new packet is not transmitted. For this reason, measuring transmission throughput is equivalent to measuring reception throughput. Moreover, this ensures the real-time transmission as long as the data stream generation velocity (required transmission bandwidth as represented in Fig. 1) does not surpass the channel throughput.

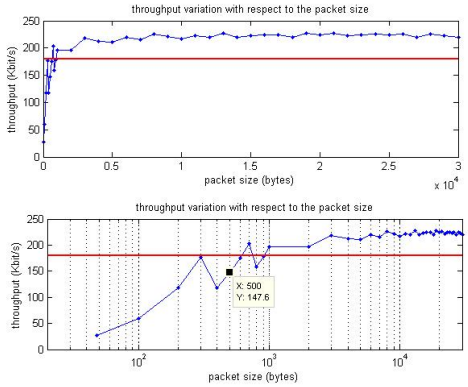

Figure 7: Measured mean throughput with respect to the transmission packet size.

In Fig. 7 the transmission mean throughput in relation to the defined packet size is represented. The mean throughput is calculated as the overall time required for transmission T, measured in nanoseconds, divided by the number of transmitted bits N. As it can be observed from Fig. 7, the mean throughput increases with the packet size. For a packet sizes smaller than 1000 bytes the throughput is below 180 kbps. Due to the fact that the required minimum transmission data rate for neural signals, as described in section 2. by Fig. 1 is 180 kbps, only packet sizes greater than 1000 bytes provide real-time transmission of one neural signal. For these packet sizes (> 1000 bytes) as the packet size increases a saturation in the mean throughput is observed. The obtained maximum mean throughput value is below 230 kbps.

Due to the limited processing and storage capabilities of the mobile phone, the maximum MTU for the Bluetooth transmission is 512 byte offering a data throughput smaller than 180 Kbps (see Fig. 7) as required for the real-time transmission of one neural signal channel. In fact, the transmission rate with an MTU of 512 byte is limited to 147.6 Kbps.

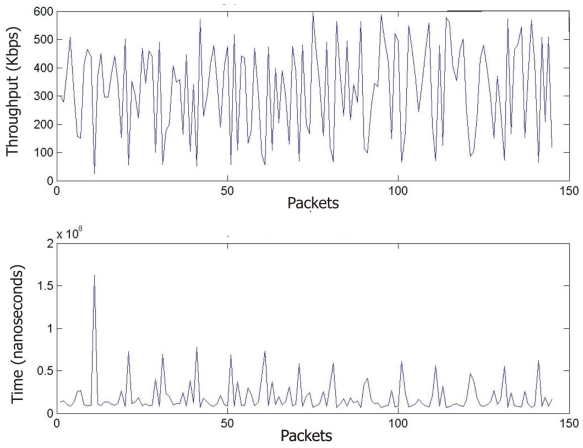

Figure 8: Measured transmission for packet sizes ranging from 48 to 1000 bytes.

Figure 8 shows the time evolution of the mean values represented in Fig. 7. The real-time throughput evolution is represented which is calculated as the ratio between the transmitted packet size and the time needed for this transmission measured in nanoseconds. As it can be observed from Fig. 8, the real-time throughput is not constant, it presents variations around its mean value. The higher the packet size, the higher the mean throughput and also the higher the throughput variance. Therefore, even if the mean throughput is higher than the required 180 kbps limit it can not be guaranteed that the real-time throughput is always higher than this limit, thus implying the need of adequate data compression before transmission.

Analyzing the real-time throughput evolution, it is observed that less than 20% of the measured throughput values fall below the range of the mean value. Therefore, an adequate mean throughput value guaranties the channel capacity for over the 20% of the time.

The developed compression algorithm is able to reduce the required data transmission rate up to 75% depending on the spiking activity of the particular culture. Taking into account that the transmission rate is limited to 147.6 Kbps, taking advantage of the compression algorithm, it is possible to transmit up to 3 neural signals in real-time. In fact, the spiking activity of the neural signal is monitored in real-time and the number of transmitted neural signals is adaptively recalculated. Finally, the most active channels are transmitted in real-time. The measurement of the activity of a channel is performed inspecting the actual compression rate: the more active a channel is, the lower will be its compression rate.

5. Conclusions

In this contribution a wireless transmission system over Bluetooth and 3G is analyzed for its application to

the real-time transmission of neural signals captured by implanted micro-electrode array sensors.

First, the required data rates for this type of neural signals are calculated to be not less than 180 kbps for every single micro-electrode. Thus, for an array of 64 micro-electrodes a minimum transmission rate of 64×180 kbps $= 11520$ kbps is required.

To be able to compress the neural signals, detection of spikes is implemented and up 75% compression rate is achieved. Detection uses a non-linear energy operator preprocessing and automatic threshold adaptation.

The wireless transmission of these signals integrates a Bluetooth transmission from the information source to a mobile device and the data transmission from the mobile device over 3G to a remote server, without intermediate storage on the mobile phone.

The transmission rate is limited by the Bluetooth link, depending on the transmission packet size. Due to the limited resources of the mobile phone, the maximum transmission unit is limited to 512 byte thus achieving a maximum transmission rate of 147.6 Kbps.

With this transmission rate, it is not possible to transmit a neural signal in real-time over the Bluetooth link. Therefore, the compression algorithm is used to enhance the performance of the system allowing the transmission of up to 3 neural signals in real-time.

The complete system, including signal compression, Bluetooth transmission and transmission over 3G, is implemented in Java (JSE for the information source and the remote server, J2ME for the mobile phone) using the package JMATLink to launch MATLAB^{TM} data processing applications.

References

[1] T. Zasowski, F. Althaus, M. Stäger, A. Wittneben, and G. Tröster, "UWB for noninvasive wireless body area networks: Channel measurements and results," in *IEEE Conference on Ultra Wideband Systems and Technologies, UWBST 2003*, nov 2003. [Online]. Available: http://www.nari.ee.ethz.ch/wireless/pubs/p/uwbst2003

[2] B. P. Lo, S. Thiemjarus, R. King, and G.-Z. Yang, "Body sensor network – a wireless sensor platform for pervasive healthcare monitoring," *Gastroenterology*, 2005.

[3] I. Obeid, "A wireless multichannel neural recording platform for real-time brain machine interfaces," Ph.D. dissertation, Department of Biomedical Engineering Duke University, 2004.

[4] "Bluetooth special interest group: Specification of the bluetooth system," 2004. [Online]. Available: http://www.bluetooth.com/Bluetooth/Learn/Technology/Specificatio

[5] M.-G. Di Benedetto and R. v. Branimir, "Ultra wide band wireless communications: A tutorial," *Journal of Communications and Networks*, 2003.

[6] R. Saeed, S. Khatun, B. Mohd Ali, and K. A. Mohd, "Ultra wide band (uwb) ad-hoc networks: Review and trends," *Journal of Computer Science*, 2005.

[7] C. Yi Lee and C. Toumazou, "Ultra-low power uwb for real time biomedical wireless sensing," in *IEEE International Symposium on Circuits and Systems*, may 2005.

[8] J. Ryckaert, C. Desset, A. Fort, M. Badaroglu, V. De Heyn, G. Wambacq, Piet Van der Plas, S. Donnay, B. Van Poucke, and B. Gyselinckx, "Ultra-wideband transmitter for low-power wireless body area networks: design and evaluation," *IEEE Transactions on Circuits ans Systems*, 2005.

[9] D. Barras, F. Ellinger, H. Jackel, and W. Hirt, "Low-power ultra-wideband wavelets generator with fast start-up circuit," *IEEE Transactions on Microwave Theory and Techniques*, 2006.

UWB CHANNEL MEASUREMENTS FOR HAND-PORTABLE DEVICES: A COMPARATIVE STUDY

Cristina Tarín Paula Martí Lara Traver Narcís Cardona Juan A. Díaz Eva Antonino
Telecommunication and Multimedia Applications Institute (iTEAM)
Technical University of Valencia
Camino de Vera s/n, E-46071 Valencia, Spain

ABSTRACT

On-body UWB signal propagation is analyzed using two different types of UWB antennas. For the study, measurements of the frequency response by means of a VNA (Vector Network Analyzer) are performed at 2001 discrete frequency points in the 3 to 6 GHz range. Separated measures are taken for four different transmitter positions on the head and six receiver positions on the body. Channel estimation parameters, such as mean excess delay, delay spread and path loss are obtained. Results are similar for both types of antennas regarding path loss exponent and Average Power Delay Profiles.

I. INTRODUCTION

Wireless Body Area Networks (WBAN) are wireless communication networks where either the transmitter, the receiver or both are placed on the human body. Nowadays, with the raising number of applications in health-monitoring and telemedicine, characterization of the channel behavior involving the human body is becoming increasingly important.

Body-worn devices must be permanently available and, at the same time, operate at a low transmission power, not only because of the body proximity but also in order to extend battery life. In such scenario, Ultra Wideband (UWB) technology appears as an appropriate solution for wireless communication, providing considerable transmission rates at a relatively low power consumption cost.

In the literature, several measurements and models of the UWB channel for indoor and outdoor propagation can be found [1],[2]. Some studies try to model the effects of the human body interfering a wireless network by interposing a person between two antennas [3]. Others[4] consist on measurement campaigns where only the transmit antenna is placed on the body. Additionally, studies performed by Alomani et al [5], [6] place both antennas on the body, but the focus lies in finding out which kind of antennas are best fitted to be used in WBAN channel estimation. Finally, characterization of the channel with transmitter and receiver antennas along the torso is performed in [7]. Despite the above studies, there are few works that take into account the human head. Zasowski et al [8] and [9] demonstrate the propagation mechanisms on the head, like diffraction or absorption, but without an exhaustive analysis of the propagation channel.

The objective of this work is to study the behavior of the UWB channel surrounding the body in a usual office environment for an specific application: the transmission of signals recorded from the head to a device such as a mobile phone or a PDA that the same person is carrying. To the authors' knowledge, such kind of study has not yet been published. The measurement campaign was carried out in the office environment to obtain a realistic channel model. For comparison, each measurement was repeated using two types of antennas with similar characteristics but provided by different manufacturers.

In this paper, section II. describes the measurement setup. Section III. presents and discusses measurement results for both types of antennas and implications for receiver design. Finally, section IV. deals with conclusions and further work.

II. MEASUREMENT SETUP

Measurements were performed in an large office room (8m x 17m) with metallic furniture like desks or cabinets. A Vector Network Analyzer (VNA) was used and the complex frequency transfer function of the channel, S-parameter S_{21}, was recorded for a large set of discrete frequencies in the range from 3 to 6 Ghz. The particular vector network analyzer was the ZVA24 model from Rhode & Schwarz. This analyzer allows measuring magnitude and phase of a signal from 10 MHz to 24 GHz with up to 135 dB dynamic range. Two antennas are connected to the VNA by means of 5m length RG-223 cables. These cables are suitable for working in ranges up to 12.4 GHz and their attenuation will not affect the measure thanks to the calibration process of the VNA.

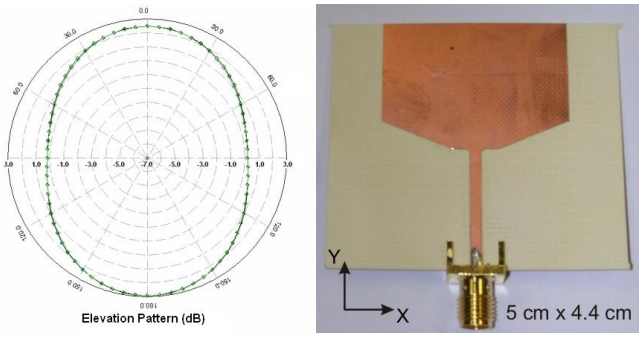

Figure 1: iTEAM UWB antenna (right) and its radiation pattern in the XZ plane at 3.1 GHz (left)

With respect to the antennas, two types of omnidirectional antennas were selected. First, a pair of antennas provided by Wisair, suitable for UWB measures and, second, a pair of UWB antennas designed and manufactured by the iTEAM. Figure 1 shows the latter antenna type together with a representation of its radiation pattern in the XZ plane. The antenna presents similar behavior in the rest of planes. Considering the frequency

1-4244-1144-0/07/$25.00©2007 IEEE

domain, as one can see in figure 2, S_{11} has a relatively flat response for the frequency range used in our channel measurements (3-6 GHz).

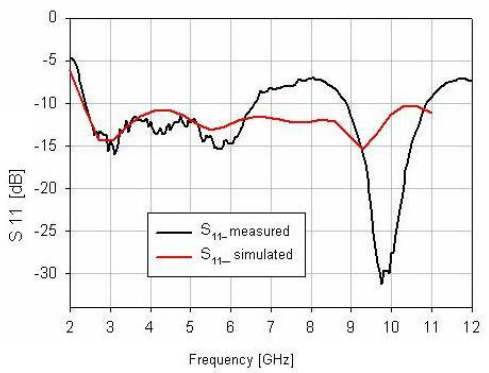

Figure 2: S_{11} versus frequency for the iTEAM UWB antenna

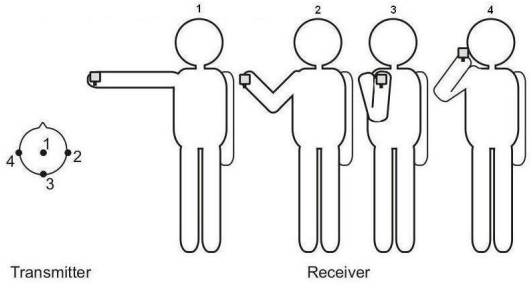

		rx1 (extended)	rx2 (half ext.)	rx3 (bent)	rx4 (talk)	rx5 (front pocket)	rx6 (back pocket)
tx1 (top)	channel	ch 1	ch 2	ch 3	ch 4	ch 5	ch 6
	d [m]	0,84	0,50	0,37	0,20	0,85	0,92
tx2 (right)	channel	ch 7	ch 8	ch 9	ch 10	ch 11	ch 12
	d [m]	0,86	0,50	0,30	0,22	0,80	0,85
tx3 (back)	channel	ch 13	ch 14	ch 15	ch 16	ch 17	ch 18
	d [m]	0,80	0,46	0,33	0,16	0,80	0,80
tx4 (left)	channel	ch 19	ch 20	ch 21	ch 22	ch 23	ch 24
	d [m]	0,70	0,38	0,26	0,60	0,70	0,78

Figure 3: Transmitter and receiver locations.

As depicted in figure 3, several measurements were performed corresponding to different positions of the antennas. The transmitter was placed on the head at four different locations: top, right side, left side and back of the head, while, given that the receiver is expected to be a hand-held device, receiver antenna was placed at six probable hand-held device locations along the body: in the hand with extended arm, in the hand with half extended arm, in the hand with the arm flexed to the chest, near the ear (talking on the phone), in the front pocket and in the back pocket. Measurements between each transmitter and each receiver result in 24 different arrangements corresponding to 24 different propagation channels. The table in figure 3 shows the transmitter and receiver positions together with the corresponding channel number and the distance of the link.

For each channel, measurement of 2001 discrete frequency points in the 3 to 6 GHz range was repeated 200 times. To ensure enough dynamic range, a transmission power of 0 dBm was used and to include even the further reflections, 600 ns of the signal were recorded. Finally, the average of the 200 measures was then calculated in order to reduce the error due to channel variability.

III. Measurement results and discussion

Measured UWB links correspond to very different propagation cases, given that in some of them there is a LOS link between transmitter and receiver while in others there is shadowing by the body. This results in different propagation conditions for each of the cases and, therefore, characterization parameters corresponding to the different types of such links are expected to differ considerably due to link geometry variability.

A. *Path loss*

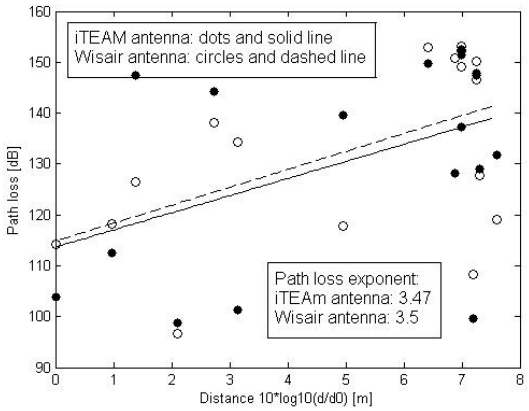

Figure 4: Path loss for on-body channels using iTEAM UWB antennas (solid) and Wisair antennas (dashed). Linear models by best fit are also shown.

Figure 4 shows the measured path loss for each of the 24 static channels versus the logarithmic distance between transmitter and receiver normalized to the minimum link distance (20cm). Measures corresponding to the two types of antennas are separated (iTEAM antenna: dots and solid line, Wisair antenna: circles and dashed line). One can note that the calculated path loss increase exponent is consistent regardless of the antenna. Path loss variability comparing all the measured channels amounts to 55 dB.

B. *Averaged power delay profile*

Figures 5 to 8 show calculated Average Power Delay Profiles (APDP) for each measured channel. Figure 5 presents the subset of channels corresponding to the transmitter position 1 and receiver at the 6 defined positions. Analogously, figures 6 to 8 correspond to measures for transmitter positions 2 to 4. Moreover, APDPs for each of the two types of antennas are grouped in pairs corresponding to the same channel. For the sake of clarity, channel number and antenna type are labeled in the y-axis and channels are ordered with respect to the increasing distance between transmitter and receiver.

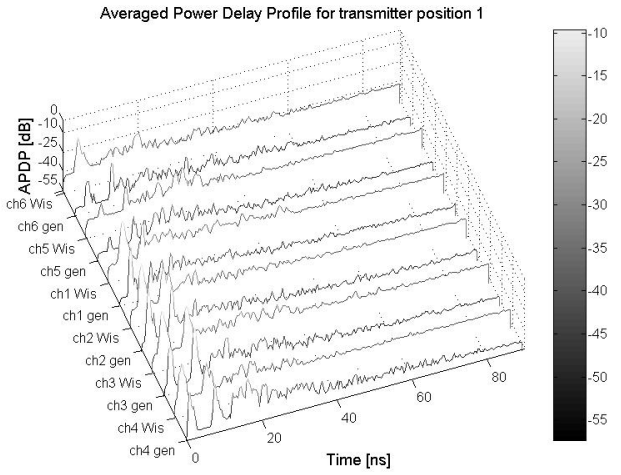

Figure 5: Averaged Power Delay Profiles for channels corresponding to transmitter in position 1.

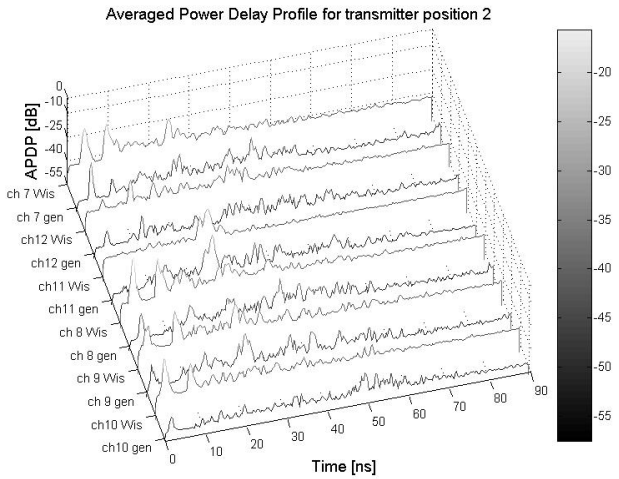

Figure 6: Averaged Power Delay Profiles for channels corresponding to transmitter in position 2.

From the Averaged Power Delay Profiles (APDPs), different signal contribution clusters can be observed. The first cluster, constituted by peaks from 1 to 6 ns, corresponds to contributions of paths around the body, while clusters starting from 8 ns are due to reflections on the various environment surfaces.

For transmitter position 1, measures with both antennas are similar in most cases. In general one can observe a first Multi-Path Component (MPC) cluster with a strong peak corresponding to the contribution from the direct path. Peak position increases gradually from 1 to 4 ns as the distance between transmitter and receiver increases. After the first MPC there is a silence lasting for 2-3 ns until the next MPC corresponding to the first reflection arrives. First reflected contributions start at 8 ns and are due to the floor and the ceiling. Channel 6, which corresponds to the receiver positioned in the back pocket presents a differing measure for the two antennas. While Wisair APDP presents a much stronger direct path component, it lacks a significant reflection peak coming from a near surface. Such disagreement arises from differences between the antennas' radiation patterns in the YZ plane.

In figure 6 we can see the APDPs for the channels where the transmitter is in position 2 (right side of the head) and receiver is in each of the 6 positions along the left side of the body. In this case there is strong shadowing created by the body between transmitter and receiver. From these APDPs one can see that direct path contributions are much smaller than for the previous case seen in figure 5. It is also noticeable a slight difference between measures taken with the two types of antennas. Measures with Wisair antenna show stronger peaks in the first MPC cluster.

In figure 7 (transmitter in the back of the head and the receiver at 6 positions along the left side of the body), it is specially important to see that there is one channel (channel 17) with almost flat APDP for both antennas. This channel corresponds to the receiver in the front pocket. In this case shadowing created by the body and possible cancelation of reflections

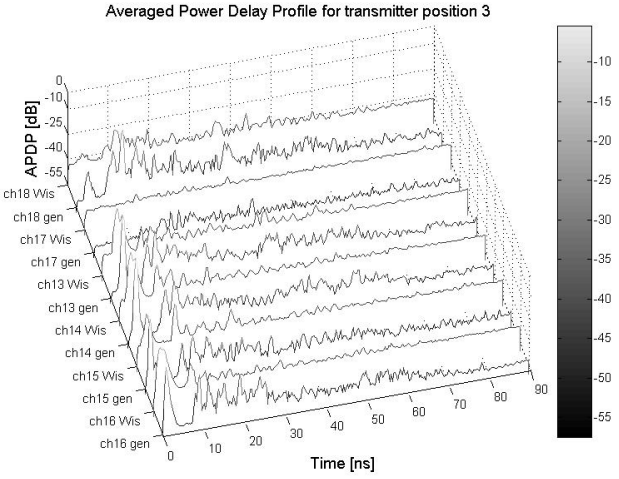

Figure 7: Averaged Power Delay Profiles for channels corresponding to transmitter in position 3.

by the antenna radiation pattern are the reason of the lack of strong peaks.

In figure 8 one can observe that the lack of strong contributions mentioned for channel 17 is repeated for channel 23, which is also the one with the receiver in the front pocket.

C. *Mean delay of strongest and first echo, mean excess delay and delayspread*

Figure 9 shows the Mean Delay of Strongest Echo MDSE for iTEAM and Wisair antenna plotted for the different distances of the evaluated links. The links which are LOS are represented separately from those which are NLOS. As it can be observed, for both antennas the results are quite similar. The linear increase for LOS and NLOS channels for both antennas are similar. As expected, the LOS channels show an smaller MDSE than the NLOS channels, for both antennas. Also, as expected, for the NLOS channels the distance is more relevant

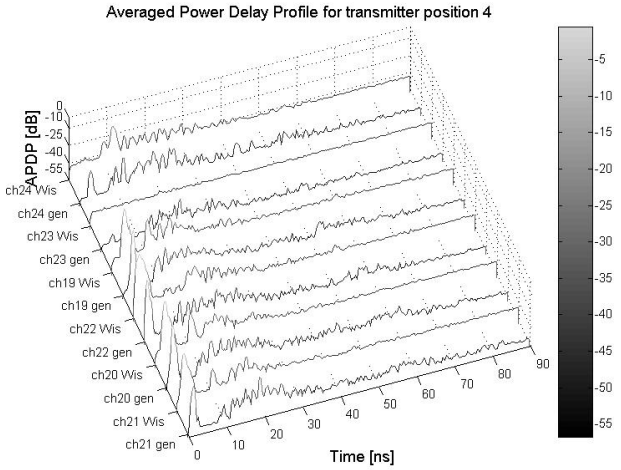

Figure 8: Averaged Power Delay Profiles for channels corresponding to transmitter in position 4.

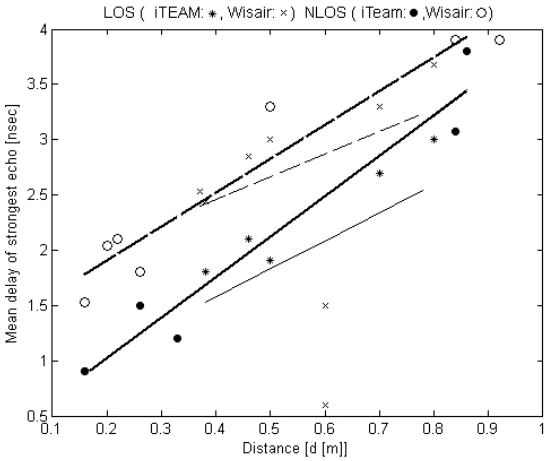

Figure 9: Mean Delay of Strongest Echo for iTEAM (solid) and Wisair (dashed) for LOS and NLOS channel. Linear models by best fit are also shown.

in the MDSE than for the LOS channels. The larger slope of the linear fit for NLOS channels (for both antennas) makes this relationship apparent. The main difference between the two evaluated antennas is that the Wisair antenna shows a larger MDSE than the iTEAM antenna for both LOS and NLOS channels. This is due to the poor adaption of the Wisair antenna leading to phase shift and MDSE enlargement. To characterize the APDP the delayspread τ_{rms} is calculated as the square root of the second central moment of $|h(\tau)^2|$. The mean τ_{rms} for iTEAM and Wisair antenna classified per LOS and NLOS channels is shown in Table 1. As expected, for NLOS the delayspread is larger than for LOS channels. Also in this case, the poor adaptation of the Wisair antenna leads to a larger delayspread (in both cases LOS and NLOS) than that obtained with iTEAM antenna.

As an example of these relationships figure 10 shows the APDP measured with the iTEAM antenna (top) and the Wisair

		Delayspread [ns]
iTEAM	LOS	0.2484
	NLOS	1.0198
Wisair	LOS	0.4932
	NLOS	1.1096

Table 1: Delayspread for LOS and NLOS channels, for iTEAM and Wisair antennas.

antenna (bottom) for LOS and NLOS channels. As it can be observed, the delayspread is much larger for NLOS than for LOS channel.

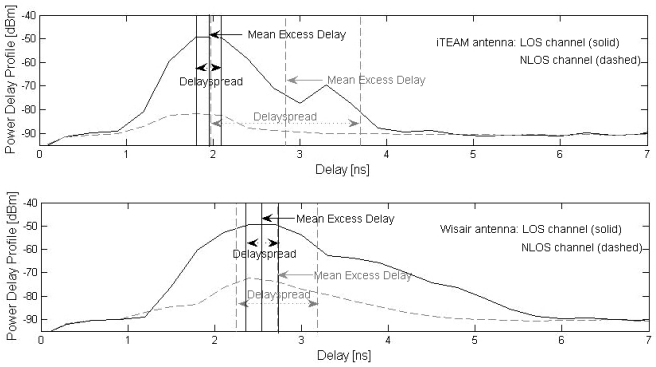

Figure 10: Averaged Power Delay Profiles for iTEAM and Wisair antenna: Mean Excess Delay and Delayspread.

Compared to the results obtained for the MDSE, also in the case of the Mean Delay of First Echo MDFE both the iTEAM and the Wisair antenna show similar behavior. In figure 11, the MDFE for two different transmitter positions, namely 4 (top) and 2 (bottom) is depicted. The MDFE is larger for the Wisair antenna than for the iTEAM antenna due to poor adaptation of the Wisair antenna. The slopes of the linear fits are similar for both antennas.

Figure 12 (top) shows both the MDSE (black circles) and the MDFE (grey squares) for all measured channels with the iTEAM antenna. For those measurements, where MSFE and MDSE are the same, only the MDFE is represented. Additionally, the arrival time of the first non-direct path contribution (reflection on ceiling or floor) is represented for each channel (black line). As it can be observed from figure 12 (top), for all LOS channels, the MDSE is smaller than the arrival time of the first non-direct path contribution. In figure 12 (bottom) the percentage of receiver power is represented for all channels. In fact, here it is shown the relation between the power collected up to the first non-direct path contribution arrival time and the total received power. As it can be observed, for those channels that present the MDSE after the arrival time of the first non-direct path contribution (represented in black dots), the relative power sinks below 10% of the total received power. For the other channels, a receiver using power up to the first non-direct

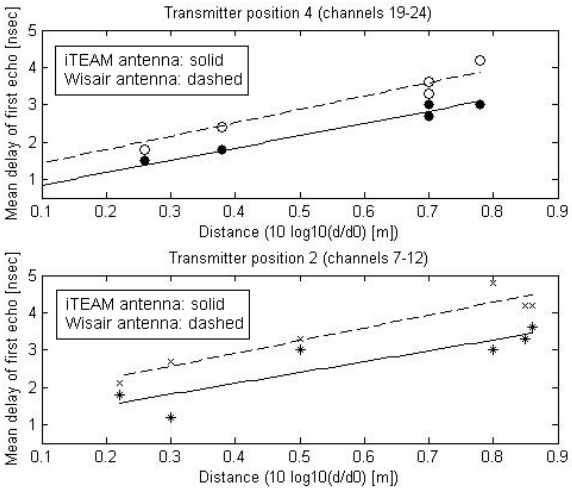

Figure 11: Mean Delay of First Echo for transmitter position 4 and 2.

path contribution ensures a useful power percentage of more than 20%. LOS channels present better average power relation of 42% than NLOS channels with 10.5%.

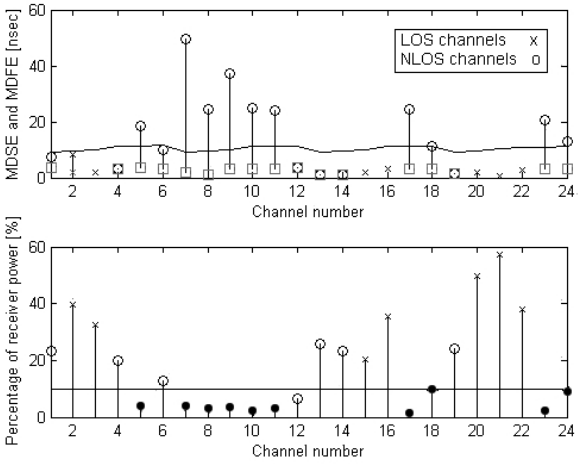

Figure 12: MDSE and MDFE for LOS and NLOS channels (top) and receiver power percentage (bottom).

IV. Conclusions and Further Work

In the present work, UWB on-body channel measurements are performed in an office environment and channel characteristics are studied for 24 different combinations of transmitter and receiver positions. Furthermore, separate measures are taken for two types of UWB antennas.

As we have seen in the previous section, the studied antennas show only a slightly different effect on the measures. The difference becomes relatively more significant for channels where the line of sight is in the YZ plane of the radiation pattern, therefore, the effects of the proximity of the body to the antenna's radiation pattern in the YZ plane should be further studied. All in all, the path loss increase exponent is consistent regardless of the antenna and path loss variability comparing all the measured channels amounts to 55 dB.

From APDPs different signal contribution clusters are observed: The first cluster constituted by peaks from 1 to 6 ns corresponds to contributions of paths around the body, while clusters starting from 8 ns are due to reflections on the various environment surfaces. For strong body-shadowing channels (NLOS), the direct path contributions are much smaller than for LOS links.

Analyzing MDSE, MDFE and delayspread it is concluded that the linear increase of MDSE with distance for LOS and NLOS channels for both antennas are similar. As expected, the LOS channels show an smaller MDSE than the NLOS channels and for NLOS channels the distance is more relevant in the MDSE than for the LOS channels, for both antennas. For NLOS the delayspread is larger than for LOS channels. Poor adaptation of the Wisair antenna leads to phase shift and causes augmentation of MDSE, MDFE and delayspread.

Results have also shown that signal contributions arriving at the receiver that correspond to paths around the body are subject to severe fluctuations depending on the transmitter and receiver locations. Therefore, when it comes to the design of the receiver it will be necessary to use signal coming from ceiling or floor reflection in order to increase the signal to noise ratio.

References

[1] Andreas F. Molisch "Ultrawideband propagation channels-theory, measurement, and modeling" *IEEE Transactions on Vehicular Technology* vol. 54, no. 5, 2005.

[2] A. Muqaibel and A. Safaai-Jazi and A. Attiya and B. Woerner and S. Riad "Path-Loss and Time Dispersion Parameters for Indoor UWB Propagation" *IEEE transactions on wireless communications* vol. 5, no. 3, 2006.

[3] I. Zoubir and J. Dacuña and G.J.M. Janssen and H. Nikookar "UWB Channel Measurements and Results for Wireless Personal Area Networks Applications" *in Proceedings of the European Conference on Wireless Technology*, 2005, pp. 189-192

[4] T.B. Welch and R.L. Musselman and B.A. Emessiene and P.D. Gift and D.K. Choudhury and D.N. Cassadine and S.M. Yano "The effects of the human body on UWB signal propagation in an indoor environment" *IEEE Journal in selected areas in communications* vol. 20, no. 9, 2002.

[5] A. Alomainy and Y. Hao and C.G. Parini and P.S. Hall "Comparison Between Two Different Antennas for UWB On-Body Propagation Measurements" *Antennas and Wireless Propagation Letters* vol. 4, 2005.

[6] A. Alomainy and Y. Hao "Radio Channel Models for UWB Body-Centric Networks with Compact Planar Antenna" *in Proceedings of the IEEE International Symposium on Antennas and Propagation*, 2006, pp. 2173-2176

[7] T. Zasowski and F. Althaus and M. Stäger and A. Wittneben and G. Tröster "UWB for noninvasive wireless body area networks: Channel measurements and results" *in Proceedings of the IEEE Conference on Ultra Wideband Systems and Technologies*, 2003.

[8] T. Zasowski and G. Meyer and F. Althaus and A. Wittneben "Propagation Effects in UWB Body Area Networks" *in Proceedings of the IEEE International Conference on Ultra-Wideband*, 2005, pp. 16-21

[9] T. Zasowski and G. Meyer and F. Althaus and A. Wittneben "UWB Signal Propagation at the Human Head" *IEEE Transactions on Microwave Theory and Techniques* vol. 54, no. 4, 2006.

UWB Channel measurements for measures for hand-portable and wearable devices

Cristina Tarín Lara Traver Paula Martí Narcís Cardona Juan A. Díaz Marta Cabedo
Telecommunication and Multimedia Applications Institute (iTEAM)
Technical University of Valencia
Camino de Vera s/n, E-46071 Valencia, Spain
{critasa,latrase,paumarro,ncardona,judiase,marcafab}@iteam.upv.es

Abstract

On-body UWB signal propagation is analyzed for propagation channels surrounding the body in an usual office environment for an application requiring the transmission of signals recorded from the head to a device such as a mobile phone or a PDA carried by the subject or also from the transmitter on the head to other devices located along the body. For the study, measurements of the frequency response by means of a VNA (Vector Network Analyzer) are performed at 2001 discrete frequency points in the 3 to 6 GHz range. Channel estimation parameters, such as mean excess delay, delay spread and path loss are obtained. Results show that for the transmitter located on top of the head best average performance is achieved facilitating the receiver design. Energy can also be captured from multipath reflections in the office environment providing better performance when using adaptive receivers.

1. Introduction

Wireless Body Area Networks (WBAN) are wireless communication networks where either the transmitter, the receiver or both are placed on the human body. Nowadays, with the raising number of applications in healthmonitoring and telemedicine, characterization of the channel behavior involving the human body is becoming increasingly important.

Body-worn devices must be permanently available and, at the same time, operate at a low transmission power, not only because of the body proximity but also in order to extend battery life. In such scenario, Ultra Wideband (UWB) technology appears as an appropriate solution for wireless communication, providing considerable transmission rates at a relatively low power consumption cost.

In the literature, several measurements and models of the UWB channel for indoor and outdoor propagation can be found [1], [2]. Some studies try to model the effects of the human body interfering a wireless network by interposing a person between two antennas [3]. Others [4] consist on measurement campaigns where only the transmitter antenna is placed on the body. Additionally, studies performed by Alomani et al. [5] place both antennas on the body, but the focus lies in finding out which kind of antennas are best fitted to be used in WBAN channel estimation. Finally, characterization of the channel with transmitter and receiver antennas along the torso is performed in [6]. Despite all the above studies, it has been found that there are few works taking into account the human head.

The objective of this work is to study the behavior of the UWB channel surrounding the body in an usual office environment for a specific application: the transmission of signals recorded from the head to a device such as a mobile phone or a PDA that the person is carrying or also from the transmitter on the head to other devices located along the body. In future medical applications those devices would be either monitoring or active devices. To the authors' knowledge, such kind of study has not yet been published.

2. Measurement setup

Measurements are performed in a large office room (8m x 17m) with metallic furniture. A Vector Network Analyzer (VNA) is used and the complex frequency transfer function of the channel, S-parameter S_{21}, is recorded. Specifically, the particular VNA is the ZVA24 model from Rhode & Schwarz. This analyzer allows measuring magnitude and phase of a signal from 10 MHz to 24 GHz with up to 135 dB dynamic range. Two antennas are connected to the VNA by means of 5m length RG-223 cables. These cables are suitable for working in ranges up to 12.4 GHz and their attenuation will not affect the measure thanks to the calibration process of the VNA.

Third IEEE International Conference on
Wireless and Mobile Computing, Networking and Communications (WiMob 2007)
0-7695-2889-9/07 $25.00 © 2007 IEEE

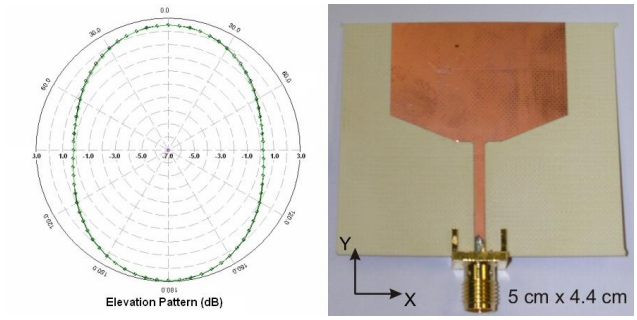

Figure 1. iTEAM UWB antenna (right) and its radiation pattern at 3.1 GHz (left)

With respect to the antennas, a pair of UWB antennas designed and manufactured by the iTEAM are used. Figure 1 shows one of the antennas together with a representation of its radiation pattern in the XZ plane. Considering the frequency domain, S_{11} has a relatively flat response for the measured frequency range (3-6 GHz).

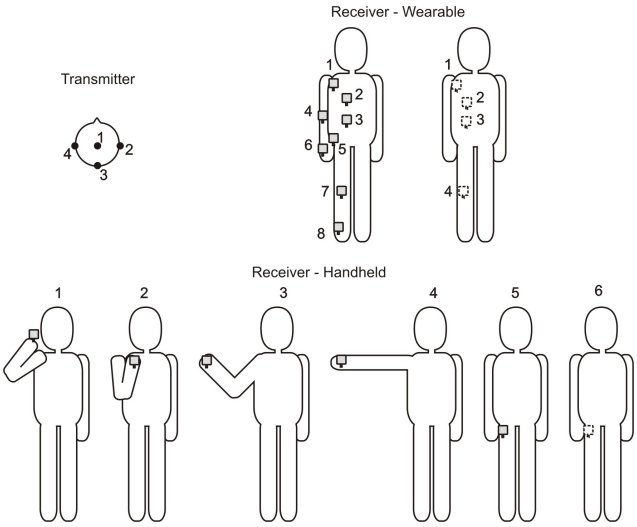

Figure 2. Transmitter and receiver locations.

As depicted in Fig. 2, several measurements are performed corresponding to different positions of the antennas. The transmitter is placed on the head at four different locations: top, right side, left side and back of the head. Receiver is according to two different types of applications. First, for applications were the receiver is a handheld device, receiver antenna is placed at six probable handheld device locations along the body: in the hand with extended arm, in the hand with half extended arm, in the hand with the arm flexed to the chest, near the ear (talking on the phone), in the front pocket and in the back pocket. Second, assuming the receiver would be a wearable device, locations of the receiving antenna are set along 12 different positions along the front and back of the human body. Measurements between each transmitter and each receiver result in a total of 72 different arrangements corresponding to 72 different propagation channels. Table 1 shows the transmitter and receiver positions together with the corresponding channel number and the distance of the link.

Receiver position	Channel nr.	Link distance [m]			
		TX1	TX2	TX3	TX4
Wearable front					
1	1	0.35	0.33	0.3	0.2
2	2	0.4	0.36	0.35	0.3
3	3	0.6	0.5	0.5	0.5
4	4	0.7	0.65	0.55	0.57
5	5	0.8	0.7	0.7	0.6
6	6	0.9	0.85	0.8	0.77
7	7	1.25	1.05	1.1	1.1
8	8	1.6	1.5	1.4	1.4
Wearable back					
1	9	0.42	0.35	0.27	0.3
2	10	0.5	0.4	0.32	0.4
3	11	0.7	0.55	0.5	0.54
4	12	1.25	1.1	1	1.1
Handheld					
1	13	0.84	0.86	0.8	0.7
2	14	0.5	0.5	0.46	0.38
3	15	0.37	0.3	0.33	0.26
4	16	0.2	0.22	0.16	0.6
5	17	0.85	0.8	0.8	0.7
6	18	0.92	0.85	0.8	0.78

Table 1. Transmitter and receiver positions with channel number and link distance.

For each channel, measurement of 2001 discrete frequency points in the 3 to 6 GHz range was repeated 200 times. To ensure enough dynamic range, a transmission power of 0 dBm was used and to include even the further reflections, 600 ns of the CIR (Channel Impulse Response) were recorded. Finally, the average of the 200 measures was then calculated in order to reduce the error due to channel variability.

3. Measurement results and discussion

Measured UWB links correspond to very different propagation cases, given that in some of them there is a LOS link between transmitter and receiver while in others there is shadowing by the body. This results in different propagation conditions for each of the cases and, therefore, characterization parameters corresponding to the different types of such links are expected to differ considerably.

Third IEEE International Conference on
Wireless and Mobile Computing, Networking and Communications (WiMob 2007)
0-7695-2889-9/07 $25.00 © 2007 IEEE

3.1. Path loss

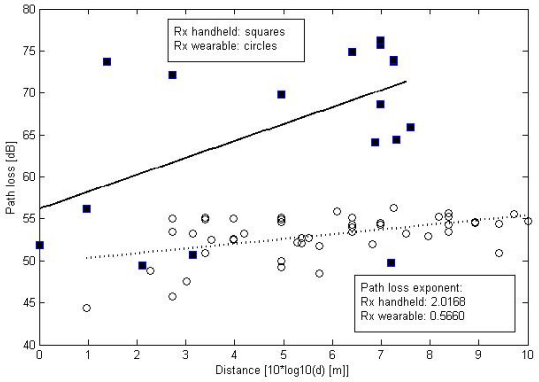

Figure 3. Path loss for channels with handheld and wearable receiver.

Figure 3 shows the measured path loss for each of the 72 static channels (except for those channels which offer direct line of sight LOS) versus the logarithmic distance between transmitter and receiver normalized to the minimum link distance. Measures corresponding to the two types of channels are marked by squares for the handheld receiver device and circles for the wearable receiver device.

One can note that for channels with handheld receiver the path loss variability amounts to 25 dB while for the channels with wearable receiver it reduces to 10 dB. In addition, it can be observed that the mean path loss for channels with handheld receiver is larger than for those with wearable receiver. Both issues can be explained with the fact that the shadowing produced by the head is much more significant for channels with the receiver in handheld positions than for those where the receiver is located at wearable sites along the body. In fact, the more meaningful the shadowing gets, the greater becomes the attenuation reverting in a path loss increase.

Figure 4 shows the path loss together with the linear fits of 72 measured static channels sorted by the transmitter position. It can be observed that the path loss is similar for transmitter positions 1 and 2, which is represented by the path loss exponents. On the other hand, also the path loss obtained for transmitter positions 3 and 4 are similar (similar path loss exponents). In fact, transmitter positions 3 and 4 are those which offer more probability of LOS links than transmitter positions 1 and 2.

3.2. Averaged power delay profile

Figures 5 and 6 show calculated Average Power Delay Profiles (APDP) for each of the 72 different measured

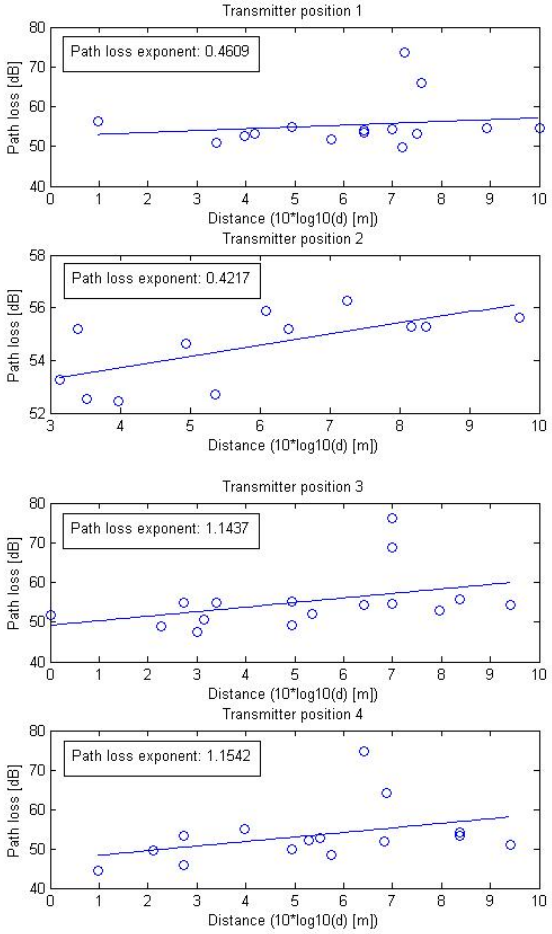

Figure 4. Path loss transmitter positions 1-4.

channels. For each transmitter position, individual channel APDPs have been grouped in 3 sets along the y axis corresponding to: first, 8 positions for a wearable sensor along the front part of the body, second, 4 positions for a wearable sensor on the back part of the body and, third, 6 positions for a hand-held device. For the sake of clarity, the receiver positions are labeled along the y-axis and, among members of the same group, channels are ordered with respect to the increasing distance between transmitter and receiver.

Looking globally at the whole set of measured APDPs, one can clearly differentiate separate signal contribution clusters. First, a Multi-Path Component (MPC) cluster constituted by peaks from 1 to 6 ns and corresponding to contributions of paths around the body, followed by a small period of silence and a second cluster starting from 8 ns and originating from reflections on the various environment surfaces.

For transmitter position 1, it can be observed that the strongest peak falls on the first MPC Cluster in handheld receiver related channels, whereas for wearable receiver posi-

Third IEEE International Conference on
Wireless and Mobile Computing, Networking and Communications (WiMob 2007)
0-7695-2889-9/07 $25.00 © 2007 IEEE

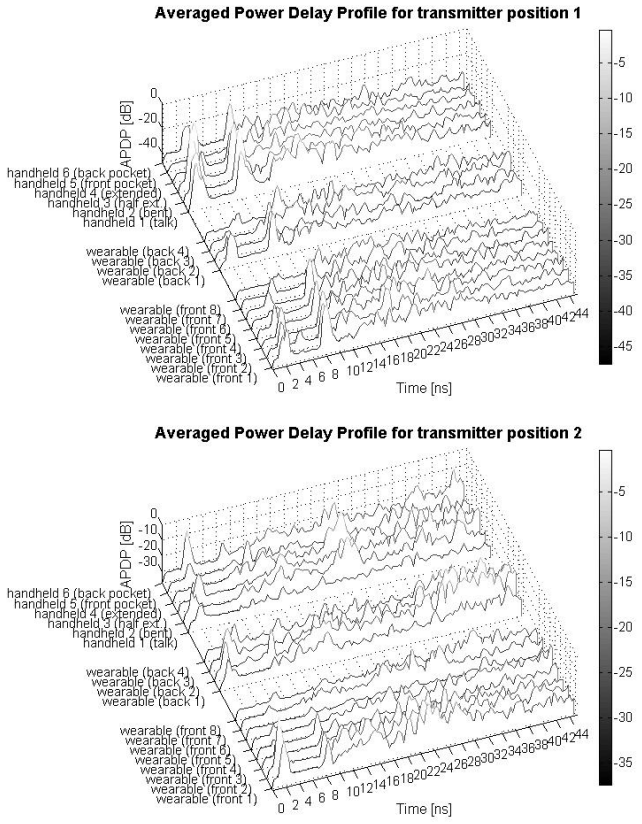

Figure 5. APDP for transmitter positions 1-2.

tions it lies in the second MPC. This MPC cluster starts just after 8 ns and corresponds to reflections on the surrounding surfaces, mainly the floor and the ceiling. Such difference is due to body shadowing given that the transmitter is on the top of the head and receiver is along the body. On the other hand, the common pattern for all the channels is the existence of a strong contribution before 6 ns and a second one after 8 ns. Delayed position of the peaks with the increasing distance can be observed. However, there is an exception for channels corresponding to receiver positions 'front 7', 'front 8' and 'front pocket', in which peaks in both first and second clusters are very weak.

When it comes to transmitter at position 2, the receiver positions are all on the opposite side. Therefore the majority of channels related to transmitter position 2 are NLOS channels. Furthermore, strong shadowing from the body is expected in them. Looking at the plotted results, one can see that, indeed, there are some channels with very weak peaks in the first and second MPC clusters; namely, channels for wearable receiver at front positions 3 to 8.

Comparing with transmitter position 1, in transmitter position 2, the MPCs from the first cluster before 6 ns dominate, while the ones corresponding to reflections on the ceiling and floor do not contribute as strongly to the total power as for position 1. On the other hand, in an analogous way as for transmitter position 1, channels along the front part of the body from 3 to 8 suffer from very strong shadowing of the body and the direct path contribution is almost null. This fact, together with the lack of a strong reflection peak produced by the ceiling or the floor, suggest that the receiver power may be eventually low for this transmission arrangements and that will have receiver design implications. For the positions on the back part of the body the power is distributed similarly, with only some more weight for the first cluster components. Finally, for handheld device positions, there is an important direct-path contribution and also the ceiling or floor contributions are lacking. However, a later peak appears around 20 ns and is probably due to the room walls.

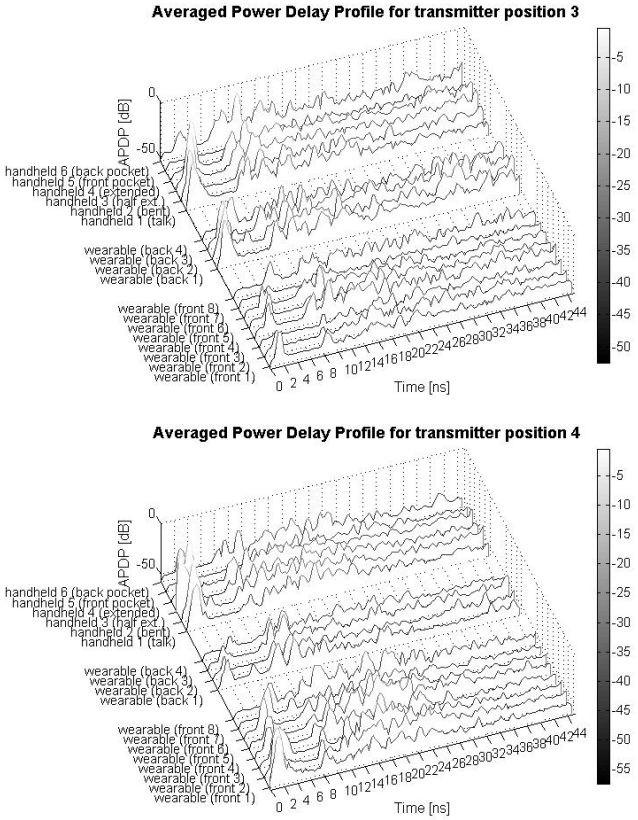

Figure 6. APDP for transmitter positions 3-4.

For transmitter position 3, it can be observed from the APDPs that direct path or LOS contributions are strong for all the channels with receiver at handheld positions and at wearable back part of the body positions. However, as it can be expected, channels with receiver in the front part of the body are lacking a clear contribution before 8 ns. There is one channel, the one with the receiver in the front pocket,

which shows almost flat APDP. In this case shadowing created by the body and possible cancelation of reflections by the antenna radiation pattern are the reasons behind the lack of strong peaks.

Finally, for transmitter position 4, the remarkable characteristics of these APDPs are that, all the wearable along the body positions and the handheld positions present strong direct-path contributions, whereas for back part of the body and front and back pocket positions there is low power concentration before 6 ns. Similarly to the transmitter position 3 case, one can observe that the lack of any strong MPC for the channel with the receiver at the front pocket is repeated here.

3.3. Mean excess delay and delay spread, mean delay of strongest and first echo

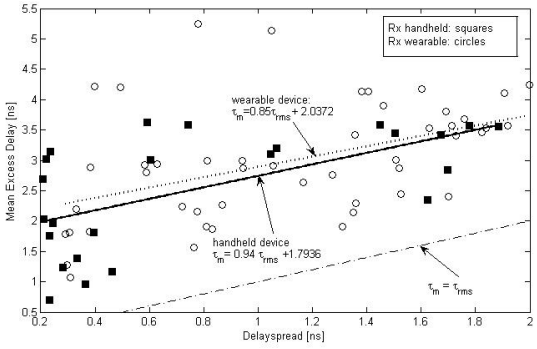

Figure 7. Mean excess delay vs. delay spread.

To characterize the power delay profile, the mean excess delay τ_m and the delay spread τ_{rms} are used, represented in Fig. 7 for both types of channels (handheld receiver and wearable receiver). As it can be observed from Fig. 7, the linear fits for both types of channels are very similar. Moreover, it can be noted that for all of the 72 measured channels $\frac{\tau_m}{\tau_{rms}} > 1$. This means that in general the power concentration is not tight, energy arrives distributed all over the power delay profile and not concentrated at the earliest part.

Figure 8 shows both the Mean Delay of Strongest Echo MDSE ('$*$' for wearable device, '$\diamond$' for handheld device) and the Mean Delay of First Echo MDFE ('o' for wearable device, '$\square$' for handheld device) for all measured channels ordered by transmitter position 1-4. Additionally, the arrival time of the first non-direct path contribution (reflection on ceiling or floor) is represented for each channel (black line). As it can be observed from Fig.8, some of the measured channels, such as channel 5 transmitter position 1 and 2, present a very large MDSE (around 20 ns and 55 ns, respectively). For these channels, the APDP is almost flat and therefore power contribution of the first echo and the power contribution of the strongest echo is similar, not showing any pronounced echo. It shall be pointed out, that for the transmitter in position 1, 3 and 4 the percentage of channels with this particular characteristic is much lower (11.1%, 22.2% and 27.7% respectively) than for transmitter in position 2 (72.2%). In sight of these results it can be concluded that transmitter positions 1, 3 and 4 provide better signal characteristics, which is due to the fact that the echoes from the ceiling are meaningful for transmitter position 1 and 3 and that the direct path is considerable for transmitter position 4. The shadowing is more significant for transmitter position 2, which corresponds to the lateral site of the head opposite to the receiver. When it comes to receiver positions at the back part of the body (channels 8-12) best performance is observed for transmitter position 3 due to the fact that more power is received from the direct contribution.

In Fig. 8, the percentage of receiver power is represented for all 72 channels, also ordered by transmitter positions from 1 to 4. In fact, here it is shown the relation between the power collected up to the first non-direct path contribution arrival time and the total received power. For those channels that present the MDSE after the arrival time of the first non-direct path contribution (represented by '$\triangle$'), the relative power sinks below 10% of the total received power. All LOS channels (represented by '∇') present a relative useful power relation larger than 10% (see channels 14 and 15 for transmitter position 1, channels 15 and 16 for transmitter position 3, channels 13, 15 and 16 for transmitter position 4). As it can be observed, these LOS channels present the highest useful power relation: near 60% for channel 13 of transmitter position 4. Again, for transmitter positions 1, 3 and 4 better performance is observed as shadowing is not so significant.

4. Conclusions

In the present work, UWB on-body channel measurements are performed in an office environment and channel characteristics are studied for 72 different combinations of transmitter and receiver positions. The transmitter is located on 4 different emplacements on the head, while the receiver is placed on 18 different handheld or wearable positions around the human body.

Results show that, for channels with handheld receiver the mean path loss and its variability are higher than for channels with wearable receiver. The shadowing produced by the head is much more significant for channels with the receiver in handheld positions than for those where the receiver is located at wearable sites along the body. Best results are achieved when the transmitter is located at the top of the head, back head and lateral of the head close to re-

Third IEEE International Conference on
Wireless and Mobile Computing, Networking and Communications (WiMob 2007)
0-7695-2889-9/07 $25.00 © 2007 IEEE

ceiver emplacements, while the lateral of the head opposite site of receiver emplacements leads to poorer characteristics.

From calculated APDPs, similar conclusions to those above can be extracted. The smaller time figures are obtained for channels corresponding to transmitter positions 4 and 1, in this order. The longer energy-span windows correspond to channels for transmitter position 2.

To characterize the APDPs, the mean excess delay and the delay spread are used. The time dispersion of the UWB pulses are characterized by the ratio of the average arrival time to the spread of the arrival time resulting in a poor power concentration: energy arrives distributed all over the power delay profile and not concentrated at the earliest part. Analyzing the MDFE and MDSE together with the delay spread the achieved results are coherent showing that transmitter position 2 performs quite poorly thus, transmitter positions 1, 3 and 4 with best average performance facilitating the receiver design.

References

[1] A. F. Molisch, "Ultrawideband propagation channels-theory, measurement, and modeling," *IEEE Transactions on Vehicular Technology*, september 2005.

[2] A. Muqaibel, A. Safaai-Jazi, A. Attiya, B. Woerner, and S. Riad, "Path-loss and time dispersion parameters for indoor uwb propagation," *IEEE transactions on wireless communications*, 2006.

[3] Z. Irahhauten, J. Dacuña, G. J. Janssen, and H. Nikookar, "Uwb channel measurements and results for wireless personal area networks applications," in *The European Conference on Wireless Technology, 2005*, October 2005.

[4] T. B. Welch, R. L. Musselman, B. A. Emessiene, P. D. Gift, D. K. Choudhury, D. N. Cassadine, and S. M. Yano, "The effects of the human body on uwb signal propagation in an indoor environment," *IEEE Journal in selected areas in communications*, december 2002.

[5] A. Alomainy and Y. Hao, "Radio channel models for uwb body-centric networks with compact planar antenna," in *Antennas and Propagation Society International Symposium 2006,IEEE*, July 2006.

[6] T. Zasowski, F. Althaus, M. Stäger, A. Wittneben, and G. Tröster, "UWB for noninvasive wireless body area networks: Channel measurements and results," in *IEEE Conference on Ultra Wideband Systems and Technologies, UWBST 2003*, nov 2003.

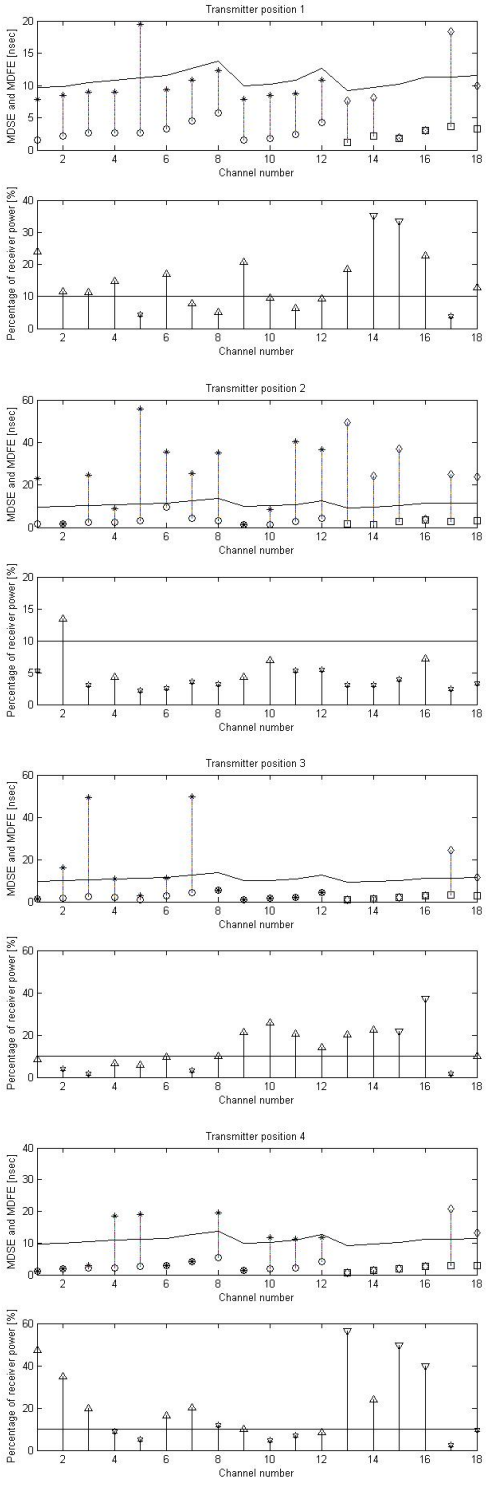

Figure 8. MDSE and MDFE for LOS and NLOS channels (top) and receiver power percentage (bottom) for transmitter position 1-4.

Third IEEE International Conference on
Wireless and Mobile Computing, Networking and Communications (WiMob 2007)
0-7695-2889-9/07 $25.00 © 2007 IEEE

Wireless communication systems from the perspective of implantable sensor networks for neural signal monitoring

C. Tarín, L. Traver, P. Martí, N. Cardona

Institute for Telecommunications and Multimedia Applications

Technical University of Valencia,
Valencia, Spain

Abstract

Recent advances in modern neurocomputing heading towards promising clinical applications of implantable neuronal sensing devices have shown the utmost necessity of wireless communication systems that allow real-time monitoring of neural signals. The design of a wireless transmission system for this particular application shall meet several requirements involving source compression of the high data rate neural recording, communication with a standard device as bridge between body area and remote server, and high fidelity of the received signal to ensure effective brain activity monitoring. A wireless transmission system over Bluetooth and 3G is analyzed for its application to the real-time transmission of neural signals captured by implanted micro-electrode array sensors. Average compression rate of 75% of the neural signal is achieved through detection using nonlinear energy operator preprocessing and automatic threshold adaptation. The wireless transmission of these signals integrates a Bluetooth transmission from the information source to a conventional mobile device and then over 3G to a remote server, without intermediate storage on the mobile phone. Reconstruction of the coded neural signal provides the input to high performance spike classification algorithm allowing the tracking of individual neuron spiking patterns.

1. Introduction

In recent years, a number of promising clinical prototypes of implantable and wearable monitoring devices have started to emerge [32]. Although a number of problems as long-term stability and biocompatibility remain, the potential medical value is enormous. Many applications exist in the field of bio-telemetry: blood glucose level monitorization, identification in cardiological life threatening episodes, etc. Our interest focusses in neural signal recording and monitoring [4], [30].

Studies conducted during the last decade have demonstrated the improvements that neural signal decoding will bring to health care, especially for patients suffering from paralysis [6], blindness [5] or deafness [22]. Spike processing techniques and, in particular, spike detection and classification are fundamental in analyzing and interpreting both in-vivo and in-vitro recordings of neural activity. Basic spike detection algorithms apply threshold-based detection to identify spikes and, although simple thresholding is attractive for real-time implementations because of its computational simplicity, it is thought to be sensitive to noise and requires user input to set effective threshold levels [2].

Telemetry systems for neuronal signals are nowadays under investigation. In fact, the implementation of a wireless transmission method for such systems brings considerable advance especially for in-vivo recordings as the subject wearing the measurement devices would then be freely moving around and neural recordings from normal life-style activities would be available. Wireless implanted neural electrodes that have been characterized and tested in-vivo are reported in [1],[7],[15]. Heading one step further, the involved wireless transmission system should be such that a conventional portable device could figure as bridge between the real-time neural recording of the implanted device and a remote server where data analysis is performed. Thus, Bluetooth and third generation mobile communication (3G) are particularly interesting as possible wireless transmission methods for such systems as these techniques are available on conventional mobile phones and other portable devices [32],[13].

The design of a telemetry application includes the specification of the communication system parameters such as data transmission capacity, synchrony, delay, etc. In other words, the application defines the set of requirements to be met by the communication system [23]. Meeting the required specifications is eventually accomplished by correct definition of the communication protocol layers which use a physical channel to implement the data communication.

We have developed a wireless transmission system for neural signals over Bluetooth and 3G. The neural signals are recorded by micro-electrode arrays and then, in real-time transmitted over a Bluetooth link to a mobile phone. This mobile device immediately, without intermediate storage, re-transmits the signals over 3G to a remote server where data processing and analysis is performed.

First, in section 2, there is a description of the characteristics of the signals captured by the neuronal multi-electrode sensors and the bandwidth requirements imposed by them. This section also includes a compression algorithm based on spike detection. Detection quality is improved through an adaptive threshold method to be used with Nonlinear Energy Operator spike detection and results are presented by means of Receiver Operating Curves.

Section 3 describes and analyzes the developed wireless transmission system over Bluetooth and 3G. This section includes an analysis of the transmission capability depending on the source compression factor. Reconstruction algorithms and signal post-processing are detailed in section 4, where the focus lies on the classification algorithms that allow the sorting of the recorded spikes and thus, the extraction of relevant neural activity parameters.

Finally, in section 5 the conclusions drawn from the developed work are shown and the future trends are discussed providing insight about the future of the wireless communication systems from the perspective of implantable sensor networks for neural signal monitoring.

.

2. Neural signal processing

Neural signals, recorded either from in-vitro cultures or from in-vivo subjects, present a high data rate information source. Due to the limited bandwidth of wireless transmission system, compression becomes mandatory. Compression through spike detection becomes extremely attractive when aiming at real-time applications and individual neuron spike pattern analysis.

2.1 Neural signals

Signals from extracellular cortical electrodes contain action potential waveforms with amplitudes ranging from tens to hundreds of microvolts

peak to peak; pulse widths are typically 1 - 1.5 ms. The noise floor, which includes biological noise from far field neurons and electrical noise from the amplifier circuit, is around 20 μVrms; Signal to Noise Ratios (SNRs) therefore range from 0 to 12 dB, although ratios as high as 20 dB are occasionally encountered. Published figures for the signal frequency content vary, ranging from 100 to 400Hz for the low end range and 3k to 10 kHz for the high end range [18].

Published sampling rates also vary, ranging from 15 kHz up to 50 kHz [20]. In general, higher sampling rates produce higher fidelity signals but also produce more data, requiring faster and higher-power systems to process them, which may become a handicap in a wireless system with limited bandwidth.

Analog to digital converter (ADC) resolution should be 10 - 12 bits to provide 60 - 72 dB of dynamic range.

In general, the required transmission bandwidth (*Bwth*) can be obtained as $Bwth = fs \cdot nbits \cdot Nch$, where *fs* is the sampling frequency in samples per second, *nbits* the number of bits per sample and *Nch* the number of channels to be transmitted. Figure **156923243.1** displays the data rate required for the transmission of a neural signal as a function of the sampling frequency and the selected number of quantization bits per sample. As it can be observed from this figure, for the transmission of one single channel with a medium sampling rate the required bandwidth is of 180 kbps. When it comes to simultaneous transmission of several channels (up-to-date in-vivo and in-vitro micro-electrode array recording systems provide up to 128 simultaneous channels [19]) including source compressing algorithms in the communication system becomes a must, especially when wireless transmission with limited bandwidth availability is aimed at.

Fig. 156923243.1 Transmission bandwidth required depending on the sampling frequency and precision.

The spiking activity among the recorded channels might differ substantially, and therefore, as widely discussed in literature [10], spike detection yields the most suitable compression algorithm. Quantitatively assessing detection quality [20],[31] requires knowledge of the ground truth, i.e., decisions taken by the algorithm on the presence of spikes must be compared with the real presence of spikes in the signal. Recordings from micro-electrode arrays do not allow intra-cellular recording which means that the ground truth is not known.

In order to overcome this problem we select two different types of source signals:

First, recordings of in-vitro neural activity kindly provided by Multichannel Systems. A 64-electrode array was used and signals where sampled at 15 kHz. Figure **156923243.2** shows the Multi Channel Systems Multi-Electrode Array (MEA). One channel of the recording was selected and spikes were manually detected by several experts. Manual detections were used as the ground truth for detection algorithms evaluation.

Fig. 156923243.2 64 channels Multi-Electrode Array (MEA) from Multi Channel Systems (www.multichannelsystems.com) widely used in neuronal signal recordings.

Second, we use a set of synthetic signals from a statistical model resembling real signals, where the spike positions are known and can be used for evaluation of spike detection algorithms.

The set of artificial signals contains 10 different signals resulting from adding an artificially generated neuronal noise with a principal neuron spike train. We started with in-vivo recordings from rat cerebellum's striatum cells, publicly available at [28]. From these recordings we isolated 50 action potentials and an additional one was selected and repeated periodically with a frequency of 50 Hz to construct the principal neuron spike train of 10 s duration. To generate a realistic underlying noise, we assumed that each neuron fires according to a homogeneous Poisson process. The Poisson model is valid if one assumes that each neuronal spike constitutes an independent random variable, which is not totally true but it yields to an approximation that suffices for the generation of additive noise, where the importance is not on the exact spiking times but on the fact that the resulting noise resembles the real neuronal noise present in micro-electrode recordings. The number of noise neurons taken for noise generation is an approximation based on the assumptions that: only neurons within 140 μm of the electrode are detectable and that the density of the motor cortex neurons is 30.000 neurons/mm [2]. A scheme of the procedure is shown in Fig. **156923243.3**. First, the firing rate for each neuron is obtained randomly in the range [50, 90] Hz, then, a firing pattern for each neuron is obtained using the Poisson process model, and finally, the resulting noise is the sum of the individual firing patterns. The principal neuron spike train is added to the adequately attenuated noise to obtain 10 different signals with SNRs in the range [1, 4.6] dB.

Fig. 156923243.3 Artificial noise generation process.

2.2 Neural signal compression

As described above, neural signals contain trains of action potentials or spikes that form particular spiking patterns. During the intervals of the signal without spikes, the content of the signal is exclusively noise. It is, therefore, possible to compress neural signals by coding the impulse trains leaving the noise-only parts away. For doing this, it is necessary to: first detect the occurrence of the spikes, and then code the time, the channel (in the case of a multi-channel recording system) and the spike waveform. In this way, it is feasible to compress and multiplex an arbitrary number of channels into one single stream of data. For this work, we have considered the Multi Channel Systems MEA case where the recording system has 64 recording electrodes, with the sampling frequency being 15 KHz and the sampling precision 12 bits. The system is then producing a $12 \times 15 \times 64 = 11520$ kbps data stream.

We have implemented a compression algorithm that works in a frame-based manner. The algorithms takes input data samples in frames containing 750 samples, i.e. 50 ms. In each frame-based step the algorithm performs spike detection for each of the channels and, when a spike is detected, the time and channel of the spike are coded at the output. Figure **156923243.4** shows the coding structure. Each coded spike results in 78 output samples to be transmitted: 1 for the channel, 2 samples for the coding the timestamp and 75 samples corresponding to the spike waveform.

Fig. 156923243.4 Coded spike.

Neural signals coded in this way can be later decoded and spike trains can be reconstructed by placing each spike waveform in the corresponding channel and time. Detection is done by a Nonlinear-Energy-Operator (NEO) based detector.

Basically the algorithm performs a preprocessing stage before detection which consists on the application of the following nonlinear operation on the input signal s[n].

$$\Psi\left(s[n]\right) = s^2[n] - s[n-1] \cdot s[n+1] \tag{1}$$

After preprocessing, spikes are detected comparing the preprocessed signal with an adaptive threshold. Real-time adaptation is done by obtaining a noise-envelope estimate via a frame-based noise-envelope tracking method and, then, setting the threshold *th*[k] to a certain level which is

proportional to the estimated noise envelope n[k] (proportionality factor *C*), where k is the frame number.

$$th[\mathrm{k}] = C \cdot \mathrm{n}[\mathrm{k}] \tag{2}$$

Such preprocessing eases the detection process because it amplifies the signal energy concentrations.

After preprocessing, spikes are detected by comparing the resulting signal amplitude with an adaptive threshold. Adaptation is done by performing automatic noise-level tracking and setting the threshold to a certain level which is relative to the estimated noise level.

As it is exposed in [2], Signal to Noise Ratios (SNRs) varies with electrode geometry, size and position with respect to the target neuron. That is why it is necessary to individually set the threshold to the appropriate value and adaptive threshold setting becomes useful.

The process for noise-level estimation is as follows. For each processing frame:

1. Calculation of the maximum absolute value of the signal amplitude $\left|\mathrm{s}_{\max}[\mathrm{n}]\right|$.
2. Comparison of the maximum with the noise-level estimation in the previous frame $\left|\mathrm{n}[\mathrm{n}\text{-}1]\right|$.
3. If the maximum is bigger than *C* times the noise level of the previous frame it is assumed that there is a spike present in the frame and therefore, the noise level estimate is not updated.
4. Otherwise,
    a. if the maximum is bigger than the noise level estimate then the noise level is updated through augmentation.

$$\left|\mathrm{s}_{\max}[\mathrm{n}]\right| > \left|\mathrm{n}[\mathrm{n}\text{-}1]\right| \Rightarrow \left|\mathrm{n}[\mathrm{n}]\right| = \alpha_{\mathrm{up}} \cdot \left|\mathrm{s}_{\max}[n]\right| + \left(1\text{-}\alpha_{\mathrm{up}}\right) \cdot \left|\mathrm{n}[\mathrm{n}\text{-}1]\right| \tag{3}$$

    b. if the maximum is smaller than the noise level estimate then the noise level is updated through reduction.

$$\left|\mathrm{s}_{\max}[n]\right| < \left|\mathrm{n}[\mathrm{n}\text{-}1]\right| \Rightarrow \left|\mathrm{n}[\mathrm{n}]\right| = \alpha_{\mathrm{dw}} \cdot \left|\mathrm{s}_{\max}[n]\right| + \left(1\text{-}\alpha_{\mathrm{dw}}\right) \cdot \left|\mathrm{n}[\mathrm{n}\text{-}1]\right| \tag{4}$$

Time constant values have been experimentally adjusted yielding adequate noise-level tracking. An example of automatic noise-level tracking is shown in Fig. **156923243.5.**

Fig. 156923243.5 Automatic neural-signal-noise-level tracking example.

2.3 Compression results

NEO based detector with automatic noise-envelope tracking algorithm is used to detect spikes in the set of real and artificial signals. Figure **156923243.6** shows spike detections given by NEO detector with automatic noise-envelope tracking for different real recording channels that offer different signal to noise ratios. One can observe that threshold adaptation to the appropriate level above the underlying noise occurs in about 0.5 seconds and that it is not affected by the spiking activity. Comparison among the four tested channels (Fig. **156923243.6** (a) to (d)) shows the algorithm ability to adapt to different SNR conditions.

Fig. 156923243.6 Automatic neural-signal noise-envelope tracking for different real recording channels with different signal to noise ratios. Input signal is plotted in blue, detections are marked in yellow, and the threshold level is depicted using magenta.

To evaluate the detection performance, Receiver Operating Curves (ROCs) have been plotted from the spike detection results. Figure **156923243.7** shows ROC families obtained for NEO when applied to the artificial signals set. It also includes resulting probabilities of detection and false alarm for the different SNRs obtained using the adaptive threshold method. Here one can see that the adaptation mechanism sets the detection working point according to the input SNR. Arrows in Fig. **156923243.7** indicate the moving direction of the working point with changing SNR if a fix threshold would be used with the consequent performance degradation.

Fig. 156923243.7 Family of ROC curves obtained for the set of 10 artificial signals with SNRs ranging from 1 to 4.6 dB. Thick dots on of the curves correspond to the detection and false alarm probabilities obtained using adaptive threshold. Arrows indicate working point moving direction if a fix threshold is used for the rest of SNR conditions.

Similarly, Fig. **156923243.8** plots ROCs corresponding to the real signal and shows that NEO curve is close to the ideal detection curve, which is the step function. Area-under-curve figure for NEO is 0.9473.

Fig. 156923243.8 ROC curve obtained using real data for NEO. Asterisk on top of the curve corresponds to the detection and false alarm probabilities obtained using adaptive threshold.

3. Wireless transmission

Figure **156923243.9** represents the overall transmission scheme. The information source is a personal computer (**PC**), where neural data recorded by the Multi Channel Systems MEA are stored. This PC establishes via a Bluetooth-Dongle a wireless communication link with a mobile terminal. The stored data are preprocessed as described in section 2 and transmitted over the Bluetooth link from the information source to the mobile device that receives them and, without intermediate storing, re-transmits them via a 3G link to a remote server PC, where the data are definitely stored, reconstructed and post-processed.

Fig. 156923243. 9 Wireless Bluetooth-3G transmission.

3.1 Bluetooth wireless transmission

Bluetooth is a flexible and capable technology for providing short-range radio communications between devices in an ad-hoc manner using the 2.4 GHz band. It is well suited as a low power radio transceiver (transmitter and receiver) operating at up to 1 Mbps [3]. Two types of channels are used in Bluetooth systems: SCO and ACL. SCO are Synchronous Connection Oriented links with fixed 64 kbps data rate used exclusively for voice traffic; while ACL are Asynchronous Connection-Less links. As shown above in Section 2, streaming of multi-channel or even single channel neural signals demands such a bandwidth which can not be offered by SCO links.
The Bluetooth connection type capable of flexible and higher bandwidths is the Asynchronous Connection-Less link [9],[16]. Figure **156923243.10** shows the core Bluetooth protocol layers.

Fig. 156923243. 10 Core Bluetooth Architecture.

The baseband layer enables the physical RF link between Bluetooth units making a connection. Link Manager Protocol (LMP) is responsible

for link set-up between Bluetooth devices and managing security aspects such as authentication and encryption. L2CAP adapts upperlayer protocols to the baseband. It multiplexes between the various logical connections made by the upper layers. Audio data typically is routed directly to and from the baseband and does not go through L2CAP.

Java standard API for Bluetooth: JSR-82

Given that our communication scheme includes a client application implemented on the information source and the server application running on a mobile phone, it is reasonable to choose a Bluetooth programming technology that is provided in nowadays mobile devices. That is why we have decided to use the standard Bluetooth Java programming API JSR-82 currently supported in a wide range of mobile devices from different manufacturers [26]. JSR-82 API allows us to establish an L2CAP point-to-point connection between client and server devices through which the neural signals are transmitted. JSR-82 supports Bluetooth standard v1.1. which is therefore the version used in our experiments.

In order to have control over the Bluetooth transmission we have programmed the client and server applications implementing the communication. In this scheme, first, an L2CAP connection is established between the master and the slave. Once communication is established, the client application running on the slave starts sending data over the connection to the master's server application. The data packet size used in the connection can be selected at compilation time and a 2 Mbyte neuronal signal of the type described in section 2 is used as data source. The transmitter monitors the channel quality by inspecting throughput.

3.2 Transmission over 3G

The third generation transmission standard for mobile communication enhances GPRS (General Packet Radio Access) in a variety of performance characteristics:

- High transmission rates up to 2 Mbps.
- High security and confidentiality.
- Efficient multiple access.
- High resistance to interferences.
- Global roaming.
- Always on, QoS (Quality of Service).
- Low cost.

In this contribution we have used the 3G technology to transmit the neural data from a mobile terminal to a remote server over public cellular networks. This remote server is either an ordinary PC, a laptop or even a remote MEA connected to a neural culture.

As the mobile device receives the neural data from the information source, they are retransmitted immediately to the remote server. Once the mobile phone is registered in the network, a profile containing all necessary parameters for the 3G transmission, such as access point etc., is established. The TCP, Transmission Control Protocol, is used for the data transmission. It offers a point-to-point connection-oriented reliable link recovering a huge variety of errors dynamically and adaptively. In order to use the TCP, the transmitter (in this particular case the mobile phone) and the receiver (equivalent to the remote server in our application) shall create the terminal points of the connection, called sockets. A socket is defined by a transmission protocol (TCP is this case), an IP address and a port number. In our experiments the mobile phone is programmed to be the client. It requests the opening of a TCP-socket to the server that is waiting for inquiries.

The application running on the mobile phone implementing both, the Bluetooth and 3G transmission, is programmed in J2ME™ (due to the limited device resources). Also, the server application is programmed using Java™.

In Fig. **156923243.9** it can be observed that both the application running on the information source PC and the remote server application incorporate the JMATLink software package. This package allows the integration of MATLAB™ applications with Java™ applications.

Especially for data pre- and post-processing as well as for real-time data representation this package offers huge advantages. The data compression algorithms described in Section 2.2 are implemented in MATLAB™ and launched by JMATLink. For the evaluation of the transmission, real-time graphical data representation is required on the server, also implemented in MATLAB™ and launched by JMATLink.

3.3 Transmission results

Due to the fact that the Bluetooth L2CAP connection is a secure channel, retransmissions assure the correct arrival of each single packet and until the acknowledgment of the former packet does not confirm its correct reception a new packet is not transmitted. For this reason, measuring transmission throughput is equivalent to measuring reception throughput.

Moreover, this ensures the real-time transmission as long as the data stream generation velocity (required transmission bandwidth as represented in Fig. **156923243.1**) does not surpass the channel throughput.

Fig. 1569023243.11 Measured mean throughput with respect to the transmission packet size

In Fig. **156923243.11** the transmission mean throughput in relation to the defined packet size is represented. The mean throughput is calculated as the number of transmitted bits divided by the overall time required for transmission measured in nanoseconds. As it can be observed from Fig. **156923243.11**, the mean throughput increases with the packet size. For a packet sizes smaller than 1000 bytes the throughput is below 180 kbps. Due to the fact that the required minimum transmission data rate for neural signals, as described in section 2 by Fig. **156923243.1** is 180 kbps, only packet sizes greater than 1000 bytes provide real-time transmission of one neural signal. For these packet sizes (> 1000 bytes) as the packet size increases, saturation in the mean throughput is observed. The obtained maximum mean throughput value is below 230 kbps.

Fig. 1569023243.12 Measured throughput and packet transmission time for packet size 512 bytes with EDR.

Fortunately, the measured throughput values are improved by using the Bluetooth v.2. EDR (Enhanced Data Rate). With this new standard, data rates up to 3 Mbps are achieved. Due to the limited processing and storage capabilities of the mobile phone, the maximum packet size for the Bluetooth transmission is 512 bytes. In Fig. **1569023243.12** (top) the real-time evolution of the transmission throughput for a packet size of 512 bytes is represented. As it can observed, there appear peak values of up to 695.6 kbps while the minimum value is 24.61 kbps. The mean throughput obtained for a 512 bytes packet size is of 323.1 kbps for the experiment shown in Fig. **1569023243.12**. Figure **1569023243. 12** (bottom) shows the corresponding time profile. It can be observed, that throughput peak values in Fig. **1569023243.12** (top) correspond to time minimum values as appears in packet nr. 8. The mean packet transmission time is calculated to be 12.67 ms. The obtained throughput allows the real-time transmission of one neural signal channel (180 kbps required for each channel). Therefore, adequate data compression before transmission is mandatory.

Analyzing the real-time throughput evolution, it is observed that less than 20% of the measured throughput values fall below the range of the

mean value. Therefore, an adequate mean throughput value guaranties the channel capacity for over the 20% of the time.

The developed compression algorithm described in section 2 is able to reduce the required data transmission rate on average to 75% depending on the spiking activity of the particular culture.

With the transmission rate limited to 323.1 kbps and taking advantage of the compression algorithm, it is possible to transmit in real-time 4 neural signals on average. In fact, the spiking activity of the neural signal is monitored in real-time and the number of transmitted neural signals is adaptively recalculated. Finally, the most active channels are transmitted in real-time. The measurement of the activity of a channel is performed inspecting the actual compression rate: the more active a channel is the lower will be its compression rate.

4. Neural signal post-processing

At the receiver, neuronal signals are reconstructed from compressed format. For doing so, for each spike, channel number, frame number and spike time are extracted. Then, spike samples are situated in the corresponding channel and time to obtain the original spike patterns.

Besides signal reconstruction, given that electrodes record signals from multiple neurons, a classification phase is needed, where spikes are assigned to originating neurons based on a spike waveform analysis algorithm.

4.1 Decoding and signal reconstruction

The spike coding algorithm that allows the source signal compression is not fully reversible, given that even for excellent detection performance the ideal curve cannot be achieved. Nevertheless, as it will be shown further on, the compression algorithm takes advantage of the neural signal characteristics thus allowing signal post-processing with similar quality as without compression.

For each frame that is received by the server the decoding algorithm provides the crucial information extracted from the frame header (see Fig. **156923243.4**) as input for the reconstruction algorithm. Frame by frame, the reconstruction algorithm situates, for the received channel identification number, the coded spike samples on the corresponding time scale. The

resulting reconstructed signal is represented in Fig. **1569023243.13.** As it can be observed, the reconstructed signal (green) contains the detected spikes but does not include the noise signal when no spike is present.

Fig. 1569023243.13 Result of the reconstruction algorithm for one channel: original neural signal (blue) compared to the reconstructed signal (green).

As a consequence, from the reconstructed signal a variety of interesting parameters for the neural signal analysis can be extracted. Actually, due to the fact that not only the spike presence is transmitted but also the corresponding recorded samples, even spike classification can be tackled.

4.2 Classification

Typically, MEA are situated such that for each electrode, there exists a number of surrounding neural cells [12]. Thus, each single electrode of the MEA records the signals originating from several neural cells, obtaining multispike trains for each MEA electrode.

The exact wave form captured for each neuron depends on the neural cell itself and the geometry of the extracellular space as described in [31]. Moreover, the wave form characteristics of the captured signal are constant over time for each neuron. Exactly these different wave form characteristics can be used to identify the corresponding neuron in a single electrode recording, that is, to classify the detected multispike train. In Fig. **1569023243.14** (top) the detections and spiking frequency obtained for a typical multispike train are depicted. Considering that this multispike train includes contributions of three different neural cells, detection and spiking frequency (depicted in Fig. **1569023243.14** (bottom)) are computed for each of the individual neurons, thus implying prior classification. From Fig. **1569023243.14** it becomes apparent that classification is a must when dealing with multispike trains. As we have seen, for each MEA electrode recording, the individual contributions of the surrounding neural cells can be distinguished using signal processing algorithms that take advantage of the similar wave form characteristics of the spikes originated by one neural cell. This implies that prior to classification a detection process shall be performed. That is the reason why compression through detection allows neural signal post-processing with similar quality parameters as those yielded for the original recorded signal. However, simultaneous firing of two or more neural cells surrounding one MEA electrode can cause overlapping of the associated wave forms deforming the resulting signal and thus, increasing the difficulty of the spike sorting task.

Fig. 1569023243.14 The need of spike sorting in multispike trains: Overall spiking pattern differs substantially form individual neural spiking patterns, also spiking frequency are not similar.

Any automatic classification process is based on two consecutive steps:

1. Extraction of the most relevant signal characteristics.
2. Based on the extracted characteristics, determination of the classes and the membership of each of the signals to the classes.

When it comes to the multispike train sorting problem, several characteristics extraction algorithms are suitable [12],[21]. Our choice fell on Principal Components Analysis (PCA), selected for its demonstrated excellent performance [34]. The PCA is based on the stored reconstructed frames. Through PCA, for each of the spike sets, a set of sorted vectors that forms an orthogonal base capable of representing the spikes' subspace is obtained. These base vectors indicate the directions of maximum data variation and each spike can be represented as a scaled sum of them. Base vectors are sorted with respect to their relative contribution in representing the set of analyzed signals and, selecting the N base vectors with highest scores of this sorted list, the spikes are characterized through their projection on the selected base vectors. Exactly these projections are the extracted characteristics, Principal Components, used for the determination of one class, that is, the originating neural cell.

Once the characteristics (N base vectors or Principal Components) have been extracted, the class membership algorithm *k-means* is applied to the multispike train. This algorithm basically consists in associating to each spike the class with the closest weight center using the Euclidean distance. The weight center of the associated class is recalculated after the inclusion of the spike.

4.3 Classification results

In order to assess performance quality of the implemented classification algorithm it is applied to both, the artificially generated signals and the real recordings from Multi Channel Systems.

Similarly to the process described in section 2.1, artificial signals containing two trains of spikes randomly superposed were generated and in fact, the artificial multispike train classification is used to tune interactively several parameters of the classification process such as Principal Component score, clustering distance etc. Once the optimized parameters

are obtained, the classification algorithm is applied to the real signal recordings from Multi Channel Systems described in section 2.

Figures **1569023243.15** to **1569023243.18** show graphically the developed classification process applied to one channel of real recordings. In Fig. **1569023243.15** the superposition, aligned to the minimum, of the detected spikes is shown. These spikes represent the input set for the PCA. As a result of the PCA, a sorted list of base vectors is computed.

Fig. 1569023243.15 Superposition of the detected spikes of one channel. Alignment is performed to the minimum value.

The computed scores of the Principal Components of the complete input spike set that form the sorted list are shown in Fig. **1569023243.16** (top). The three most scored Principal Components collect more than 81% of the overall scores, thus yielding a high-fidelity representation of the complete input set when truncating at a 3-dimensional representation. Precisely these three most relevant signals are depicted in Fig. **1569023243.16** (bottom). They form an orthogonal vector base that will be used for the whole input set space.

Fig. 1569023243.16 Scores of Principal Components of the input spike set (top) and three most relevant Principal Components (bottom).

From this 3-dimensional representation the *k-means* clustering algorithm is applied to establish the membership of each spike to one determined class. Figure **1569023243.17** (top) shows the 3-dimensional representation of the complete spike input set separating colorwise the 3 different classes. For sake of clarity, the 2-dimensional projection on the two first Principal Components is also shown in Fig. **1569023243.17** (bottom).

Fig. 1569023243.17 3-dimensional representation of the input spike set (top) and 2-dimensional projection (bottom).

The overall result of the classification is summarized in Fig. **1569023243.18** (top) that shows the input spike set separated colorwise depending on its class membership. As it can be observed from Fig. **1569023243.18** (bottom), the spikes belonging to one class show similar wave forms

Fig. 1569023243.18 Classified input spike set (top) and spikes belonging to class 1-3 (bottom).

The classification performance for the set of artificial multispike trains yields 92% of correctly classified spikes. For the real data recorded by

Multi Channel Systems (see section 2) the classification performance shall be assessed through evaluation of experts, similarly to the assessment of the detection quality described in section 2.

6. Conclusions and future trends

In this contribution a wireless transmission system over Bluetooth and 3G is analyzed for its application to the real-time transmission of neural signals captured by implanted micro-electrode array sensors.

First, the required data rates for this type of neural signals are calculated to be not less than 180 kbps for every single micro-electrode. Thus, for an array of 64 micro-electrodes a minimum transmission rate of 11520 kbps is required. To be able to compress the neural signals, detection of spikes is implemented and average 75% compression rate is achieved. Detection uses a nonlinear energy operator preprocessing and automatic threshold adaptation. Results of spike detection quality assessment show successful adaptation to different input SNRs and thus eliminating the need for manual threshold setting.

Wireless transmission of these signals integrates a Bluetooth transmission from the information source to a mobile device and a data transmission from the mobile device over 3G to a remote server, without intermediate storage on the mobile phone.

The transmission rate is limited by the Bluetooth and 3G links, depending on the transmission packet size. Due to the limited resources of the mobile phone, the maximum transmission unit is also bounded, thus achieving a maximum transmission rate of 323.1 Kbps. With this transmission rate, it is not possible to transmit more than one neural signal in real-time over the Bluetooth link without compression. With the developed compression algorithm the system performance is enhanced allowing real-time transmission of 4 neural signals considering average spiking activity.

The developed system is one step further to gain insight in brain activity for neuroscientists. Recent work indicates that there is a vast universe of possible applications [14], especially considering brain-machine interfaces (BMIs), devoted to create interfaces between the human brain and artificial devices [17],[27],[11]. Scientists from a wide range of disciplines are working on technologies that allow patients to use brain activity signals to control mechanical or electronic devices providing technologies that allow the patients to restore lost sensory-motor functions [19],[29]. There are still fundamental questions to be solved in the neurobiology field, however

first results of brain-actuated technologies, such as neuroprostheses or neurorobots, lead to optimistic expectations.

When it comes to focus on the communication systems involved in these BMIs there is still much work to be done. The neural signal, the fundamental information source, hides significant conceptual complexity and thus, its recordings shall be made available to as many researchers as possible [8]. That is why world-wide transmission systems are so important particularly in this area. On the other hand, a fundamental requirement for any communication system aimed towards the development of clinical applications of BMIs, is to be wireless in order to allow patients to wander around during neural recording and monitoring. Moreover, aspects like low power consumption (especially considering implantable devices, not only because of the body proximity but also to extent battery life) and small interference with already existing systems shall be not neglected.

Considering these requirement and the high data rates generated by implantable neural sensors, from our point of view, future applications will probably start to exploit Ultra Wideband (UWB) technology [33],[25],[24]. UWB presents several characteristics that make it very attractive for this particular application:

- considerable high transmission rates of over 100 Mbps
- extremely low power consumption
- no interference with other wireless technologies due to its spread transmission spectrum (short pulse transmission)

There are some additional considerations to be regarded. UWB allows only short distance communications with these high transmission rates, which is perfectly assumable for body area networks but raises the need of a bridge between the close body field and remote stations. By now, there is no global regulation or standardization for UWB. With the announcement of the new Bluetooth standard with UWB as core transmission technology being made commercially available very soon, the solution for these issues arose. Commercial mobile phones and computers will integrate UWB technology as high data rate transmission technology and thus, mobile phones can figure as high data rate bridges between body area communications and the rest of the world.

References

[1] Akin T, Najafi K, Bradley R (1998) A wireless implantable multichannel digital neural recording system for a micromachines sieve electrode. In: IEEE Journal of Solid State Circuits, number 33, vol. 1, pp. 109-118

[2] Anderson DJ, Oweiss KG (2003) Capturing Signal Activity and Spatial Distribution of Neurons in a Sub-Millimeter Volume. Conference Record of the Thirty-Seventh Asilomar Conference on Signals, Systems and Computers, vol 1, pp 387-390

[3] Bluetooth special interest group: Specification of the bluetooth system (2004) http://www.bluetooth.com. Accessed 23 july 2007

[4] Brown EN, Kass RE, Mitra PP (2004) Multiple neural spike train data analysis: state-of-the-art and future challenges. Nature neuroscience

[5] Fernández E, Pelayo F, Romero S, Bongard M, Marín C, Alfaro A, Merabet L (2005) Development of a cortical visual neuroprosthesis for the blind: the relevance of neuroplasticity. J. Neural Eng. vol 2, R1-R12

[6] Hochberg LR, Serruya MD, Friehs GM, Mukand JA, Saleh M, Caplan AH, Branner A, Chen D, Penn RD, Donoghue JP (2006) Neuronal ensemble control of prosthetic devices by a human with tetraplegia. Nature, vol. 442, pp 164-171

[7] Irazoqui-Pastor P, Mody I, Judy JW (2002) Transcutaneous rf-powered neural recording device. In: Proceedings of the Second Joint EMBS/BMES Conference, Houston

[8] Irazoqui-Pastor P, Mody I, Judy JW (2005) Recording brain activity wirelessly. Engineering in Medicine and Biology Magazine, IEEE vol 24, issue 6, pp 48 – 54

[9] Ju M (2002) Link management scheme of bluetooth based on channel quality estimation. p 789

[10] Kim K, Kim S (2000) Neural spike sorting under nearly 0 dB signal-to-noise ratio using nonlinear energy operator and artificial neural-network classifier. In: IEEE Transactions on Biomedical Engineering, number 47, vol 10, pp 1406-1411

[11] Lebedev MA, Carmena JM, O'Doherty JE, Zacksenhouse M, Henriquez CS, Principe JC, Nicolelis MAL (2005) Cortical Ensemble Adaptation to Represent Velocity of an Artificial Actuator Controlled by a Brain–Machine Interface. In: The Journal of Neuroscience

[12] Letelier JC, Weber PP (2000) Spike sorting based on discrete wavelet transform coefficients. In: Journal of Neuroscience Methods number 101, vol 2, pp 93-106

[13] Lopez-Casado C, Tejero-Calado J, Bernal-Martin A, Lopez-Gomez M, Romero-Romero M, Quesada G, Lorca J, Garcia E (2005) Network architecture for global biomedical monitoring service. In: 27th Annual International Conference of the Engineering in Medicine and Biology Society

[14] Martinoiaa S, Sanguinetib V, Cozzib L, Berdondinic L, van Peltd J, Tomase J, Le Massonf G, Davideg F (2004) Towards an embodied in vitro electrophysiology: the NeuroBIT project. In: Neurocomputing, number 58, vol 60, pp 1065-1072

[15] Mojarradi M, Binkley D, Blalock B, Anderson R, Ulshoefer N, Johnson T (2003) A miniaturized neuroprosthesis suitable for implantation into the brain. In: IEEE Transactions on Neural Systems and Rehabilitation Engineering, number 11, vol. 3, pp. 38-42

[16] Morrow R, (2000) Connecting with a bluetooth piconet. In: Proceedings of the Fall Wireless Symposium/Portable By Design Conference and Exhibition, Chicago

[17] Nicolelis MAL (2001) Actions from thoughts. In: Nature, vol 409, pp 403–407

[18] Obeid I, Nicolelis MAL, Wolf PD (2004) A multichannel telemetry system for single unit neural recording. In: The Journal of Neuroscience Methods, number 133, pp. 33-38

[19] Obeid I, Nicolelis MAL, Wolf PD (2004) A low power multichannel analog front end for portable neural signal recordings. In: Journal of Neuroscience Methods, number. 133, pp. 27-32

[20] Obeid I, Wolf PD (2004) Evaluation of Spike-Detection Algorithms for a Brain-Machine Interface Application. IEEE Transactions on Biomedical Engineering, vol 51, number 6

[21] Olson BP, Si J, Hu J, He J (2005) Closed-Loop Cortical Control of Direction Using Support Vector Machines. In: IEEE Transactions on Neural systems and Rehabilitation Engineering, vol 13, number 1

[22] Ryugo DK, Kretzmer EA, Niparko JK. (2005) Restoration of Auditory Nerve Synapses in Cats by Cochlear Implants. Science, vol 310, number 5753, pp 1490 – 1492

[23] Salamon D, Bei A, Grigioni M, Gianni M, Liberti M, D'Inzeo G, Luca SD (2005) Indoor telemedicine in hospital: a pda-based flexible solution for wireless monitoring and database integration. In: 27th Annual International Conference of the Engineering in Medicine and Biology Society

[24] Tarín C, Martí P, Traver L, Cardona N, Díaz JA, Antonino E (2007) UWB Channel Measurements for hand-portable devices: a comparative study. To appear in: IEEE International Symposium on Personal, Indoor and Mobile Radio Communications, Athens

[25] Tarín C, Traver L, Martí P, Cardona N, Díaz JA, Cabedo M (2007) UWB Channel measurements for measures for hand-portable and wearable devices. To appear in: Proceedings of the IEEE International Conference on Wireless and Mobile Computing, Networking and Communications, New York

[26] Tarín C, Traver L, Santamaría JF, Martí P, Cardona N (2007) Bluetooth-3G wireless transmission system for neural signal telemetry. In: Proceedings of the IEEE Wireless Telecommunications Symposium, Pomona, California

[27] Taylor DM, Helms Tillery SI, Schwartz AB (2002) Direct coritcal control of 3D neuroprosthetic devices. In: Science, vol 296, pp 1892-1832
[28] Universite Paris Descartes, UFR Biomedicale. http://www.biomedicale.univ-paris5.fr/SpikeOMatic/Data.html. Accessed 23 july 2007
[29] Wessberg J, Stambaugh CR, Kralik JD, Beck PD, Laubach M, Chapin JK, et al. Real-time prediction of hand trajectory by ensembles of cortical neurons in primates. Nature 2000; 408(6810):361–5.
[30] Wise KD, Anderson DJ, Hetke JF, Kipke DR, Njafi K (2004) Wireless implantable microsystems: High-density electronic interfaces to the nervous system. Proceedings of the IEEE
[31] Wood F, Black MJ, Vargas-Irwin C, Fellows M, Donogue JP (2004) On the Variability of Manual Spike Sorting. IEEE Transactions on Biomedical Engineering, vol 51, issue 6, pp 912-918
[32] Yu SN, Cheng JC (2005) A wireless physiological signal monitoring system with integrated bluetooth and wifi technologies. In: 27th Annual International Conference of the Engineering in Medicine and Biology Society
[33] Zasowski T, Althaus F, Stäger M, Wittneben A, G Tröster (2003) UWB for noninvasive wireless body area networks: Channel measurements and results. In: IEEE Conference on Ultra Wideband Systems and Technologies, UWBST 2003
[34] Zumsteg ZS, Kemere C, O'Driscoll S, Santhanam G, Ahmed RE, Shenoy KV, Meng TH (2005) Power Feasibility of Implantable Digital Spike Sorting Circuits for Neural Prosthetic Systems. In: IEEE Transactions on Neural Systems and Rehabilitation Engineering, vol 13, number 3

Adaptive-threshold neural spike detection by noise-envelope tracking

L. Traver, C. Tarín, P. Martí and N. Cardona

A new method for adaptive threshold setting is implemented and used in two threshold-based spike detectors: Simple Threshold (STH) and Non-linear Energy Operator (NEO). Detection quality assessment is performed using both, a set of artificially generated signals and a real neural recording. Receiver Operating Curves (ROCs) are obtained and results show that, compared to fix threshold, adaptive threshold setting yields performance improvement.

Introduction: Studies conducted during the last decade have demonstrated the advances that neural signal decoding will bring to health care, especially for patients suffering from paralysis (Hochberg et al. [1]), blindness (Fernandez et al. [2]) or deafness (Ryugo et al. [3]). Spike processing techniques and, in particular, spike detection are fundamental in analyzing and interpreting both in-vivo and in-vitro recordings of neural activity. Basic spike detection algorithms apply threshold-based detection to identify spikes and, although simple thresholding is attractive for real-time implementations because of its computational simplicity, it is thought to be sensitive to noise and requires user input to set effective threshold levels. As it is exposed in Anderson and Oweiss [4], Signal to Noise Ratios (SNR) vary with electrode geometry, size and position with respect to the target neuron. That is why it is necessary to individually set the threshold to the appropriate value and adaptive threshold setting becomes useful. This paper describes an effective adaptive threshold method to be used in Simple Threshold spike detection (STH) and Non-linear Energy Operator spike detection (NEO). Detection quality comparison between STH and NEO is also presented by means of Receiver Operating Curves (ROCs).

Neural signals: As it has been widely discussed in the literature (Obeid and Wolf [5], Wood et al. [6]), quantitatively assessing spike detection algorithms requires knowledge of the ground truth, i.e., decisions taken by the algorithm on the presence of spikes must be compared with the real presence of spikes in the signal. Recordings from micro-electrode arrays do not allow intra-cellular recording which means that the ground truth is not known. In order to overcome this problem we have:

a) First, used data (kindly provided by Multichannel Systems) that was recorded from a neuronal cell culture with rat striatum cells after application of NMDA using a 64-electrode array and 25 KHz sampling frequency. One channel of the recording was selected and spikes were manually detected by several experts. Manual detections were used as the ground truth for detection algorithms evaluation.
b) Second, constructed a set of synthetic signals from a statistical model resembling real signals.

The set of artificial signals contains 10 different signals resulting from adding an artificially generated neuronal noise with a principal neuron spike train. We started with in-vivo recordings from rat cerebellum's striatum cells, publicly available at [7]. From these recordings we isolated 50 action potentials and an additional one was selected and repeated periodically with a frequency of 50 Hz to construct the principal neuron spike train of 10 s duration. To generate a realistic underlying noise, we assumed that each neuron fires according to a homogeneous Poisson process. The Poisson model is valid if one assumes that each neuronal spike constitutes an independent random variable, which is not totally true but it yields to an approximation that suffices for the generation of additive noise, where the importance is not on the exact spiking times but on the fact that the resulting noise resembles the real neuronal noise present in micro-electrode recordings. The number of noise neurons taken for noise generation is an approximation based on the assumptions that: only neurons within 140 μm of the electrode are detectable and that the

density of the motor cortex neurons in primates is 30.000 neurons/mm^3 (Obeid and Wolf [5]). A scheme of the procedure is shown in Figure 1. First, the firing rate for each neuron is obtained randomly in the range [50, 90] Hz, then, a firing pattern for each neuron is obtained using the Poisson process model, and finally, the resulting noise is the sum of the individual firing patterns. The principal neuron spike train is added to the adequately attenuated noise to obtain 10 different signals with Signal to Noise Ratios in the range [1, 4.6] dB.

Spike detection: Detection is performed using a thresholding technique with 2 types of pre-processing. First, by applying the absolute value operator, Simple Threshold detector (STH) and second by a Nonlinear-Energy-Operator (NEO), which pre-processes input signal s[n] with the energy operator in (1), emphasizing signal energy concentrations.

$$\Psi\left(s[n]\right) = s^2[n] - s[n-1]\cdot s[n+1] \qquad (1).$$

After pre-processing, spikes are detected comparing the pre-processed signal with an adaptive threshold. Real-time adaptation is done by obtaining a noise-envelope estimate via a frame-based noise-envelope tracking method and, then, setting the threshold ($th(k)$) to a certain level which is relative to the estimated noise envelope ($n(k)$), where k is the frame number.

$$th(k) = K \cdot n[k] \qquad (2)$$

The process for noise-envelope estimation is preformed in 50 ms-long frames. Frame processing reduces computational cost since estimation performed only once per frame. The steps for each processing frame (k) are:

1. Calculate the maximum absolute value of the signal amplitude ($|s[k]|_{\max}$).
2. Compare it with the previous noise-envelope estimation: ($|n[k-1]|$).

3. If the maximum is bigger than K times the previous noise envelope, assume that there is a spike present in the frame do not update noise estimation.
4. Otherwise,
    a. if $|s[k]|_{\max} > |n[k-1]|$, $n[k] = \alpha_{up} |s[k]|_{\max} + (1-\alpha_{up}) \cdot |n[k-1]|$,
    b. if $|s_{\max}[n]| < |n[n-1]|$, $n[k] = \alpha_{dw} |s[k]|_{\max} + (1-\alpha_{dw}) \cdot |n[k-1]|$.

Time constants α_{up} and α_{dw} have been experimentally adjusted to $\alpha_{up} = 0.02$ and $\alpha_{dw} = 0.5$.

Experimental results: STH and NEO detectors have been used to detect spikes in the set of real and artificial signals. Figure 2 shows spike detections given by STH detector with automatic noise-envelope tracking. One can observe that threshold adaptation to the appropriate level above the underlying noise occurs in about 0.5 seconds and that it is not affected by the spiking activity. Comparison among the four tested channels (Figure 2 (a) to (d)) shows the algorithm ability to adapt to different SNR conditions.

To compare STH's and NEO's performance, ROCs have been plotted from the spike detection results. Figure 3 shows ROC families obtained for STH (top) and NEO (bottom) when applied to the artificial signals set. It also includes resulting probabilities of detection and false alarm for the different SNRs obtained using the adaptive threshold method. Here one can see that the adaptation mechanism sets the detection working point according to the input SNR. Arrows in Figure 3 indicate the moving direction of the working point with changing SNR if a fix threshold would be used with the consequent performance degradation.

Similarly, Figure 4 plots ROCs corresponding to the real signal and shows that NEO curve is closer to the ideal detection curve, which is the step function. Area-under-curve figure for NEO is 0.9473 against 0.9258 for STH.

Conclusions: A new method for adaptive threshold spike detection has been applied and results show successful adaptation to different input SNRs. It can be used for both STH and NEO spike detectors improving detection and eliminating the need for manual threshold setting. Additionally, spike detection quality for STH and NEO has been assessed. Although previous publications (Obeid and Wolf [5]) show that STH detection is comparable to NEO when the input signal is previously high-pass filtered; here we show that, when no pre-filtering is applied, NEO brings a significant improvement to spike detection results.

References:

1. L. R. HOCHBERG, M. D. SERRUYA, G. M. FRIEHS, J. A. MUKAND, M. SALEH, A. H. CAPLAN, A.BRANNER, D. CHEN, R. D. PENN AND J. P. DONOGHUE. "Neuronal ensemble control of prosthetic devices by a human with tetraplegia". Nature, July 2006, vol. 442, pages: 164-171.

2. E. FERNÁNDEZ, F. PELAYO, S. ROMERO, M. BONGARD, C. MARIN, A. ALFARO and L. MERABET. "Development of a cortical visual neuroprosthesis for the blind: the relevance of neuroplasticity". J. Neural Eng. 2005 Vol. 2, R1-R12.

3. D. K. RYUGO, E. A. KRETZMER, AND J. K. NIPARKO. "Restoration of Auditory Nerve Synapses in Cats by Cochlear Implants". Science, December 2005, vol. 310, no. 5753, pages: 1490 – 1492.

4. D. J. ANDERSON and K. G. OWEISS, "Capturing Signal Activity and Spatial Distribution of Neurons in a Sub-Millimeter Volume", Conference Record of the Thirty-Seventh Asilomar Conference on Signals, Systems and Computers, 2003. vol. 1, pages: 387-390.

5. IYAD OBEID and PATRICK D. WOLF, 'Evaluation of Spike-Detection Algorithms for a Brain-Machine Interface Application', IEEE Transactions on Biomedical Engineering, vol. 51, no. 6, June 2004.

6. F. WOOD, M. J. BLACK, C. VARGAS-IRWIN, M. FELLOWS and J. P. DONOGUE, “On the Variability of Manual Spike Sorting”. IEEE Transactions on Biomedical Engineering, Vol. 51, issue 6, June 2004, pages: 912-918.

7. http://www.biomedicale.univ-paris5.fr/SpikeOMatic/Data.html

Authors’ affiliations:

Lara Traver, Cristina Tarín, Paula Martí and Narcís Cardona (ITEAM, Tech. University of Valencia, Camino de Vera s/n, E-46022 Valencia, Spain)
e-mail: latrase@iteam.upv.es

Figure captions:

Fig. 1 Artificial noise generation process.

Fig. 2 Automatic neural-signal noise-envelope tracking for different real recording channels with different signal to noise ratios.

Fig. 3 Family of ROC curves obtained for the set of 10 artificial signals with SNRs ranging from 1 to 4.6 dB. Top: STH detector, bottom: NEO detector. Thick dots on of the curves correspond to the detection and false alarm probabilities obtained using adaptive threshold. Arrows indicate working point moving direction if a fix threshold is used for the rest of SNR conditions.

Fig. 4 ROC curves obtained using real data for STH (circles) and NEO (triangles). Markers on top of the curves correspond to the detection and false alarm probabilities obtained using adaptive threshold for STH (cross) and NEO (asterisk).

Figure 1

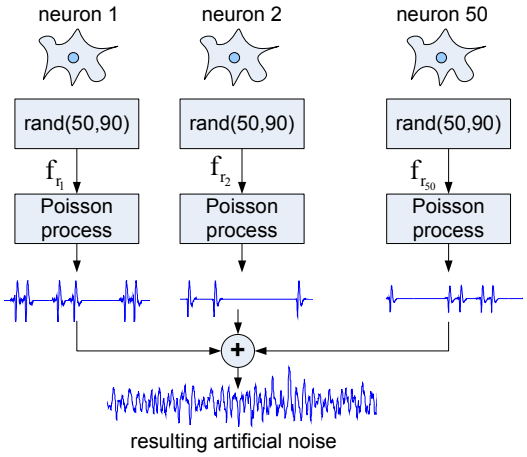
neuron 1
neuron 2
neuron 50
rand(50,90)
rand(50,90)
rand(50,90)
f_{r_1}
f_{r_2}
$f_{r_{50}}$
Poisson process
Poisson process
Poisson process
resulting artificial noise

Figure 2

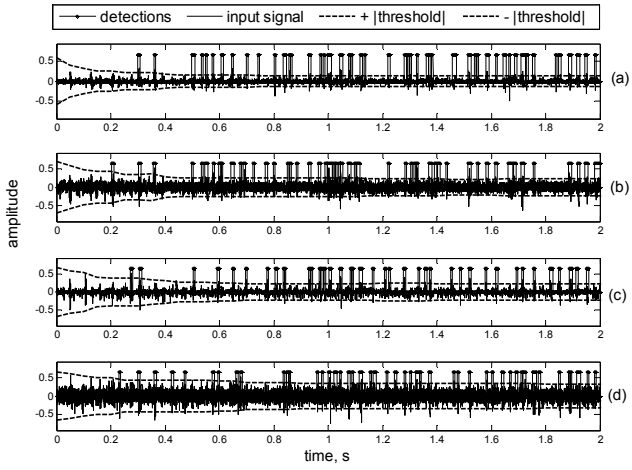
detections
input signal
+ |threshold|
- |threshold|
amplitude
time, s
(a)
(b)
(c)
(d)

Figure 3

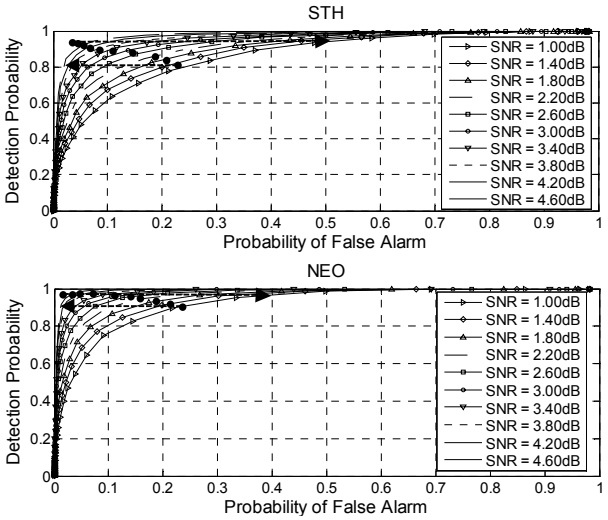
STH
Detection Probability
Probability of False Alarm
SNR = 1.00dB
SNR = 1.40dB
SNR = 1.80dB
SNR = 2.20dB
SNR = 2.60dB
SNR = 3.00dB
SNR = 3.40dB
SNR = 3.80dB
SNR = 4.20dB
SNR = 4.60dB
NEO
Detection Probability
Probability of False Alarm
SNR = 1.00dB
SNR = 1.40dB
SNR = 1.80dB
SNR = 2.20dB
SNR = 2.60dB
SNR = 3.00dB
SNR = 3.40dB
SNR = 3.80dB
SNR = 4.20dB
SNR = 4.60dB

Figure 4

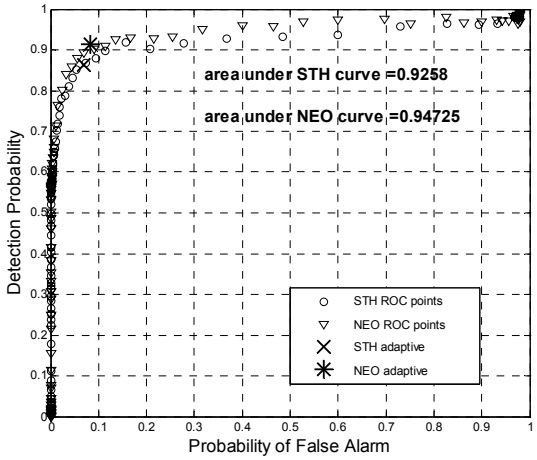
area under STH curve =0.9258
area under NEO curve =0.94725
STH ROC points
NEO ROC points
STH adaptive
NEO adaptive
Detection Probability
Probability of False Alarm
0
0.1
0.2
0.3
0.4
0.5
0.6
0.7
0.8
0.9
1